MASARYKOVA UNIVERZITA

Přírodovědecká fakulta

Ústav teoretické fyziky a astrofyziky

Diplomová práce

Brno 2026 **Bc. Sabina Pačková**

MASARYKOVA UNIVERZITA
Přírodovědecká fakulta
Ústav teoretické fyziky a astrofyziky

Diplomová práce

Ověření čtyřhvězdné povahy vícenásobných systémů

Bc. Sabina Pačková

Vedoucí práce:
doc. RNDr. Miloslav Zejda, Ph.D.

Brno 2026

Bibliografický záznam

Autor: Bc. Sabina Pačková
Přírodovědecká fakulta, Masarykova univerzita
Ústav teoretické fyziky a astrofyziky

Název práce: Ověření čtyřhvězdné povahy vícenásobných systémů

Studijní program: Fyzika
Studijní plán: Astrofyzika

Vedoucí práce: doc. RNDr. Miloslav Zejda, Ph.D.

Akademický rok: 2025/2026

Počet stran: IX + 86

Klíčová slova: Dvojzákrytové systémy, vícenásobné hvězdné systémy, zákrytové dvojhvězdy, fotometrie, spektroskopie

Bibliographic entry

Author:	Bc. Sabina Pačková Faculty of Science, Masaryk University Department of Theoretical Physics and Astrophysics
Title of Thesis:	Verification of the quadruple nature of multiple systems
Degree Programme:	Physics
Field of Study:	Astrophysics
Supervisor:	doc. RNDr. Miloslav Zejda, Ph.D.
Academic year:	2025/2026
Number of Pages:	IX + 86
Keywords:	Doubly eclipsing systems, multiple star systems, eclipsing binaries, photometry, spectroscopy

Abstrakt

Tato práce je zaměřena na výzkum dvou kandidátů na dvojzákrytové systémy, TYC 168-784-1 a V0432 Vel. Hlavním cílem bylo získat jejich základní parametry a rozhodnout, zda jsou jednotlivé páry v těchto systémech vzájemně gravitačně vázány. Pro prvotní odhad celkové efektivní teploty soustav byla využita analýza SED pomocí VOSA. Fyzikální a geometrické modelování v programu PHOEBE 2 bylo provedeno s využitím *TESS* fotometrie, doplněné radiálními rychlostmi pro primární složky TYC 168-784-1; modelování pro V0432 Vel bylo založeno výhradně na fotometrických datech. K sestavení $O-C$ diagramů byla data z *TESS* kombinována s archivními fotometrickými přehlídkami a pozemními pozorováními. Variace v $O-C$ diagramech potvrzují vzájemný orbitální pohyb mezi páry v obou systémech, což dokazuje, že jak TYC 168-784-1, tak V0432 Vel jsou skutečné, gravitačně vázané čtyřhvězdné systémy.

Abstract

This thesis is focused on the investigation of two doubly eclipsing candidates, TYC 168-784-1 and V0432 Vel. The primary objectives were to derive their fundamental parameters and determine whether their constituent binary pairs are gravitationally bound to one another. To provide an initial estimate of the overall systemic temperature, SED analyses were performed using VOSA. Physical and geometric modelling in PHOEBE 2 was performed utilising *TESS* photometry, supplemented by radial velocities for the primary components of TYC 168-784-1; modelling for V0432 Vel relied solely on photometric data. The $O-C$ diagrams were constructed by combining *TESS* data with archival photometric surveys and ground-based observations. The variations in the $O-C$ diagrams confirm mutual orbital motion between the pairs in both targets, demonstrating that both TYC 168-784-1 and V0432 Vel are true, gravitationally bound quadruple star systems.

MUNI
SCI

MASARYKOVA UNIVERZITA
PŘÍRODOVĚDECKÁ FAKULTA
KOTLÁŘSKÁ 2, 611 37 BRNO
IČ: 00216224
DIČ: CZ00216224

ZADÁNÍ DIPLOMOVÉ PRÁCE

Akademický rok: 2025/2026

Ústav:	Ústav teoretické fyziky a astrofyziky
Studentka:	Bc. Sabina Pačková
Program:	Fyzika
Specializace:	Astrofyzika

Ředitel *ústavu* PřF MU Vám ve smyslu Studijního a zkušebního řádu MU určuje diplomovou práci s názvem:

Název práce:	Ověření čtyřhvězdné povahy vícenásobných systémů
Název práce anglicky:	Verification of the quadruple nature of multiple systems
Jazyk práce:	angličtina

Oficiální zadání:
Velké množství hvězd se ve vesmíru vyskytuje v párech, část z nich se nám při vzájemném oběhu zakrývá. V posledních letech byly objeveny i vícenásobné zákrytové soustavy. Z téměř tisíce kandidátů je však jen několik desítek potvrzených případů. Cílem diplomové práce je detailní studium vybraných kandidátů na vícenásobné zákrytové systémy. Student sesbírá dostupná fotometrická data, rozplete pozorovanou světelnou křivku na světelné křivky jednotlivých zákrytových dvojhvězd a pokusí se vyloučit, že se jedná jen o tzv. blend, kdy na stejném místě hvězdné oblohy sledujeme jen překrývající se signály dvou nezávislých zákrytových soustav. Pro 1 až 2 vybrané soustavy pak provede modelování a určení základních fyzikálních parametrů složek soustavy.

Vedoucí práce:	doc. RNDr. Miloslav Zejda, Ph.D.
Konzultant:	Mgr. Jakub Kolář, Ph.D.
Datum zadání práce:	26. 10. 2024
V Brně dne:	5. 12. 2025

Zadání bylo schváleno prostřednictvím IS MU.

Bc. Sabina Pačková, 21. 11. 2024
doc. RNDr. Miloslav Zejda, Ph.D., 24. 11. 2024
Mgr. Dušan Hemzal, Ph.D., 27. 11. 2024

Poděkování

Ráda bych na tomto místě poděkovala všem, kteří mi byli během psaní této práce oporou. Můj největší dík patří vedoucímu práce, doc. Miloslavu Zejdovi, za jeho nesmírně cenné znalosti z oblasti astrofyziky a hvězdných systémů a za jeho nadšení pro pozorování, díky kterému jsem měla potřebná data.

Obrovské poděkování směřuje také mému konzultantovi, Dr. Jakubovi Kolářovi. Ten mě do fascinujícího světa dvojzákrytových systémů uvedl již během bakalářského studia a v průběhu let mi věnoval spoustu času při vysvětlování a konzultacích, a to i v době, kdy sám dokončoval své doktorské studium. Stejně tak děkuji Dr. Janu Janíkovi, který se prakticky ujal role druhého konzultanta. Děkuji mu za napozorování a zpracování velkého množství spekter i za všechny předané rady. Díky vám byly naše schůzky vždy zábavné a samotná tvorba této práce příjemnější.

Mé velké díky patří také mým přátelům za nezapomenutelných pět let plných smíchu, sdíleného zoufalství a hlavně skvělých vzpomínek. V neposlední řadě děkuji své nejoblíbenější osobě, Fílovi – bez tvé přítomnosti, podpory a motivace bych tuto cestu nedotáhla až do úspěšného konce.

Prohlášení

Prohlašuji, že jsem svoji diplomovou práci vypracovala samostatně pod vedením vedoucího práce s využitím informačních zdrojů, které jsou v práci citovány.

V Brně dne 6. května 2026

.....

Bc. Sabina Pačková

Contents

1 Stellar Multiplicity and Eclipsing Systems **1**
1.1 Introduction to Binary and Multiple Star Systems . . . 1
1.2 Doubly Eclipsing Systems . . . 6

2 Photometry **10**
2.1 Light Curve . . . 10
2.2 $O-C$ Diagrams . . . 12
2.3 Spectral Energy Distribution . . . 13

3 Spectroscopy **15**

4 Software **19**
4.1 Muniwin . . . 19
4.2 SILICUPS . . . 19
4.3 *TESS* Data Retrieval . . . 20
4.4 PHOEBE 2 . . . 20
4.5 OCFit . . . 21
4.6 Spectral Data Reduction . . . 22

5 Data analysis **24**
5.1 Objects . . . 24
5.2 Data collection . . . 25
5.2.1 *TESS* . . . 26
5.2.2 Observations . . . 27
5.2.3 Minima Timing Determination . . . 30
5.3 Photometric Results . . . 31
5.3.1 *TESS* Photometry for S1 CMi . . . 31
5.3.2 *TESS* Photometry for S4 Vel . . . 32
5.3.3 Ground-based Photometry for S1 CMi . . . 35
5.3.4 Ground-based Photometry for S4 Vel . . . 36
5.4 $O-C$ Diagrams . . . 37
5.4.1 $O-C$ Diagrams for S1 CMi . . . 37

5.4.2 $O-C$ Diagrams for S4 Vel . . . 40
5.5 SED Analysis . . . 42
5.6 Light Curve and Radial Velocity Modelling . . . 44
5.6.1 Models for S1 CMi . . . 44
5.6.2 Models for S4 Vel . . . 52

Conclusion **58**

Bibliography **60**

Appendices **69**
Scripts . . . 69
Log of Photometric Observations . . . 72
Log of Spectroscopic Observations . . . 74
Minima Timings . . . 76
Figures . . . 85

Chapter 1

Stellar Multiplicity and Eclipsing Systems

1.1 Introduction to Binary and Multiple Star Systems

A binary star system consists of two gravitationally bound objects that orbit their common centre of mass. These systems provide a unique opportunity to directly measure stellar masses through analysis of their orbital motion using Kepler's Third Law (generalised by Newton):

$$P^2 = \frac{4\pi^2}{G(M_1 + M_2)} a^3 \,, \tag{1.1}$$

where P is the orbital period, G is the gravitational constant, M_1 and M_2 are the masses of the components, and a is the semi-major axis of the relative orbit.

The classification of binary systems depends on observational characteristics, such as their geometry and the method of their detection.

Astrometric binaries consist of one visible component, while the second star is not spatially resolved, typically due to high brightness contrast or an angular separation that is too small to be distinguished. The binary nature of the system is revealed by precise measurements of the position of the visible star (Carroll & Ostlie, 2017). While the system's centre of mass moves in a linear path across the sky due to its proper motion, the gravitational influence of the unseen companion forces the visible star to orbit this moving centre. Consequently, the visible star's position periodically deviates from this straight line, resulting in a wavy or sinusoidal trajectory on the sky (Kallrath & Milone, 2009).

Spectroscopic binaries are binary star systems in which the components are too close to be resolved visually through a telescope. However, their binary nature is revealed by periodic Doppler shifts in their spectral lines (Batten & Haar, 2013). Depending on whether lines from one or both stars are visible, these systems are classified as

single-lined (SB1) or double-lined (SB2) spectroscopic binaries, which are discussed in more detail in Chapter 3.

Eclipsing binaries are systems where the orbital plane is oriented so closely to the observer's line of sight that the two stellar components periodically pass in front of one another. These mutual occultations cause periodic drops in the system's observed brightness, which are recorded as minima in a light curve. The orbital inclination i defines the angle of the system's orbit to the plane of the sky. An inclination of $i = 90°$ means the observer's line of sight lies exactly within the orbital plane. For a binary system consisting of spherical stars with radii R_1 and R_2 separated by a distance a, the geometric condition for eclipses to occur is given by Hilditch (2001):

$$\sin(90° - i) \leq \frac{R_1 + R_2}{a}. \tag{1.2}$$

When this geometric condition is met, a typical eclipsing binary features two distinct dips per orbital period. The primary eclipse occurs when the hotter component is obscured by the cooler star, resulting in the deeper minimum. The secondary eclipse occurs half an orbit later (in circular orbits) when the cooler star is eclipsed by the hotter one (Hilditch, 2001; Batten & Haar, 2013).

Depending on the relative sizes of the stars and the inclination angle, the eclipses can be total (the smaller star is completely hidden), annular (the smaller star transits in front of the larger one), or partial (for lower inclinations, where the stars only partially overlap). During total and annular eclipses, the light curve exhibits a flat minimum, while partial eclipses produce V-shaped or rounded minima (Hilditch, 2001; Terry D. Oswalt, 2013)

The shape and duration of the eclipses allow astronomers to determine the orbital inclination and the fractional radii of the stars relative to their semi-major axis (Batten & Haar, 2013). When combined with radial velocity curves, parameters including masses, radii, luminosities and surface gravities can be determined (Hilditch, 2001).

Traditionally, eclipsing binaries are classified based on the morphology (shape) of their light curves. The categories are based solely on the visual appearance of their variations in brightness and are named after prototype stars: Algol-type (EA), β Lyrae-type (EB), and W Ursae Majoris-type (EW).

Algol-type light curves (Figure 1.1) are usually characterised by a significant difference in the depths of the primary and secondary minima, indicating that the stars often have quite different surface temperatures and luminosities. However, in some cases, the eclipse depths can be nearly equal if the stars have similar brightness. Between eclipses, the light curve is typically flat and constant, suggesting that proximity and reflection effects are minimal. From the light curve, the moments of the beginning and end of the eclipses can be clearly determined. Although the flat maxima may imply that the stars are nearly spherical and physically detached, many systems (including the prototype

Algol) are semi-detached. This is explained by the Algol paradox; the donor star has filled its Roche lobe and is therefore significantly distorted, yet the system still produces an EA-type light curve. This occurs because the more luminous, nearly spherical star dominates the total light of the system, masking the variations of the distorted donor star. This demonstrates that morphological and physical classification do not always correspond perfectly. The orbital periods of the EA systems vary significantly, ranging from approximately 0.2 days to several decades (Kallrath & Milone, 2009).

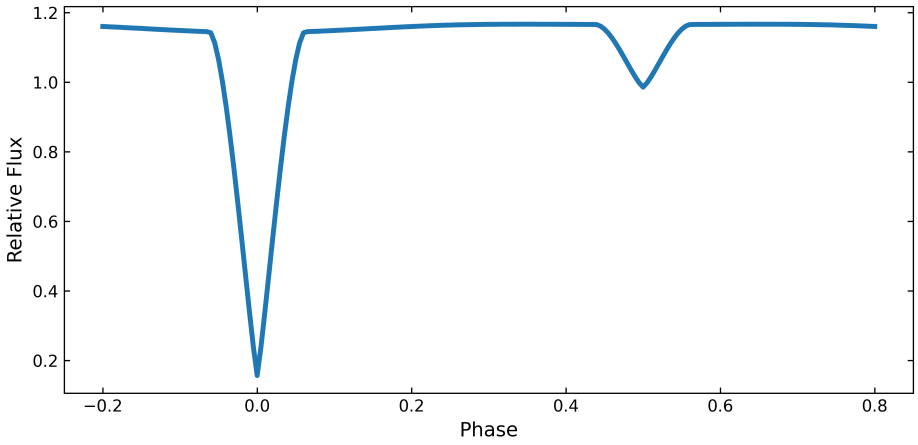

Figure 1.1: A synthetic phase curve of an Algol-type eclipsing binary, generated using PHOEBE 2 (see Section 4.4).

β Lyrae-type light curves (Figure 1.2), by comparison, exhibit continuous brightness changes between minima, with no flat sections between eclipses, making it challenging to determine the exact onset and end of the eclipses. The primary and secondary minima are both rounded and differ in depth, indicating that the components have different surface temperatures. In these systems, at least one component is strongly ellipsoidal due to tidal distortion. Orbital periods are relatively short, typically exceeding 0.5 days. Physically, these systems are classified as semi-detached or contact (Kallrath & Milone, 2009).

W Ursae Majoris-type light curves (Figure 1.3) also display continuous variation in brightness. However, unlike the β Lyrae-type systems, the minima are almost equal in depth, suggesting that the components have similar surface temperatures. Both stars are strongly distorted due to their close proximity. Orbital periods range from a few hours up to one day. Physically, both stars fill their Roche lobes and may share a common envelope, classifying them as contact binaries (Kallrath & Milone, 2009; Sterken & Jaschek, 1996).

In contrast to the observational classification based on light curves, Kopal (1955) introduced a scheme applicable to all close binary systems. It is based on the system's geometric configuration, specifically the extent to which its components fill their Roche lobes (Kallrath & Milone, 2009). These are critical regions surrounding each star

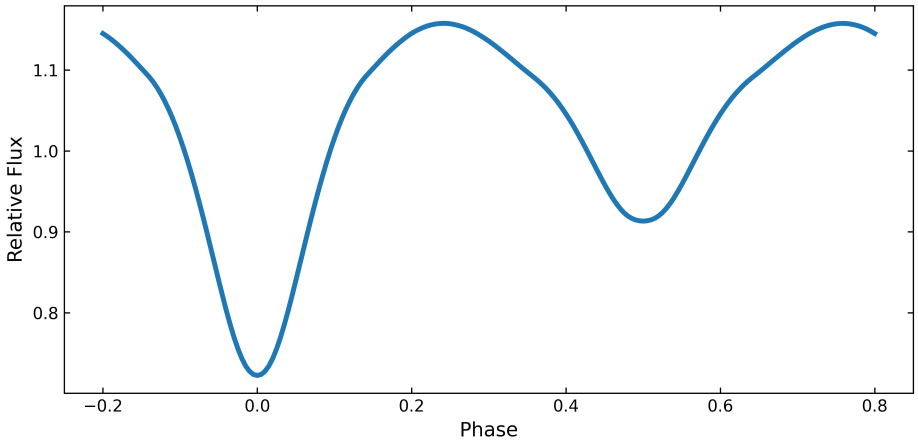

Figure 1.2: A synthetic phase curve of a β Lyrae-type binary, generated using PHOEBE 2 (see Section 4.4).

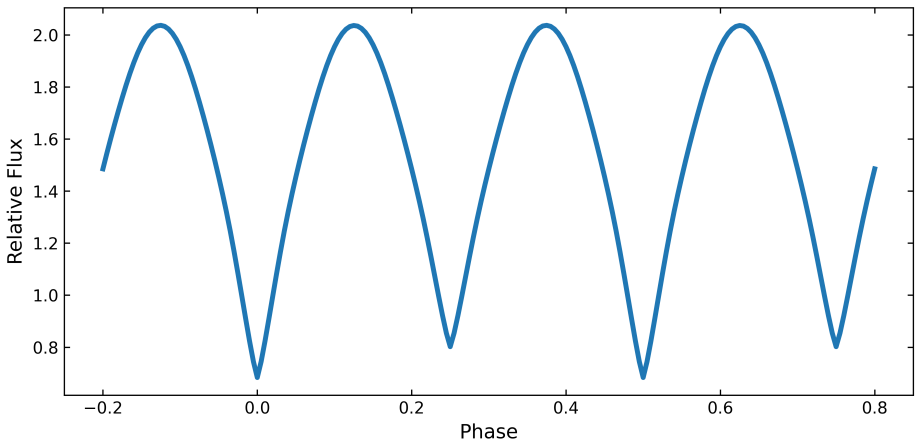

Figure 1.3: A synthetic phase curve of a W Ursae Majoris-type binary, generated using PHOEBE 2 (see Section 4.4).

in a binary system within which material is gravitationally bound to that specific component. The degree of filling, therefore, reflects the physical and evolutionary status of the binary components. According to this criterion, close binaries are categorised into three groups (Hilditch, 2001):

Detached binaries: Both components lie completely within their respective Roche lobes. The stars do not exchange mass and evolve essentially independently. They generally retain spherical shapes, but may exhibit minor tidal distortion (Hilditch, 2001; Batten & Haar, 2013; Kallrath & Milone, 2009).

Semidetached binaries: One star has expanded to completely fill its Roche lobe, while its companion remains well inside its own lobe. Because the expanded star's surface reaches the inner Lagrangian point (L_1), its outer material becomes gravitationally unstable and can spill through this point, initiating a transfer of mass to its companion (Hilditch, 2001; Batten & Haar, 2013).

Contact binaries: Both components fill or overfill their respective Roche lobes. When both stars overfill their inner Lagrangian surfaces, they touch and are surrounded by a shared, common envelope of material; these are sometimes referred to as over-contact systems (Hilditch, 2001; Batten & Haar, 2013; Kallrath & Milone, 2009).

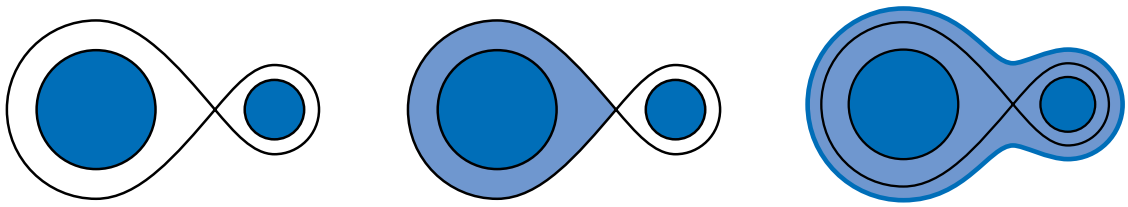

(a) Detached system. (b) Semi-detached system. (c) Over-contact system.

Figure 1.4: Three types of close binaries. Recreated from Carroll & Ostlie (2017).

In recent years, significant progress has been made in the study of multiple star systems, largely due to high-precision space-based photometry. The launch of NASA's *TESS* (Transiting Exoplanet Survey Satellite) (Ricker et al., 2015) has been particularly instrumental, enabling the discovery of many new multiple stellar system candidates, especially those in quadruple configurations.

Systems consisting of more than two stars tend to be hierarchical. For such a configuration to remain stable over a long timescale, the basic structural unit must always be a binary. As mentioned in Tokovinin (2014), this is possible because the gravitational influence of the outer companion(s) does not significantly perturb the motion within the close pair. The only stable configuration for a triple star system consists of a close binary and a more distant third star. Quadruple systems can exist in two possible configurations: a triple system with an even more distant fourth star (3+1 quadruple; see Figure 1.5a), or two binaries whose centres of mass orbit each other (2+2 quadruple;

see Figure 1.5b). According to Tokovinin (2021), the frequency of 2+2 quadruples is approximately four times higher than that of 3+1 quadruples. Furthermore, when both binaries in a 2+2 configuration are eclipsing, the system is referred to as a doubly eclipsing system.

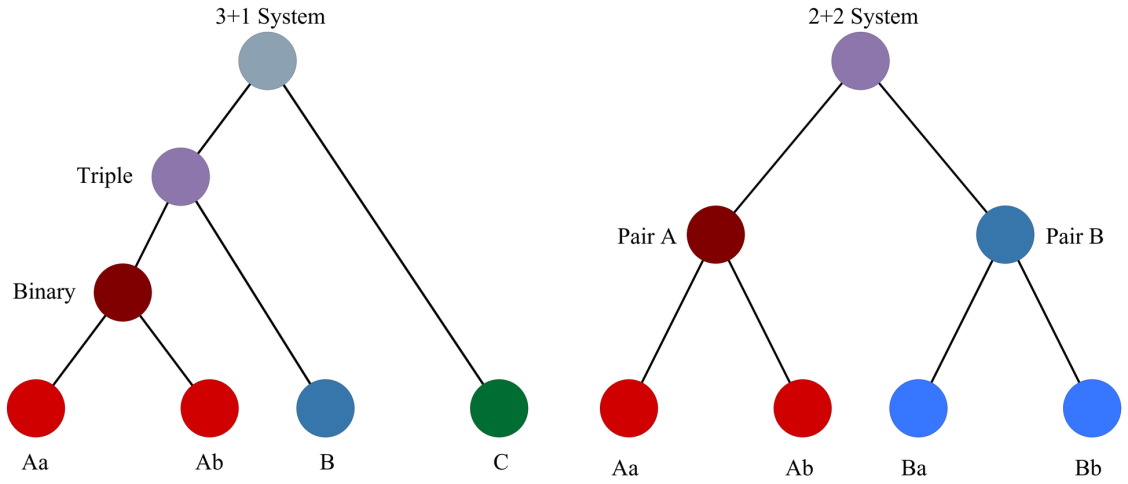

(a) Hierarchical structure of 3+1 quadruple. (b) Hierarchical structure of 2+2 quadruple.

Figure 1.5: Schematic representation of possible quadruple system configurations.

1.2 Doubly Eclipsing Systems

A doubly eclipsing system is a specific subclass of the 2+2 hierarchical quadruple systems in which both inner binaries (typically designated pair A and pair B) are oriented in such a way that they exhibit eclipses along the observer's line of sight. While 2+2 quadruple systems are relatively common in the universe, comprising about 4 per cent of solar-type star systems (Tokovinin, 2021), doubly eclipsing systems are observationally rare (Kostov et al., 2022a). Currently, there are approximately 1000 candidate systems identified (Zasche et al., 2025), yet only about 60 have been fully confirmed (Kolář, 2025). The discovery of new 2+2 doubly eclipsing candidates relies on mining the massive datasets generated by long-duration, high-precision photometric surveys. Researchers are employing machine learning algorithms that scan through hundreds of millions of light curves and recognise those that contain a signature of "extra" eclipses (Kostov et al., 2022a).

In these systems, the two binaries orbit their common centre of mass with an outer period P_{AB} much longer than the individual inner periods P_{A} and P_{B}. According to Tokovinin (2008), 25 per cent of quadruples have outer periods in the range of 10 to 100 years. However, the "typical" values depend heavily on the available data. Because

photometric surveys generally only span a decade or two of observations, most systems actually possess much longer outer periods that cannot yet be detected (Zasche et al., 2019). Nevertheless, while rare, there are cases with outer periods shorter than one year, such as the system BU CMi, which currently holds the record for the shortest known outer period at just 121 days (Pribulla et al., 2023). A schematic representation of the orbits for such a system is shown in Figure 1.6.

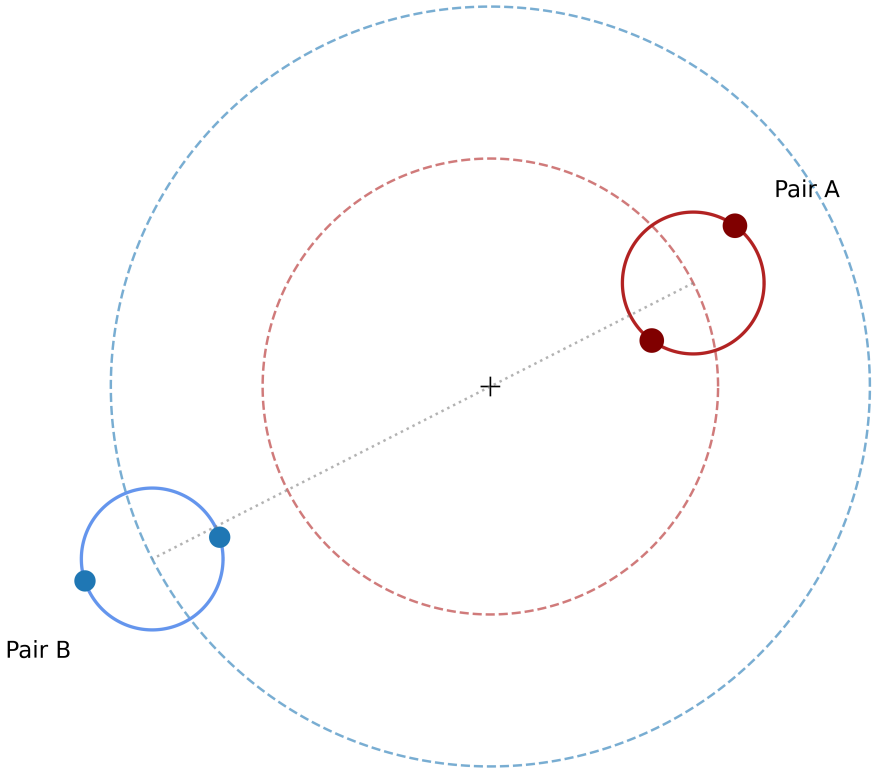

Figure 1.6: A schematic representation of a hierarchical 2+2 quadruple system. The solid lines depict the inner orbits of the individual stars within pair A (red) and pair B (blue). The dashed lines illustrate the outer mutual orbit of the two pairs' centres of mass around the system barycentre (marked with a cross). The condition $M_{\mathrm{A}} > M_{\mathrm{B}}$ is reflected by pair A orbiting closer to the common barycentre.

Observationally, the light from the four stars is blended together into one photometric (or spectroscopic) signal. However, the disentanglement method allows for the separation of this composite light into two distinct signals, one representing each binary.

To survive long-term without ejecting components or disintegrating, these systems must satisfy strict hierarchical stability criteria, such as those defined by Mardling & Aarseth (2001) and Eggleton & Kiseleva-Eggleton (2001), which have been utilised in recent studies of multiple systems (Hamers, 2019; Torres et al., 2017). The system's

outer period and semi-major axis must be significantly larger than those of the inner binaries (Powell et al., 2025). The exact minimum stability ratio strongly depends on the eccentricity of the outer orbit and the mass ratios of the components (Hamers, 2019; Powell et al., 2025).

The two pairs must share an evolutionary history, which makes this a great advantage while analysing the individual binaries. Pair A and pair B should yield consistent results regarding distance, age, and metallicity (Zasche et al., 2023). The structural architecture of such systems acts as a genetic record of how stars form and assemble. Measuring the ratios between the individual components, the orbital period ratios between the two binary stars, and their mutual inclinations, can help distinguish whether a system formed via core or disk fragmentation or via gravitational capture (Kostov et al., 2022a). Additionally, observing how their inner orbital periods cluster near certain resonances provides constraints on how their orbits migrated and evolved (Kolář et al., 2025; Zasche et al., 2019). They allow astronomers to directly observe gravitational effects that either do not occur or are much weaker in simpler systems.

For example, in non-coplanar systems, mutual gravitational interactions drive nodal precession (Zasche et al., 2024). This continuous shift in the binary's orbital inclination relative to Earth observationally manifests as changing eclipse depths, or even their complete disappearance, over timescales of decades to centuries (Borkovits et al., 2021). Additionally, these systems exhibit apsidal motion due to the Kozai-Lidov cycles or eccentricity variations (Zasche et al., 2024). Quadruple systems are significantly more efficient than triple systems at driving their inner binaries to extreme eccentricities through mechanisms like Lidov-Kozai oscillations (Fang et al., 2018). When paired with tidal friction, these extreme eccentricities cause the inner orbits to rapidly shrink, which can lead to stellar mergers, thus producing hierarchical triples or blue stragglers (Borkovits et al., 2018).

The quadruple nature of these candidates can be confirmed via Eclipse Timing Variations (ETV). Precisely, the gravitational bond is identified by the presence of the Light Time Effect (LiTE) in their $O-C$ diagrams. Since both pairs orbit the same centre of mass, their $O-C$ diagrams must be anti-correlated. The ratio of their LiTE amplitudes ($A_{\rm A}$ and $A_{\rm B}$) allows for the direct determination of the mass ratio ($q_{\rm AB}$) between the two binaries (Kolář et al., 2026):

$$\frac{A_{\rm B}}{A_{\rm A}} = \frac{M_{\rm A}}{M_{\rm B}} = q_{\rm AB}\,, \tag{1.3}$$

where $M_{\rm A}$ and $M_{\rm B}$ represent the total mass of binary A and binary B, respectively.

However, the subsequent extraction of fundamental stellar parameters (masses, radii, and temperatures) heavily depends on the system's architecture. For wide systems with a long period (several years to decades), gravitational perturbations are negligible, and the ETVs are strictly dominated by LiTE (Zasche et al., 2024; Kolář et al., 2025).

This allows researchers to employ an iterative approach, disentangling the light curves and modelling each binary independently (Zasche et al., 2020). Conversely, in compact systems with a short outer period, strong mutual perturbations introduce significant dynamical delays into the ETVs (Powell et al., 2025). To extract precise masses, radii, and temperatures of these tight systems, numerical N-body integrations are needed to accurately solve the system (Powell et al., 2025).

Chapter 2

Photometry

One of the most significant measurable pieces of information about a star is its luminosity, defined as the total amount of energy in the form of electromagnetic radiation emitted by celestial objects per unit time. This property can be investigated through photometry, which is the measurement of a star's apparent brightness.

The earliest photometric observations were carried out visually, using the human eye as a detector. This was later succeeded by photographic photometry, which utilised glass photographic plates. The ability of these plates to record large areas of the night sky enabled the creation of extensive sky surveys. Technological advances later led to photoelectric photometry, employing photomultiplier tubes to convert photons into an electrical signal. Nowadays, however, the majority of observers use cameras equipped with CCD (Charge-Coupled Device) or CMOS sensors for detection.

2.1 Light Curve

A light curve records an object's apparent brightness, expressed in flux or magnitudes, against time, allowing researchers to categorise variable stars and to characterise the underlying physical processes, stellar structures, or orbital mechanics (Kallrath & Milone, 2009).

In practice, the relative magnitude of a variable star ($\Delta m = m_\mathrm{v} - m_\mathrm{c}$) is plotted on the vertical axis. It is determined by the ratio of the variable star's brightness (j_v) to that of a comparison star with constant brightness (j_c) (Mikulášek & Zejda, 2013):

$$\Delta m = -2.5 \log \left(\frac{j_\mathrm{v}}{j_\mathrm{c}} \right) . \tag{2.1}$$

Alternatively, if the brightness variations are periodic, the phase can be plotted on the horizontal axis instead of time, resulting in a phase curve. The phase indicates which part of the cycle the system is currently in. To construct a phase curve, it is necessary to know the period P and the reference time from which the phase is calculated. The

reference time is usually the epoch of the primary minimum T_0. The phase φ at any given observation time t can be calculated using the equation:

$$\varphi = \text{frac}\left(\frac{t - T_0}{P}\right) , \tag{2.2}$$

where the frac function retains only the decimal part of the real number. Therefore, the phase takes values between zero and one. In some cases, the curve may be shifted to make the eclipses more clearly visible (see Figure 2.1).

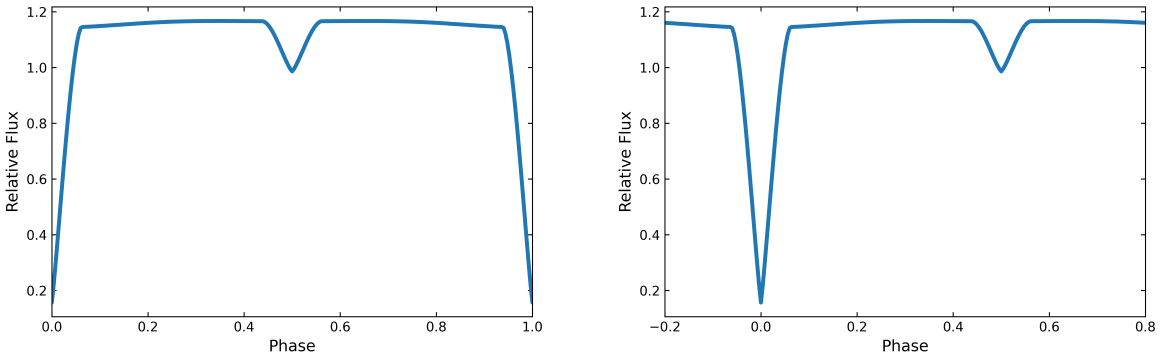

Figure 2.1: Synthetic light curve of an eclipsing binary generated using PHOEBE 2 (see Section 4.4), illustrating the necessity of phase shifting. Left: A standard phase curve plotted from $\varphi = 0$ to 1, where the primary minimum is split. Right: The same synthetic data shifted to a phase range of -0.2 to 0.8, allowing the primary minimum at $\varphi = 0$ to be viewed as a continuous feature.

While the fundamental shape of an eclipsing binary light curve is defined by the system's geometry, real stellar systems rarely produce perfectly simple geometric shapes. Several physical phenomena can significantly distort them (see, e.g., Kallrath & Milone, 2009; Percy, 2007):

Limb darkening: This effect occurs because the edges of a stellar disk appear cooler and fainter than the centre, making the bottom of eclipses appear rounded rather than flat and altering the slopes of the eclipse ingress and egress.

Gravity darkening: In close binaries where tidal forces distort the stars into ellipsoids, the surface gravity is lower at the elongated ends and therefore these regions are cooler and fainter. As a result, the light curve appears rounded outside of eclipses (ellipsoidal variations), as the system is noticeably brighter between eclipses than near them.

The reflection effect: The radiation from a hotter primary star heats the facing hemisphere of its cooler companion. This manifests in the light curve as an upward, concave curvature between eclipses, often creating distinct "shoulders" around the secondary eclipse.

Starspots: Magnetic activity can produce cool starspots that cause migrating, wave-like distortions as the system rotates. A notable consequence of this is the O'Connell effect, characterised by asymmetric out-of-eclipse maxima of unequal brightness.

2.2 $O-C$ Diagrams

The $O-C$ diagram visualises the difference between the Observed (O) times of minima derived from light curves and the Calculated (C) times predicted by a linear ephemeris equation:

$$C = T_0 + P \times E\,, \tag{2.3}$$

where P is the period and E is the cycle number, which refers to the number of cycles since the reference minimum T_0. The resulting difference ($O-C$) is plotted as a function of time or cycle number.

From the morphology of the diagram, it is possible to identify an incorrectly determined period or initial time of minima T_0, detect period changes, and recognise physical phenomena such as apsidal motion. Furthermore, the diagram can reveal the presence of an additional body or even be used to verify the gravitational binding of two binary pairs within a quadruple stellar system.

If the period of the system is constant, and the light elements are accurate, the $O-C$ diagram appears as a horizontal line distributed around zero. If the period is correct but the reference epoch T_0 is inaccurate, the data still form a horizontal line, but shifted upward or downward, reflecting the incorrect value of T_0. In the opposite case, where T_0 is correct, but the period is inaccurate, the $O-C$ data follow a linear trend with a non-zero slope (Pačková, 2024).

More complex behaviours are possible as well. For example, a parabolic curve indicates a linear period change, often driven by physical mechanisms such as mass transfer between components. Strictly periodic wave-like variations are typically caused by the Light-Time Effect (LiTE), which is arguably the most significant feature in the $O-C$ diagrams of doubly eclipsing systems. Due to the finite speed of light, as a binary moves away from the observer in its outer orbit, the eclipse signal travels a longer distance, arriving later than predicted. Conversely, when the binary is closer to the observer, the signal arrives earlier. This results in a periodic, quasi-sinusoidal variation in the $O-C$ diagram. If the two binaries are gravitationally bound, the conservation of momentum dictates that they must orbit their common centre of mass on opposite sides with a shared outer period. Consequently, their respective $O-C$ diagrams must be anti-correlated (see Figure 2.2). In eccentric eclipsing binaries, a similar wave-like signature in the $O-C$ diagram is produced by apsidal motion. The intervals between successive primary and secondary eclipses periodically change as the elliptical orbit

rotates in space, causing the $O-C$ variations of the primary and secondary minima within the same binary to be out of phase. This internal anti-correlation is the diagnostic used to distinguish apsidal motion from the LiTE caused by a third body, which shifts the entire binary system and results in completely in-phase variations for both types of minima (Batten & Haar, 2013).

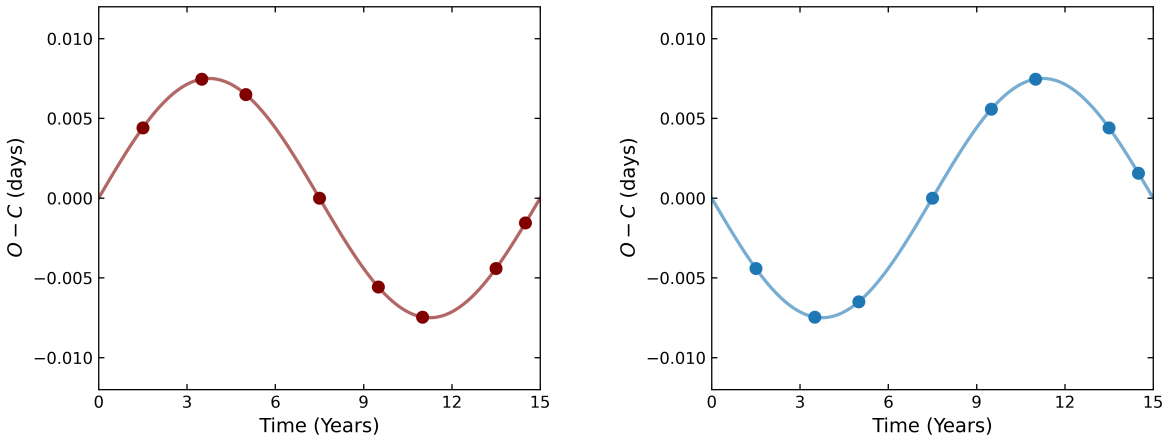

Figure 2.2: Synthetic $O-C$ diagrams illustrating the Light-Time Effect (LiTE) in a $2+2$ system, where both binaries are of equal mass and share an outer period of 15 years.

2.3 Spectral Energy Distribution

A Spectral Energy Distribution (SED) represents how much energy an astronomical object emits across the electromagnetic spectrum. The SED graph shows the dependence of the emitted flux on frequency or wavelength.

An observed SED is constructed from multiple photometric measurements obtained through filters at different wavelengths, often combined with spectroscopic observations (Hilditch, 2001). By comparing the observed SED to theoretical spectral models, it is possible to estimate some physical parameters of the object, such as the effective temperature ($T_{\rm eff}$), surface gravity ($\log g$), and metallicity (Gezer et al., 2025).

The analysis of doubly eclipsing binaries is more complex because the photometric data represent the integrated flux of all four stellar components. As a result of each star possessing its own effective temperature, its peak emission occurs at a different wavelength. Therefore, individual stars alter the overall shape of the system's combined SED in distinct ways. For instance, the presence of a significantly cooler component will manifest as an excess of flux at longer, infrared wavelengths. Conversely, if the system contains one dominating, hot star, its high luminosity will overpower the cooler companions and reshape the composite SED to mimic a higher overall temperature. Because of this blending, the composite temperature from an SED fit generally serves as an upper limit rather than an exact measurement of the individual stars' temperatures

(Kolář et al., 2026). Hence, based solely on these combined data, it is difficult to determine whether the individual components possess significantly different effective temperatures or if they share similar physical characteristics.

Finally, there are several obstacles to extracting reliable data from SEDs. Accurate distance measurements and extinction parameters are essential; if inaccurate, the resulting SED fits can be significantly biased (Kolář et al., 2026). Borkovits et al. (2021) even caution that highly precise photometric data points can statistically dominate the SED fit, skewing the overall results.

Chapter 3

Spectroscopy

Astronomical spectroscopy is an observational technique used to deduce the physical and chemical properties of celestial objects by analysing their electromagnetic radiation. When light passes through a diffraction grating, it is dispersed into its component wavelengths, producing a spectrum. A modern spectrum is generally represented as a graph showing the intensity of radiation as a function of wavelength or frequency. The wavelength λ and frequency ν are related by a simple formula:

$$c = \lambda \nu \,, \tag{3.1}$$

where c is the speed of light.

A stellar spectrum can provide information about several properties of a star, including effective temperature, surface gravity, chemical composition, projected rotational velocity, and strength of the magnetic field (Hilditch, 2001). One of the most fundamental results obtained from spectroscopy is the measurement of a star's velocity along the line of sight of an observer, known as the radial velocity. Radial velocities are determined through the Doppler effect, which causes a shift in the wavelength position of the spectral lines due to the motion of the star toward or away from the observer. The relation between the observed wavelength shift and the radial velocity is given by:

$$\frac{\lambda - \lambda_0}{\lambda_0} = \frac{\Delta\lambda}{\lambda_0} = \left(\frac{1 + (V/c)}{1 - (V/c)}\right)^{1/2} - 1 \approx \frac{V}{c} \quad \text{for} \quad V \ll c \,. \tag{3.2}$$

Here λ_0 is the laboratory wavelength of the spectral line, λ is the observed wavelength, and V is the radial velocity of the star (Hilditch, 2001).

In binary systems, the orbital motion of the components causes periodic variations in their measured radial velocities. The observed radial velocity of a star varies continuously as it moves along its orbit. At any given time t, the velocity can be described mathematically using the orbital elements of the system:

$$V_{\mathrm{r}}(t) = \gamma + K[\cos(\theta(t) + \omega) + e\cos\omega] \,, \tag{3.3}$$

where γ is the systemic velocity, representing the constant motion of the system's centre of mass relative to the observer. The parameter K is the radial velocity semi-amplitude, e represents the orbital eccentricity, and ω specifies the argument of periastron. The angle $\theta(t)$, known as the true anomaly, describes the angular position of the star in its orbit at time t (Hilditch, 2001).

Plotting these measured velocities against time or orbital phase yields radial velocity curves (see Figure 3.1), which are essential for analysing binary star systems. Depending on the system, analysing these curves provides crucial stellar data:

Double-lined spectroscopic binaries (SB2): If the components have similar luminosities, spectral lines for both stars are visible. Measuring the radial velocity semi-amplitudes for both the primary (K_1) and secondary (K_2) components allows astronomers to directly determine the mass ratio of the system.

$$\frac{K_1}{K_2} = \frac{M_2}{M_1} = q\,. \tag{3.4}$$

Single-lined spectroscopic binaries (SB1): If only the brighter star is visible, K_2 is unknown, and a mass ratio cannot be determined directly from the velocity curve alone. However, a "mass function" can still be obtained:

$$f(M_1, M_2, i) = \frac{P}{2\pi G} {K_1}^3 (1-e^2)^{3/2}\,, \tag{3.5}$$

where P is the orbital period and G is the gravitational constant. If the mass ratio q is known from photometry, the mass of the secondary component M_2 can be calculated from the mass function as:

$$M_2 = \frac{(1/q+1)^2}{\sin^3 i} f(M_1, M_2, i)\,, \tag{3.6}$$

and the primary mass M_1 as:

$$M_1 = \frac{1}{q} M_2 = \frac{(1/q+1)^2}{q^3} \frac{1}{\sin^3 i} f(M_1, M_2, i)\,. \tag{3.7}$$

Even without available information about q, the sum of masses can still be expressed as:

$$M_1 + M_2 = \frac{1}{\sin^3 i} (1+1/q)^3 f(M_1, M_2, i)\,. \tag{3.8}$$

While photometric light curves yield crucial geometric quantities such as the orbital inclination i and relative radii, radial velocity curves provide the absolute physical scaling factor. It is the combination of these two techniques that allows for the determination of the semi-major axis and stellar masses in true physical units (Kallrath & Milone, 2009).

The spectroscopic analysis of multiple star systems is significantly more complex. Obtaining accurate radial velocities requires isolating the spectral signatures of each

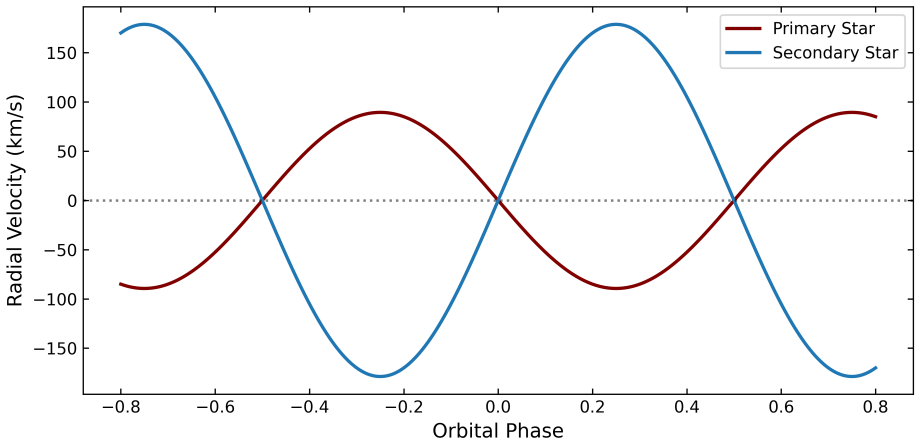

Figure 3.1: Synthetic radial velocity curves for a double-lined spectroscopic binary (SB2) system modelled with a mass ratio of $q = 0.5$, generated using PHOEBE 2 (see Section 4.4). The red and blue lines trace the respective radial velocities of the primary and secondary components, showing the expected sinusoidal variations of a circular orbit.

individual star. This process is frequently complicated by the faintness of some companions, the blending of spectral lines from stars with similar temperatures, and the effects of rotational broadening, where fast-spinning stars smear out their spectral lines (Torres et al., 2017).

While isolated binaries are classified as single-lined or double-lined, based on the number of visible components in the spectrum, higher-order multiples introduce further complexity. As a highly luminous star can outshine its fainter companions, a quadruple system might observationally appear as merely SB1 or SB2. However, in the best-case scenario, the composite spectrum can exhibit three or even four distinct sets of spectral lines, designated as SB3 and SB4 systems, respectively (Kostov et al., 2022a). An example of an SB4 system, where all four individual line profiles are visible, is presented in Figure 3.2.

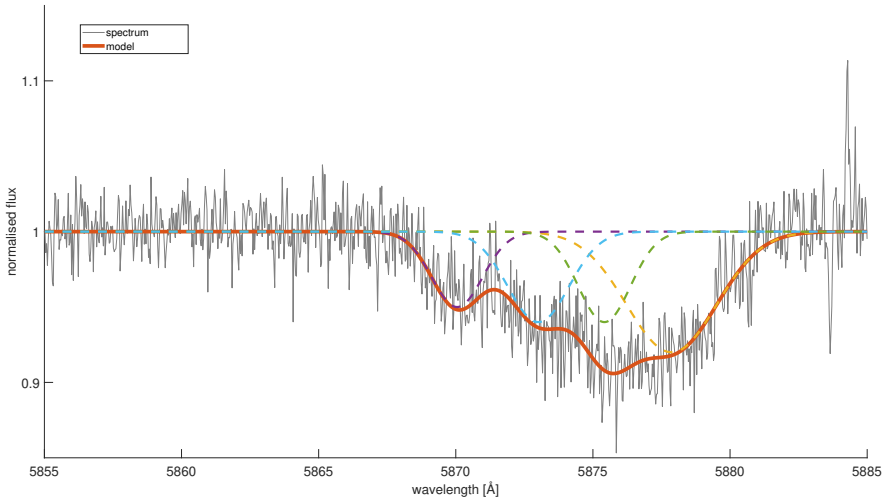

Figure 3.2: A section of the normalised observed spectrum of the SB4 system ASASSN-V J233336.79+615012.0 (grey solid line) in the region of the He I 5876 Å absorption line. The thick orange line represents the composite synthetic model fitted to the data. The individual dashed lines illustrate the modelled line profiles for each of the four stellar components, clearly demonstrating the quadruple nature of the system (Janík, J., 2026, private communication) (Kolář et al., 2026).

Furthermore, the orbital mechanics of hierarchical systems alter the observed radial velocities. As mentioned above, in an isolated binary, the systemic centre-of-mass velocity is constant. However, in multiple stellar systems, the systemic velocities of the individual binaries are not constant. Instead, they periodically change over long timescales as the binaries orbit their common barycentre (Zasche et al., 2022a).

Chapter 4

Software

4.1 Muniwin

Muniwin v2.1.34, also known as C-Munipack (Motl, 2010), is a software application designed for processing astronomical images. It employs aperture differential photometry to generate light curves from observed night sky images. The software also supports the creation of calibration frames, such as master darks and master flat field frames, which are essential for accurate image correction and processing. The complete frame processing procedure in Muniwin has been previously described by Pačková (2024). For the observational data analysed in this thesis, all scientific images were corrected using these master calibration frames, and the extracted light curves were subsequently used for further analysis.

4.2 SILICUPS

SILICUPS (Simple Light CUrve Processing System) (Cagaš, 2016; Pejcha et al., 2022) is software designed to work with light curves of variable stars. Light curves can be displayed either as time series or phased series and fitted with phenomenological models based on Mikulášek (2015). The software also enables the determination of minima timings required to construct $O-C$ diagrams. In cases where multiple variable signals are present (for example, in multiple stellar systems), they can be separated into individual signals, a process known as disentanglement. This procedure is iterative and typically requires repeated execution. In the disentanglement of light curves of doubly eclipsing systems, one of the pairs (pair A), usually the brighter or more clearly defined one, is first phased according to its ephemerides and period, and then roughly fitted. The resulting fit is subtracted from the original data, leaving only the contribution of the second pair (pair B) in the residuals. Pair B is then phased and fitted in the same way. Its fit is subsequently subtracted from the original data phased using pair B's parameters, leaving pair A in the residuals. The process is then repeated iteratively until

the shapes of the fitted light curves and the final residuals no longer change between consecutive iterations, indicating that further steps are unnecessary.

4.3 *TESS* Data Retrieval

To obtain the light curves, the Python package `lightkurve` (Lightkurve Collaboration et al., 2018) was utilised to perform differential aperture photometry on *TESS* Full Frame Images (FFIs), adapting a script originally written by Ondřej Pejcha (Pejcha, 2020) (see Listing A.1). For the target coordinates, FFI cutouts were retrieved, and a strict quality bitmask ('hardest') was applied to filter out degraded data points. An aperture mask was defined to isolate the target star's flux, and an inverse mask was used to select pixels with near-zero flux to estimate and subtract the local background noise. To remove instrumental and long-term trends, the background-subtracted light curves were normalised via the `flatten()` function. The differential light curve was then computed by comparing the target system to a chosen comparison star. Finally, the observation times were converted to Barycentric Julian Date (BJD), and these final, detrended differential light curves were saved to be disentangled in SILICUPS (see Section 4.2).

4.4 PHOEBE 2

Physical models of the light curves and radial velocity curves were constructed using the PHOEBE 2 (v2.4.22) (PHysics Of Eclipsing BinariEs) (Prša et al., 2016) software framework. PHOEBE 2 is an open-source Python package designed for modelling eclipsing binaries. In contrast to the legacy PHOEBE 0.32 (Prša & Zwitter, 2005), which comes with a GUI, PHOEBE 2 is operated exclusively within a Python environment.

PHOEBE 2 was selected for several reasons. The original PHOEBE 0.32 legacy code was based on the Wilson–Devinney method (Wilson & Devinney, 1971); however, as demonstrated by Prša et al. (2016), it can no longer produce adequate fits when applied to high-precision photometry (e.g., *TESS* or *Kepler*). PHOEBE 2 was written from scratch to account for effects that previously caused systematic errors and led to degenerate solutions. Furthermore, Prša et al. (2016) noted that the legacy framework is unsuitable for accurately modelling multiple stellar systems.

Specifically, PHOEBE 0.32 utilised a trapezoidal grid to mesh stellar surfaces, which often resulted in disconnected or overlapping elements and holes. PHOEBE 2 replaces these with a triangular mesh, ensuring seamless surface coverage (Prša et al., 2016).

The framework also incorporates detailed, modern atmosphere tables, such as Castelli & Kurucz (2003) models and the PHOENIX 3D non-local thermodynamic equilibrium

models developed by Husser et al. (2013) (see Prša et al., 2016; Jones et al., 2020, for implementation details).

To refine and improve the model fit, PHOEBE 2 offers several optimisation algorithms, including Nelder-Mead (Nelder & Mead, 1965), Powell (Powell, 1964), and conjugate gradient methods (Conroy et al., 2020). For this study, the Nelder-Mead optimiser was selected due to its efficiency in finding the point of minimal χ^2 across a multi-parameter space (Willems, 2025). Because Nelder-Mead is a local optimiser, it is most effective when parameters are already in the general vicinity of the optimal solution. PHOEBE 2 provides built-in estimators, although the user can also manually establish initial parameter guesses based on prior knowledge of the system to roughly approximate the light curve.

Unfortunately, modelling in PHOEBE 2 is computationally intensive. During the Nelder-Mead optimisation, initial exploratory runs were limited to approximately 80 iterations (requiring 50–80 minutes of computation time per run) to approach the correct parameters. The final model optimisation utilised 150 iterations (100–120 minutes). To prevent the optimiser from wandering into physically impossible local minima, highly correlated parameters were grouped together, and strict boundaries were applied.

Once a fit was secured, the adopted values served as the foundation for estimating parameter uncertainties using a Markov Chain Monte Carlo (MCMC) probabilistic sampler, which uses a sequence of random samples to thoroughly map the posterior distribution.

Physical modelling in PHOEBE 2 requires significant processing power. Although the Nelder-Mead optimisations were performed on a standard personal computer, running the MCMC with a sufficient number of iterations locally would be unfeasible. Fortunately, it was possible to carry out the computationally heavy MCMC on the MetaCentrum computing infrastructure. While having access to the cluster for the MCMC phase was essential for this study, future research will aim to secure dedicated computational time. Running the complete modelling process on high-performance facilities would reduce overall runtimes and allow for more iterations without hardware constraints.

Because this study focuses on quadruple systems, it is important to note that the advanced capability to comprehensively model multiple stellar systems is currently in a development version of PHOEBE. As it is still in development, this feature is not yet included in the official PHOEBE repository (Brož et al., 2025).

4.5 OCFit

OCFit v0.2.2 (Gajdoš & Parimucha, 2019) is a software designed to analyse $O-C$ diagrams for eclipsing binaries and transiting exoplanets. Its primary application is modelling periodic variations caused by phenomena such as apsidal motion, the Light-

Time Effect, and mass transfer (Gajdoš, 2023). Upon entering the observed times of minima, the software calculates the predicted ephemerides to generate the corresponding $O-C$ values, which can be fitted using standard analytical models (Gajdoš, 2023).

To obtain a robust first guess of the orbital parameters, OCFit utilises a combination of optimisation algorithms, such as Genetic Algorithms or Differential Evolution. Following this initial parameter estimation, a Markov Chain Monte Carlo (MCMC) method is employed to refine the fit and determine the parameter uncertainties. For simpler cases requiring only linear or quadratic ephemeris updates, the software offers standard linear regression, iterative robust regression, and MCMC sampling (Gajdoš, 2023).

4.6 Spectral Data Reduction

The majority of the spectroscopy observations analysed in this work were obtained using the PLATOSpec echelle spectrograph (Kabáth et al., 2026). Consequently, the data acquisition procedures described below reflect the specific protocols required for this instrument.

For proper spectral processing and analysis, calibration spectra must be observed. Calibration frames consist of a series of bias frames, which are zero-exposure frames used to map electronic readout noise (typically 10 at the start and 10 at the end of the night), flat field frames, which are exposures of a uniform continuum source (LED lamp), and a comparison spectrum. Flat field frames are made in three different configurations: with both fibres illuminated, with only the scientific object fibre illuminated, and with only the calibration Thorium-Argon (ThAr) fibre illuminated.

Then, the scientific spectrum (spectrum of the object) is observed. While it is possible to expose the calibration spectrum and scientific spectrum simultaneously, this can lead to signal contamination where the saturated ThAr lines bleed into the science target spectrum, particularly in the red region of the spectrum. To avoid this, a 60-second ThAr exposure is taken immediately before and after every scientific observation.

The reduction and analysis of the measured scientific and calibration spectra were performed using the IRAF software package (Tody, 1986). The bias frames are combined into a master bias, which is subtracted from all other frames. Similarly, the bias-corrected flat field frames are combined into a master flat. This master flat is utilised for the extraction of the apertures, meaning identifying the orders of spectra and the extraction of flux in individual orders. The comparison spectra are then calibrated, a process that includes the removal of outliers (ThAr lines whose measured position after conversion to radial velocity deviates from tabulated laboratory values by more than $0.5\,\mathrm{km\,s^{-1}}$).

The flux from the scientific spectrum is extracted in pixels for each order. During this process, cosmic rays (high-energy particles) that appear as bright hits on the CCD are identified and removed. A flat is also used to flatten the spectrum. The data

are in pixels, but are needed in wavelengths; therefore, the wave calibration must be performed. Consequently, numerous spectral lines must be identified throughout the whole spectrum. Because the wave calibration is with respect to laboratory wavelengths, a Doppler correction is applied (heliocentric and barycentric). Finally, the continuum of the object is fitted and divided out, resulting in a normalised spectrum. This step prepares the data for spectral disentangling and further analysis.

In the case of a doubly eclipsing system, the observed spectrum comprises the blended light of four stars and must be disentangled in order to extract the individual radial velocities. The disentanglement of these composite spectra was performed using the Gaussian process–based method described by Czekala et al. (2017). While the original approach was demonstrated for spectroscopic binaries, Jan Janík extended the model to account for additional components, making it applicable to doubly eclipsing systems.

Unlike other methods, such as cross-correlation, which depend on pre-existing stellar templates, or Fourier techniques, which often struggle with the low-order features and can create wavy patterns in the reconstructed spectra, the Gaussian process is non-parametric. Rather than relying on theoretical templates or stellar models, it models the spectrum of each component as a smooth, continuous function.

At any given epoch, the observed data are treated as the sum of the four individual stellar spectra, Doppler-shifted according to their orbital velocities. The algorithm simultaneously optimises both the orbital parameters and the shape of the individual spectra. This method can distinguish between true stellar spectra and observational noise, making it suitable for data with a low signal-to-noise ratio. In doubly eclipsing binaries, the presence of third light (contamination from the other pair) reduces the contrast of the spectral lines, limiting the precision of the disentanglement.

Chapter 5

Data analysis

This chapter presents a comprehensive analysis of the two doubly eclipsing quadruple candidates, S1 CMi and S4 Vel. Because the derivation of the fundamental stellar parameters is tied to the physical interpretation of the models, the methodology, results, and immediate discussion for each system are presented within this chapter. The analysis begins with a description of the selected targets and the data collection process, including both space-based *TESS* photometry and ground-based observations. Subsequent sections detail the disentanglement of the light curves, the determination of minima timings, the construction of $O-C$ diagrams to identify Light-Time Effects, and an independent SED analysis. Finally, the chapter details the physical modelling using PHOEBE 2 to derive the absolute and geometric parameters of the systems.

5.1 Objects

Two candidates for doubly eclipsing binaries were chosen for detailed analysis. The main selection criteria were the brightness of each system and the orbital periods of the individual eclipsing binaries. These parameters were chosen to ensure successful observation of the targets using the available ground-based telescopes, as faint systems or those with long periods would be too difficult to monitor. Given Masaryk University's access to observatories in both the Northern and Southern hemispheres (Czech Republic and South Africa), the selection was not limited by geographical location (a full list of observers is provided in Tables A.1 and A.2 in the Appendices). Additionally, the photometric observations were supplemented by observations from China, conducted by Michal Haltuf.

A major objective of this study was to complement the photometric data with radial velocity measurements to better constrain the physical parameters of the systems. The majority of the spectra were acquired by Jan Janík using the PLATOSpec instrument, while an additional set of spectra was obtained by Thibault Merle and Nikolai Shchechilin using the HERMES spectrograph.

Both systems were chosen from a list of potential candidates provided by the Squadra group, which investigates doubly eclipsing systems. For clarity, both candidates have been assigned new names derived from the constellations in which they are located. The first system, TYC 168-784-1, has been renamed S1 CMi (from Canis Minoris), while the second system, V0432 Vel, will be referred to as S4 Vel (from Velorum). Detailed information about the systems is presented in Tables 5.1 and 5.2.

Table 5.1: Information about the system TYC 168-784-1.

Parameter	Value	Source
Right ascension J2000 Declination J2000	$07^{\mathrm{h}}\ 22^{\mathrm{m}}\ 16.202^{\mathrm{s}}$ $3°1'54.929''$	Gaia Collaboration (2023)
Eclipsing binary type Magnitude range (V) Spectral type	EA + EA 10.33–10.54 A2IV	Watson et al. (2006) Luo et al. (2022)
P_{A} (days) $M_{0,\mathrm{A}}$ (HJD)	3.526276 2458507.8495	Kostov et al. (2022b)
P_{B} (days) $M_{0,\mathrm{B}}$ (HJD)	3.733625 2458499.5708	Kostov et al. (2022b)

Table 5.2: Information about the system V0432 Vel.

Parameter	Value	Source
Right ascension J2000 Declination J2000	$10^{\mathrm{h}}\ 42^{\mathrm{m}}\ 06.487^{\mathrm{s}}$ $-42°52'40.720''$	Gaia Collaboration (2023)
Eclipsing binary type Magnitude range (V) Spectral type	EA + EA 9.04–9.22 F2V	Zasche et al. (2022b) Otero & Dubovsky (2004)
P_{A} (days) $M_{0,\mathrm{A}}$ (HJD)	1.46857 2459288.820	Freund et al. (2022)
P_{B} (days) $M_{0,\mathrm{B}}$ (HJD)	0.5449716 2459288.528	Freund et al. (2022)

5.2 Data collection

Photometric data have been acquired from various surveys, including APASS (Henden et al., 2015), ASAS (Pojmanski, 2002), ASAS-SN (Shappee et al., 2014), ATLAS (Tonry et al., 2018), DASCH (Grindlay et al., 2012), *Hipparcos* (Perryman et al., 1997), *INTEGRAL* OMC (Winkler et al., 2003), MMT-9 (Beskin et al., 2017), SuperWASP (Pollacco et al., 2006), and *TESS* (Ricker et al., 2015), as well as through observations

with available ground-based telescopes. Unfortunately, much of the data were of insufficient quality; therefore, the light curves could not be disentangled. However, in some cases, it was possible to use the low-quality data to determine at least one minimum timing, most often corresponding to the primary eclipse.

5.2.1 *TESS*

The Transiting Exoplanet Survey Satellite (*TESS*) (Ricker et al., 2015) is a NASA mission dedicated primarily to the discovery of exoplanets. It monitors large areas of the sky in order to detect periodic variations in stellar brightness caused by planetary transits. Although the mission was designed to study exoplanets, its high-precision photometry has also become an invaluable tool for the variable star community.

The satellite surveys the sky in sectors (initially 13 sectors per hemisphere), with each sector observed continuously for 27.4 days, which corresponds to two orbits of the satellite around the Earth. This uninterrupted coverage makes it possible to capture complete variability cycles for many systems. Since its launch in April 2018, the satellite has operated beyond its initial planned lifespan and, by March 2026, it is projected to have scanned its 100th sector.

As described in Ricker et al. (2015), the mission primarily focuses on main-sequence dwarf stars (spectral types F5–M5) with a limiting magnitude of $I_c \lesssim 10$–13 mag. However, as demonstrated in Pačková (2024), the data gathered from *TESS* are not limited to such bright stars, and it is possible to successfully utilise *TESS* photometry for fainter objects ($V \approx 15.2$ mag).

An overview of the available sectors for both systems is provided in Table 5.3. Unfortunately, not all of these sectors yielded usable data. Specifically, Sectors 9 and 63 had to be excluded from the analysis. For these sectors, visual inspection of the generated FFI cutouts revealed that the target star was not properly captured on the detector during the observation period, meaning no valid photometric light curve could be extracted. An example of an unusable sector's cutout is shown in Figure 5.1a, compared to a properly captured target from Sector 90 in Figure 5.1b. For the extraction of the photometric light curves from the valid sectors, TYC 168-1539-1 was used as the comparison star for S1 CMi, while TYC 7731-1057-1 was used for S4 Vel.

Table 5.3: An overview of the different sectors available from *TESS*.

Sector	Year	Cadence (s)	System
07	2019	1800	S1 CMi
33	2020	600	S1 CMi
87	2024	200	S1 CMi
09	2019	1800	S4 Vel
10	2019	1800	S4 Vel
36	2021	600	S4 Vel
63	2023	200	S4 Vel
90	2025	200	S4 Vel

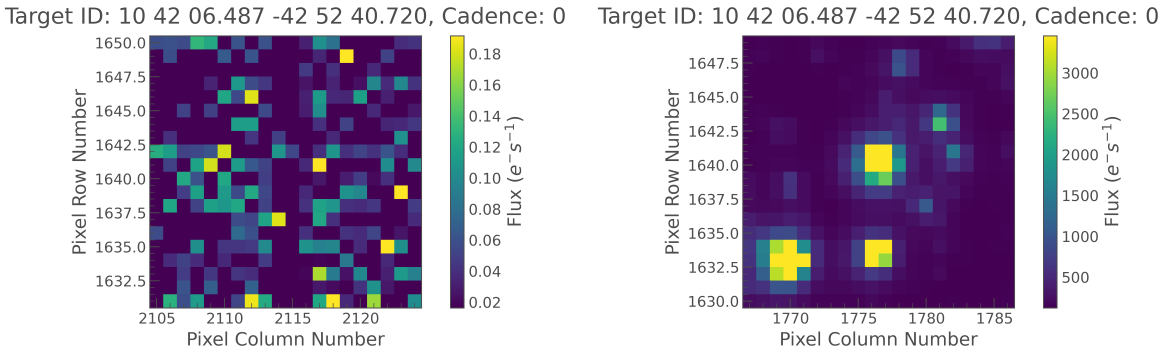

(a) Sector 63 (2023)

(b) Sector 90 (2025)

Figure 5.1: Comparison of *TESS* target pixel maps (for S4 Vel): unusable Sector 63 (left) versus usable Sector 90 (right).

Following the disentanglement of the *TESS* light curves into individual binary pairs, detrending was applied to eliminate long-term systematic and instrumental variations. This correction was performed using a custom Python script developed by Jakub Kolář (Listing A.2 in the Appendices). The systematic trend was modelled by fitting a Chebyshev polynomial to the observational residuals, with the polynomial order optimised individually for each dataset based on the specific trend characteristics. The fitted polynomial was subsequently subtracted from the original observations, yielding a flattened, fully detrended light curve suitable for modelling.

5.2.2 Observations

The photometric data were obtained from two observatories located in both the Northern and Southern hemispheres. In the Northern hemisphere, observations were conducted at the Ždánice Observatory in the Czech Republic using an 800 mm Ritchey-Chrétien telescope. In the Southern hemisphere, data were collected at the Boyden Observatory near Bloemfontein, South Africa, using a 355 mm Schmidt-Cassegrain telescope.

Observations for both candidate systems were acquired primarily in Sloan g' and r' filters. Additional data were obtained in the Sloan i' filter, as well as the Johnson V and R passbands. The V and R band observations were conducted using a 318 mm Dall-Kirkham telescope situated at the Gemini Remote Observatory in Lijiang, China. Although these additional observations were insufficient for constructing complete light curves, they proved highly valuable for determining times of minima. A complete summary of all photometric observations can be found in Tables A.1 and A.2 in the Appendices.

The raw photometric frames were processed using the Muniwin software (described in Section 4.1). Processed field frames illustrating the observed fields of view for both systems are presented in Figure 5.2. Afterwards, all observations were combined, and the light curves were disentangled using the SILICUPS software (see Section 4.2).

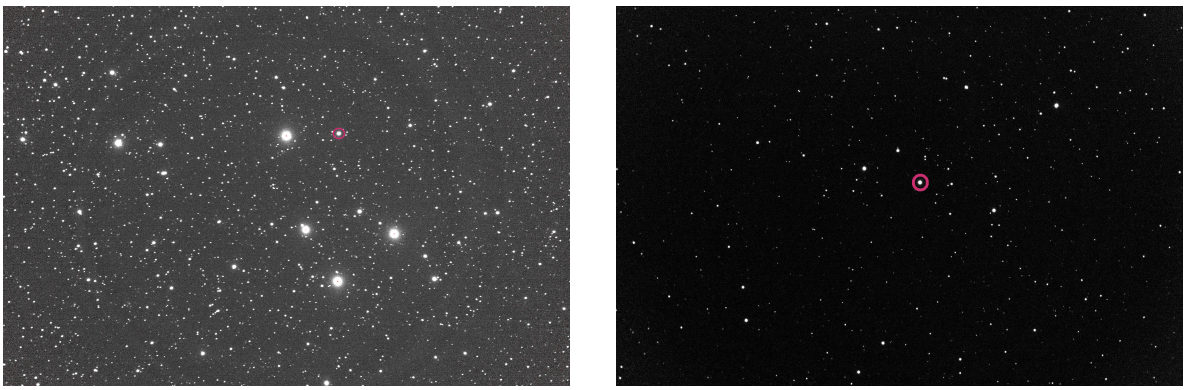

(a) S1 CMi (b) S4 Vel

Figure 5.2: Processed field frames from the Boyden Observatory for the systems S1 CMi (left) and S4 Vel (right). The target systems are highlighted with pink circles.

High-resolution spectroscopic data for both systems were obtained primarily using the PLATOSpec echelle spectrograph on the 1.52 m telescope at ESO's La Silla Observatory (Kabáth et al., 2026). Additional spectra were acquired with the HERMES spectrograph at the 1.2 m Mercator telescope on La Palma (Raskin et al., 2011). The full logs of all spectroscopic observations are provided in Appendices in Tables A.3 and A.4. In order to derive radial velocity data, observations were processed as described in Section 4.6.

To illustrate the quality of the acquired data and the variations in the line profiles, Figure 5.3 presents a sample of the individual 1D spectra. The plot focuses on the spectral window surrounding the Fe II (4549 Å) absorption line using a constant vertical offset. For visual clarity, successive normalised spectra have been vertically shifted along the y-axis. This representation clearly demonstrates the changing shape and position of the spectral lines due to the Doppler shift induced by the orbital motion of the system components.

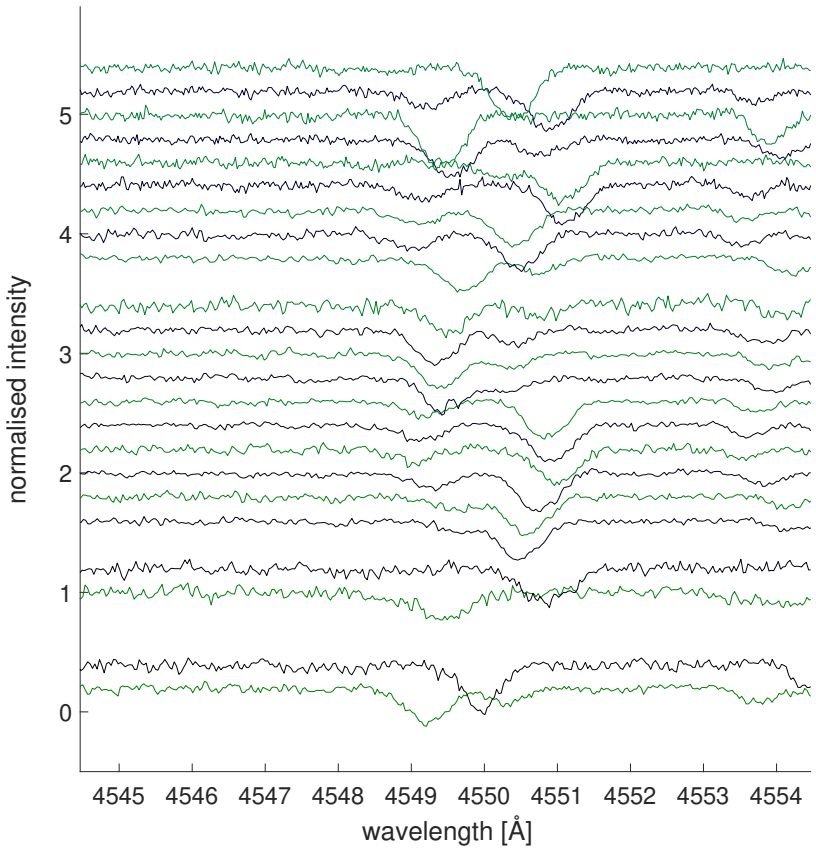

Figure 5.3: Stacked spectra for the system S1 CMi centered around the Fe II (4549 Å) line. The observations are vertically offset for better visibility.

Figures 5.4a and 5.4b display dynamic spectra for pairs A and B of the system S1 CMi, respectively. Both plots illustrate how the profile of the Fe II (4549 Å) absorption line changes as a function of the orbital phase (φ_{A} and φ_{B}). The colour scale represents the normalised flux, where the background continuum is shown in red ($\sim$1.0), and the depth of the absorption line is traced by the cooler colours. The vertical white bands visible in the figures indicate phases for which observations were not available. Despite these gaps, a clear periodic Doppler shift is apparent in both cases. For each pair, this visible sinusoidal trace reflects the orbital motion of the primary stellar component around the pair's centre of mass. The absorption lines of the secondary components are too weak to be detected in this specific spectral window.

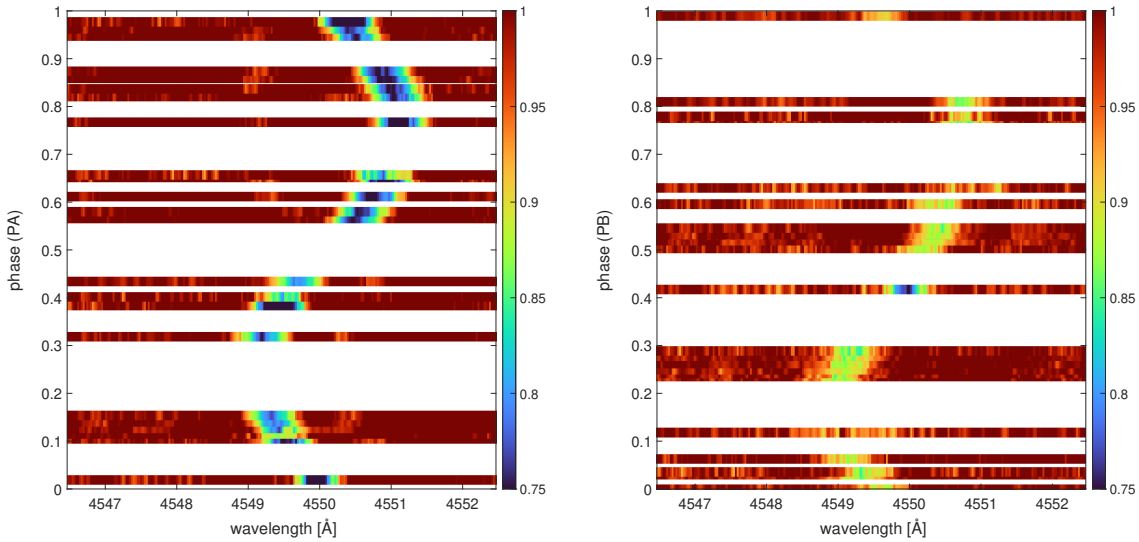

(a) Dynamic spectrum for the pair A.

(b) Dynamic spectrum for the pair B.

Figure 5.4: Dynamic spectra of the Fe II (4549 Å) absorption line for the system S1 CMi.

5.2.3 Minima Timing Determination

The minima timings used to construct the $O-C$ diagrams were determined using three distinct approaches, depending on the quality and continuity of the data.

For highly precise, continuous datasets, the SILICUPS software (see Section 4.2) was employed. This approach utilises the phenomenological modelling function introduced by Mikulášek (2015). The software provides the flexibility to determine timings either by manually defining the boundaries of individual eclipses or by fitting multiple minima simultaneously across the entire light curve.

The second approach utilised a Python script developed and described in detail by Kolář (2025). This method is specifically designed for non-continuous observations (such as ground-based data). The script requires a synthetic reference model (generated via SILICUPS), along with the phase-folded photometric data. It operates by searching for the exact phase shift required to align the observed data points with the reference model. Ground-based data rarely capture a complete light curve in a single night; instead, it often takes several weeks or months to collect enough data to cover the entire phase. Because all individual observations must be combined into a single phase curve, the script cannot measure the timings of individual eclipses. Instead, it produces one average timing for the primary and secondary eclipses, assigned to the midpoint of that observing season (Kolář, 2025).

Finally, for poorer-quality datasets, where, for example, only the primary eclipse of pair A was clearly visible, a manual method was applied. This technique involved identifying a specific data point within the eclipse that visually intersected the theoretical

fit. By extracting this point's phase value and multiplying it by the period, the exact time difference between that observation and the true minimum could be calculated. Adding or subtracting this time difference from the data point's original observational time (depending on whether the observation occurred on the descending or ascending branch of the eclipse) provided a reliable estimate for the time of minimum. Because this method relied on visual alignment, standard errors could not be automatically calculated. Instead, the uncertainties for these specific timings were estimated by varying the reference epoch T_0 to establish the maximum acceptable shift. The error value was defined as the point at which the visual alignment between the data and the theoretical model noticeably degraded.

5.3 Photometric Results

5.3.1 *TESS* Photometry for S1 CMi

The final disentangled *TESS* phase curves for the system S1 CMi are displayed in Figures 5.5a and 5.6a for pair A, and Figures 5.5b and 5.6b for pair B. The difference in observational cadence between *TESS* Sector 7 (Figure 5.5) and Sector 33 (5.6) is clearly visible.

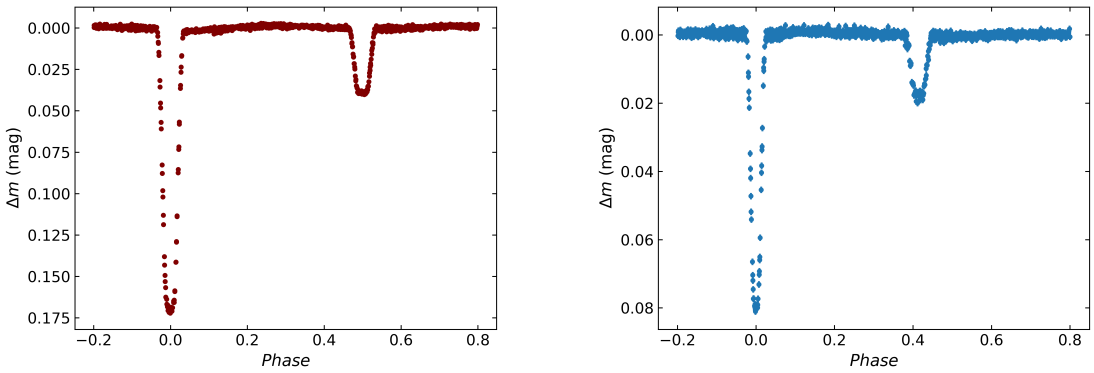

(a) Pair A

(b) Pair B

Figure 5.5: Phase curves of pair A (left) and pair B (right) for the system S1 CMi, *TESS* Sector 7 (2019).

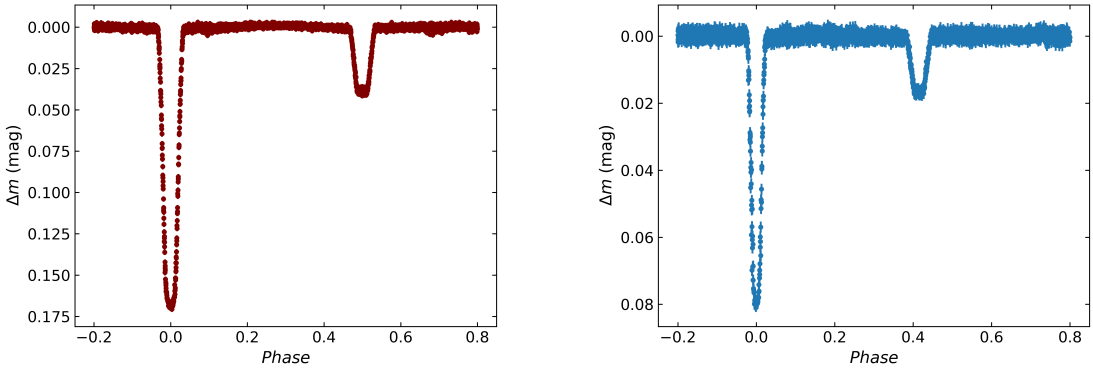

(a) Pair A (b) Pair B

Figure 5.6: Phase curves of pair A (left) and pair B (right) for the system S1 CMi, *TESS* Sector 33 (2020).

5.3.2 *TESS* Photometry for S4 Vel

Figures 5.7a, 5.8a, 5.9a, 5.10a, and 5.11a represent the disentangled *TESS* phase curves of the system S4 Vel for pair A. Figures 5.7b, 5.8b, 5.9b, 5.10b, and 5.11b show the corresponding phase curves for pair B. Due to the high observational cadence in Sector 90, the data were divided into two segments for better visual clarity (Figures 5.10 and 5.11). In the phase curves of pair B, there are noticeable changes between phases 0.1 and 0.4 across the different sectors, causing this part of the phase curve to appear thicker. This broadening occurs because the out-of-eclipse maxima are not constant, but rather vary in amplitude between individual orbits. A detailed, sector-by-sector view illustrating these changes is presented in Figure A.2 in the Appendices. These variations are likely caused by starspots on the secondary star.

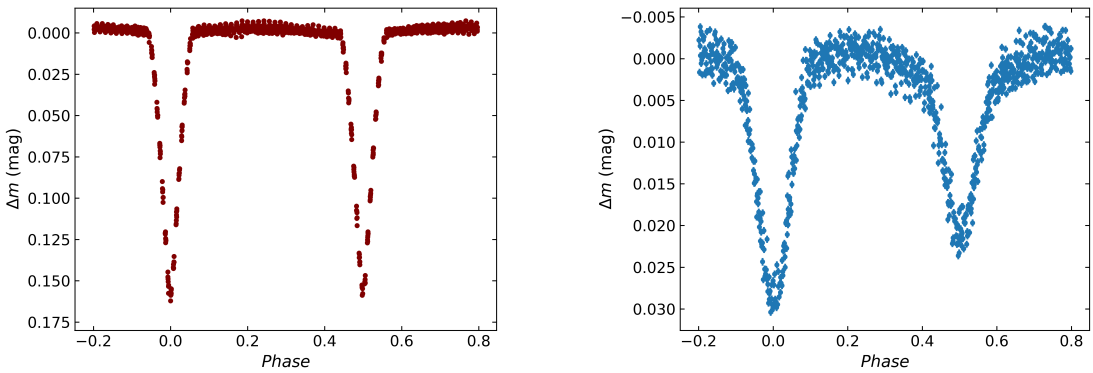

(a) Pair A (b) Pair B

Figure 5.7: Phase curves of pair A (left) and pair B (right) for the system S4 Vel, *TESS* Sector 9 (2019).

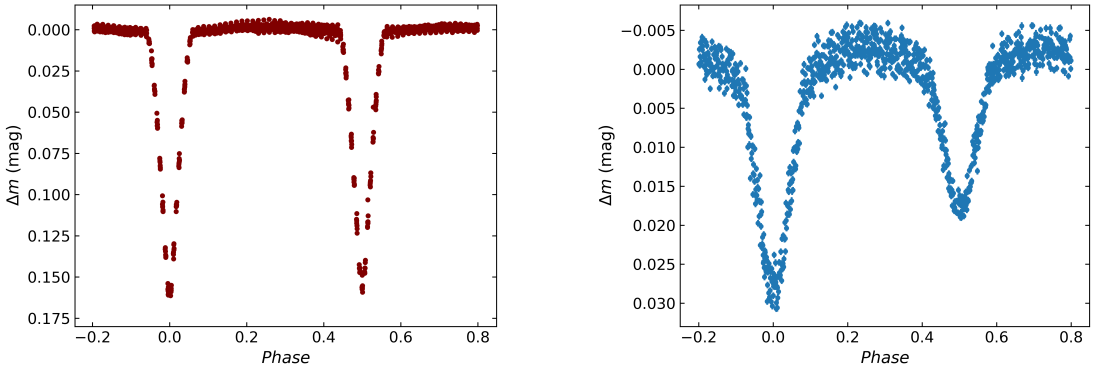

(a) Pair A

(b) Pair B

Figure 5.8: Phase curves of pair A (left) and pair B (right) for the system S4 Vel, *TESS* Sector 10 (2019).

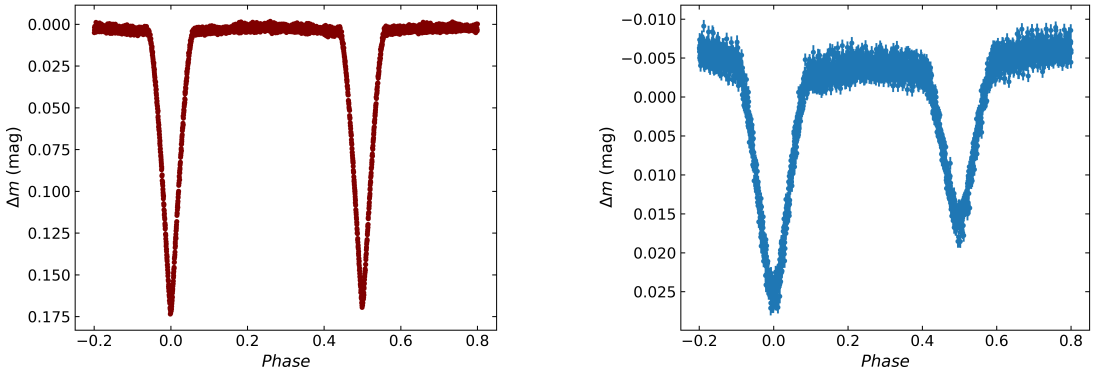

(a) Pair A

(b) Pair B

Figure 5.9: Phase curves of pair A (left) and pair B (right) for the system S4 Vel, *TESS* Sector 36 (2021).

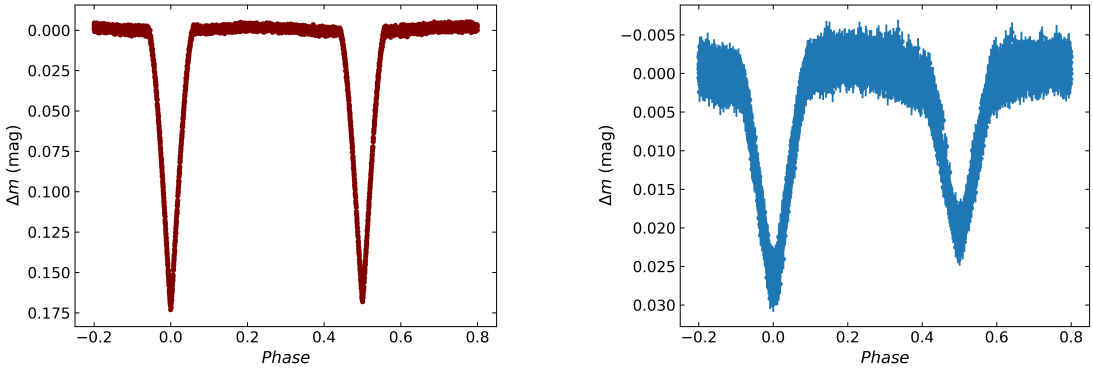

(a) Pair A

(b) Pair B

Figure 5.10: Phase curves of pair A (left) and pair B (right) for the system S4 Vel, *TESS* Sector 90 (2025), first half.

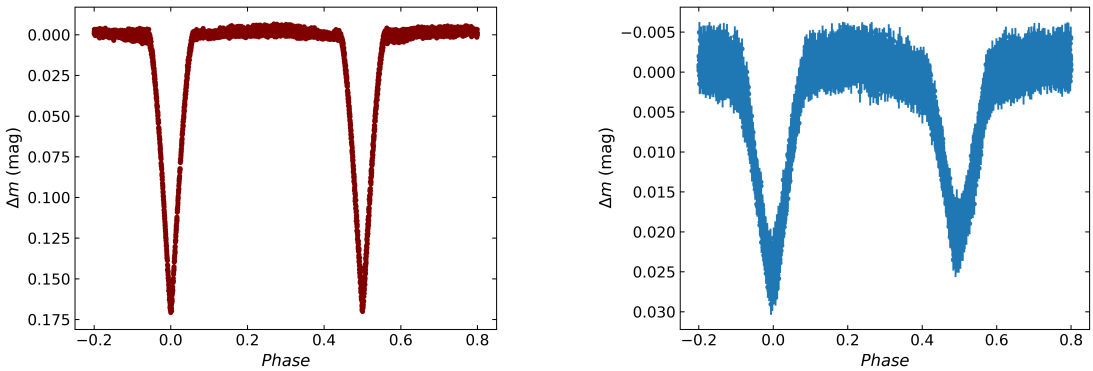

(a) Pair A

(b) Pair B

Figure 5.11: Phase curves of pair A (left) and pair B (right) for the system S4 Vel, *TESS* Sector 90 (2025), second half.

5.3.3 Ground-based Photometry for S1 CMi

The ground-based phase-folded light curves for the system S1 CMi in the g' and r' bands are presented in Figures 5.12a and 5.13a for pair A, and Figures 5.12b and 5.13b for pair B. It is noticeable that the phase curves of both pairs exhibit significant gaps in their out-of-eclipse phase coverage. This incomplete coverage is a consequence of their longer orbital periods (approximately 3.5 and 3.7 days, respectively), which makes capturing the entire phase curve with ground-based telescopes challenging. Nevertheless, the primary and secondary eclipses are clearly defined, and the overall morphology of the variations remains consistent with the *TESS* data.

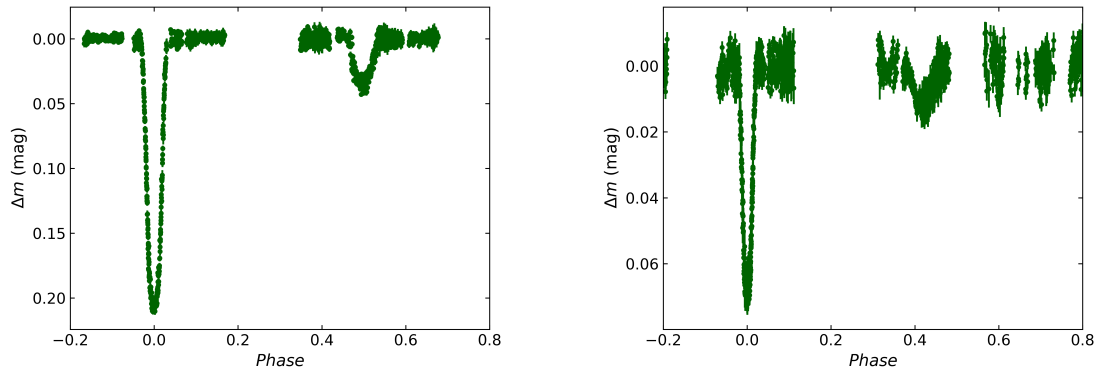

(a) Pair A (b) Pair B

Figure 5.12: Phase curves of pair A (left) and pair B (right) for the system S1 CMi, ground-based observations in the filter g'.

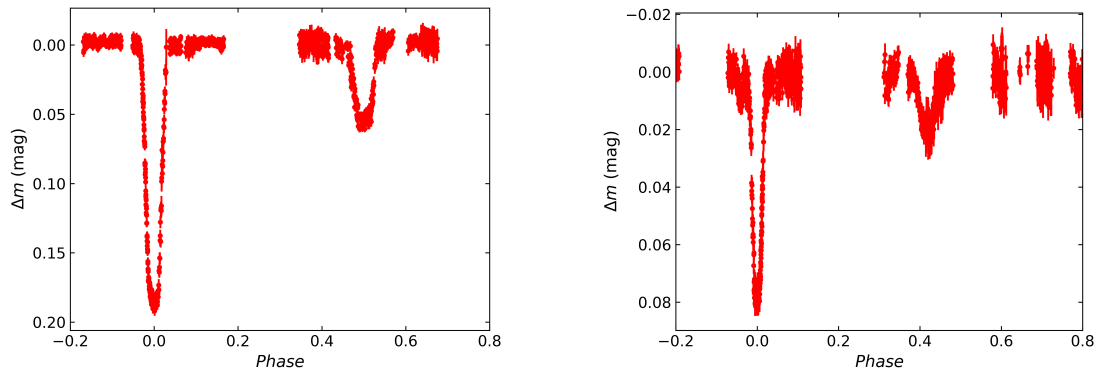

(a) Pair A (b) Pair B

Figure 5.13: Phase curves of pair A (left) and pair B (right) for the system S1 CMi, ground-based observations in the filter r'.

5.3.4 Ground-based Photometry for S4 Vel

Figures 5.14a and 5.15a present the ground-based phase-folded light curves for pair A of the S4 Vel system in the g' and r' bands. Because primarily eclipses were targeted during the observations, there is a gap in the out-of-eclipse coverage. In contrast, for pair B (Figures 5.14b and 5.15b), it was possible to cover the whole phase curve due to its relatively short orbital period. Although the low amplitude of the photometric variations causes the data to visually appear broadened by scatter, the overall shape and brightness changes are fully consistent with the *TESS* data.

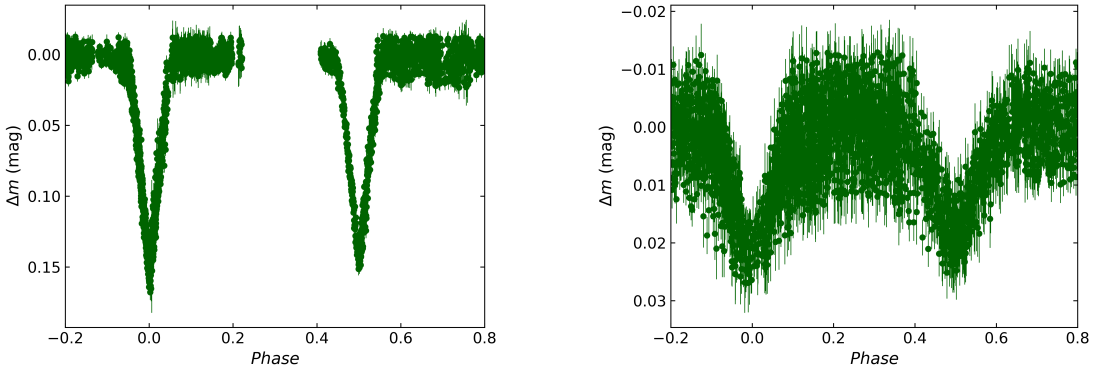

(a) Pair A (b) Pair B

Figure 5.14: Phase curves of pair A (left) and pair B (right) for the system S4 Vel, ground-based observations in the filter g'.

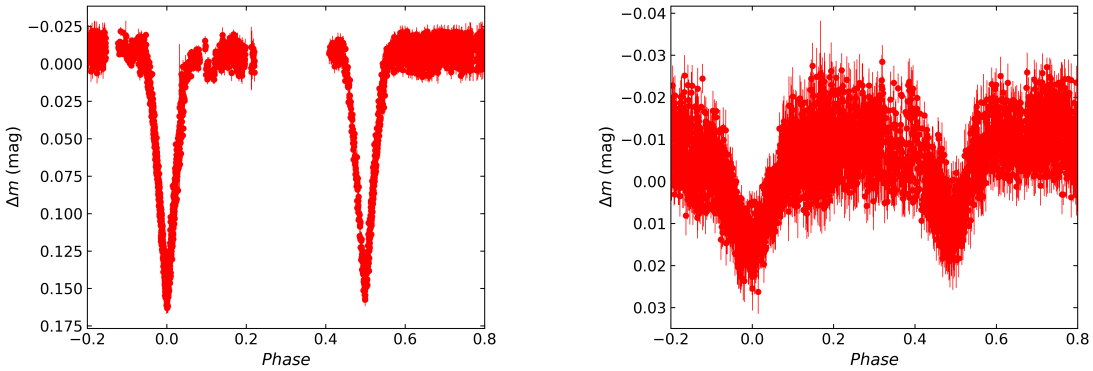

(a) Pair A (b) Pair B

Figure 5.15: Phase curves of pair A (left) and pair B (right) for the system S4 Vel, ground-based observations in the filter r'.

5.4 $O-C$ Diagrams

5.4.1 $O-C$ Diagrams for S1 CMi

For the system S1 CMi, timings of minima were gathered across multiple passbands (g', r', V, R) utilising both ground-based observations and archival databases (ASAS, ASAS-SN, MMT-9, and *TESS*). Incorporating the earliest ASAS measurements was especially important, as these historical points effectively illustrate the long-term curvature of the orbit. The $O-C$ values were computed adopting the ephemeris (T_0 and P) provided in Table 5.1. The resulting $O-C$ values are plotted in Figures 5.16 (pair A) and 5.17 (pair B). A comparison of the two plots reveals a mirror-image geometry, with pair A curving upwards, whereas pair B curves downwards. This anti-correlation is a clear signature of a mutual Light-Time Effect, providing strong evidence that S1 CMi is a gravitationally bound quadruple system. Because of the limited span of the available data, the $O-C$ diagrams only capture a partial segment of the expected sinusoidal pattern associated with the LiTE. Consequently, an exact period for the outer orbit cannot be determined at this time. However, based on the visible curvature and the duration of the current observations, the outer orbital period is constrained to be at least 80 years.

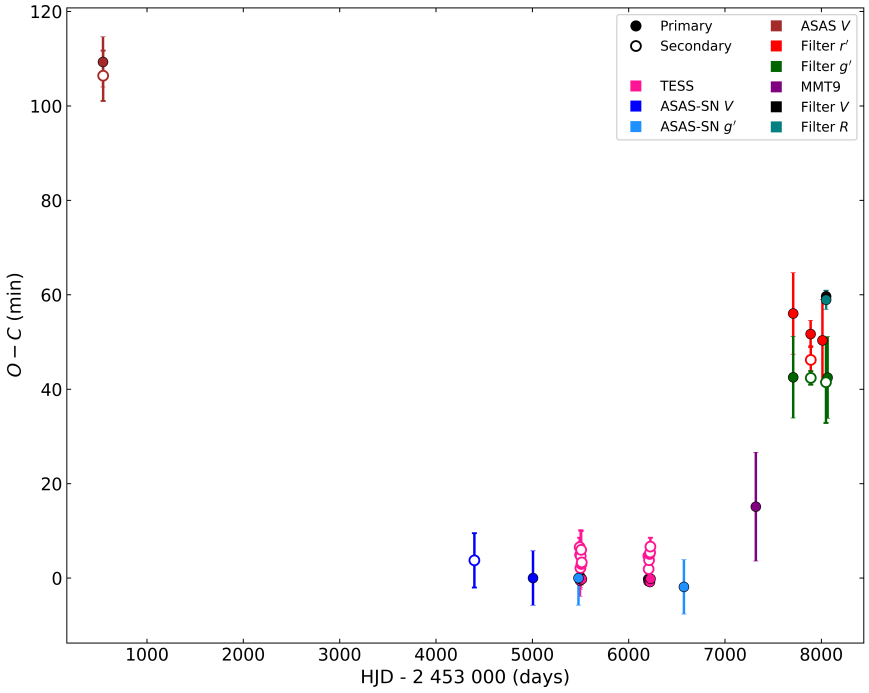

Figure 5.16: $O-C$ diagram for pair A of the system S1 CMi. The calculated times of minima (C) were derived using the standard linear ephemeris (T_0 and P) established in Table 5.1.

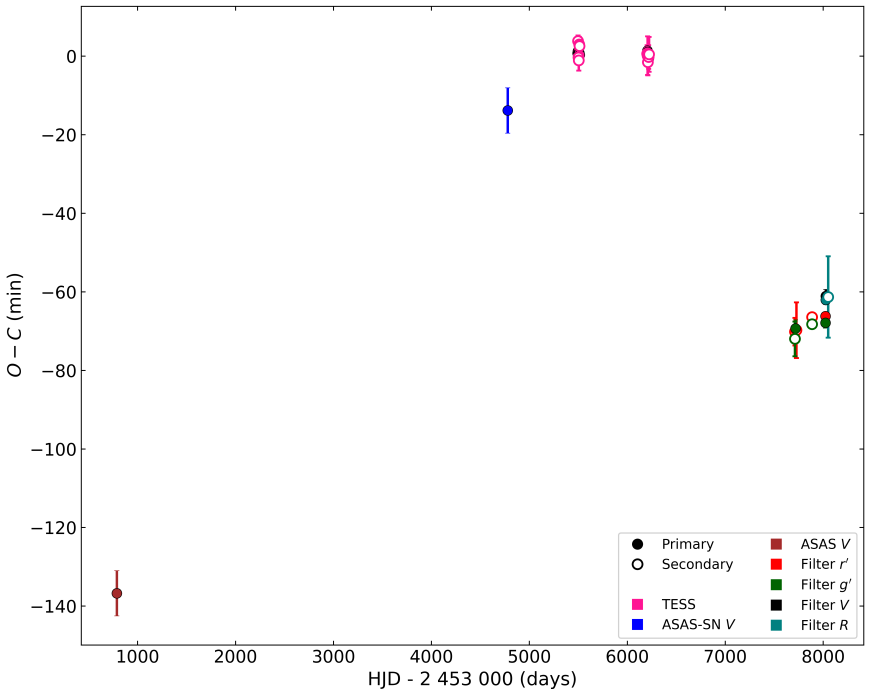

Figure 5.17: $O-C$ diagram for pair B of the system S1 CMi. The calculated times of minima (C) were derived using the standard linear ephemeris (T_0 and P) established in Table 5.1.

Beyond the systemic LiTE, the $O-C$ analysis of pair B uncovered an additional effect: a separation between the primary and secondary minima, which is a classic sign of apsidal motion within an eccentric orbit. Because the LiTE shifts the entire binary uniformly, it was fitted and subtracted from the data. After subtracting the LiTE model, the isolated apsidal motion for pair B becomes evident (Figure 5.18). To further emphasise the opposing trajectories of the primary and secondary minima, the residuals have been symmetrically aligned in Figure 5.19. The period of the apsidal motion, U, was fitted to be approximately 430 years. However, as the available observational baseline only covers a small fraction of the full cycle, this value should be treated as a preliminary estimate or a minimal possible period.

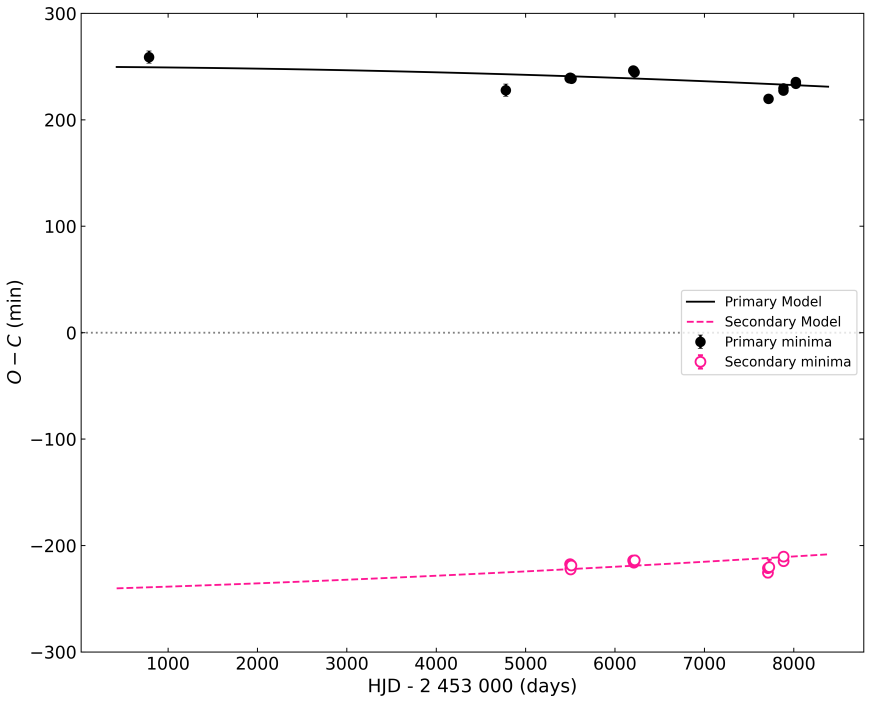

Figure 5.18: $O-C$ diagram for pair B of the system S1 CMi, shown after the subtraction of the LiTE. The data are fitted with an apsidal motion model.

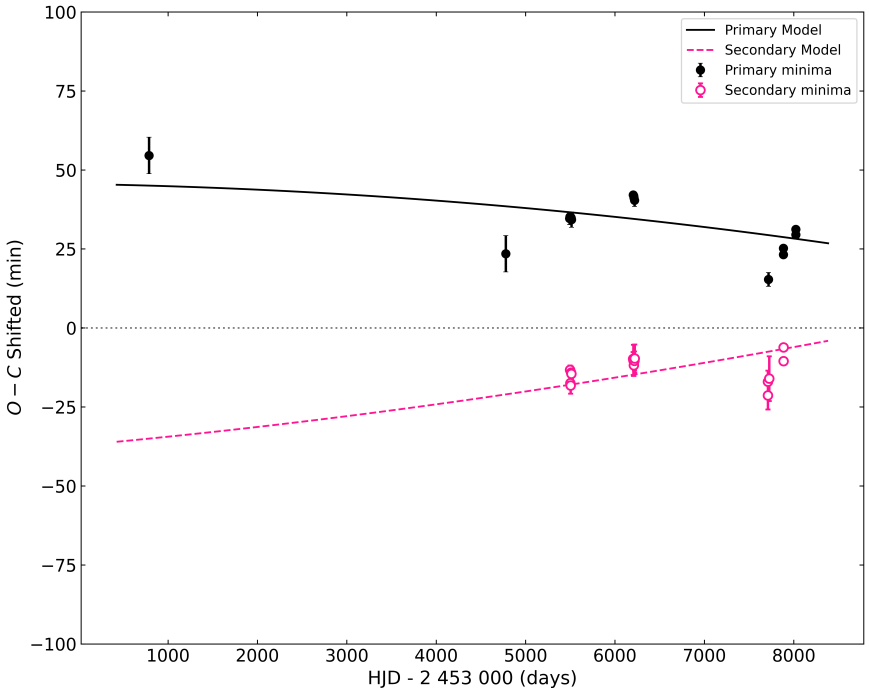

Figure 5.19: $O-C$ diagram of the system S1 CMi, pair B, showing the apsidal motion fit. To clearly visualise the curvature, the primary and secondary minima have been symmetrically shifted by 204.3 min to reduce the vertical gap to 60.0 min.

5.4.2 $O-C$ Diagrams for S4 Vel

To construct the $O-C$ diagrams, minima timings were compiled from a combination of ground-based photometry in filters g', i', and r', space-based *TESS* observations, and publicly available archival data, including ASAS, ASAS-SN, *INTEGRAL* OMC, and SuperWASP. It is important to highlight the two earliest data points in the $O-C$ diagram for pair A, derived from the ASAS archive. While they are separated from the more recent observations by a gap of several years, they are vital as they significantly extend the observational baseline and confirm the long-term non-linear trend of the orbital period. The $O-C$ diagrams for the S4 Vel system are presented in Figures 5.20 and 5.21. For pair A (Figure 5.20), the calculated minima timings were derived using the linear ephemeris (T_0 and P) previously established in Table 5.2. The resulting $O-C$ values exhibit a clear upward trend. For pair B (Figure 5.21), a slightly modified reference period of $P_{\rm ref} = 0.544979$ days was intentionally adopted for the construction of the diagram, while T_0 was retained from Table 5.2. This adjustment was chosen to improve the visual representation and clearly distinguish the downward trend of the data points. Comparing the two diagrams, it is clear that the LiTE is in antiphase, confirming that the system S4 Vel is a gravitationally bound, doubly eclipsing binary. While the antiphase behaviour of the $O-C$ data strongly indicates a bound quadruple system, the current data only cover a fraction of the mutual orbit. Consequently, the full amplitude and period of the LiTE remain unconstrained. Nevertheless, the visible curvature concludes that the outer orbital period must be long, constrained to a minimum of at least 90 years.

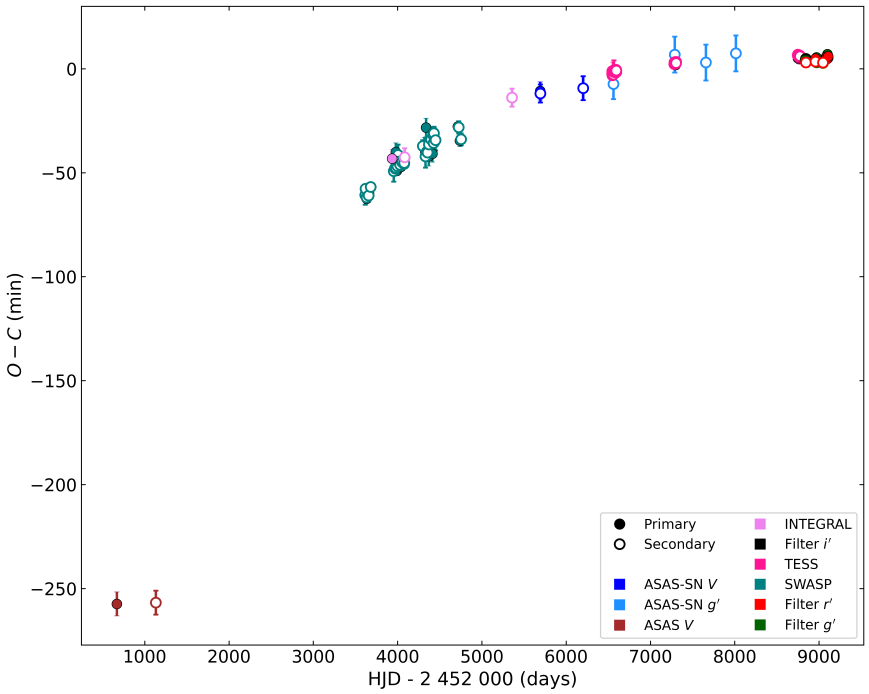

Figure 5.20: $O-C$ diagram for pair A of the system S4 Vel. The calculated times of minima (C) were derived using the standard linear ephemeris (T_0 and P) established in Table 5.2.

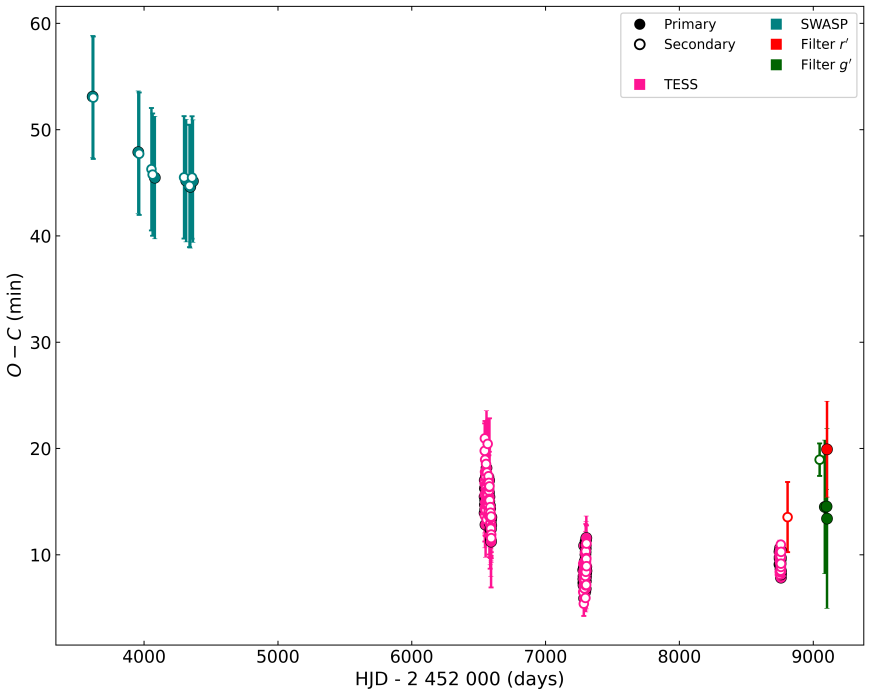

Figure 5.21: $O-C$ diagram for pair A of the system S4 Vel. To improve the visualisation of the long-term trend, the calculated times of minima (C) were derived using a modified reference period of $P_{\mathrm{ref}} = 0.544979$ days, while the reference epoch T_0 was retained from Table 5.2.

5.5 SED Analysis

The data for the construction of the SED graphs were obtained using the VOSA web service (Bayo et al., 2008). This process required input parameters for the distance and extinction of the analysed systems. While VOSA offers an option to search for these parameters, it may not always be successful. Therefore, the distance parameter for S1 CMi was adopted from *Gaia* DR3 (Gaia Collaboration, 2023), and its extinction was taken from the 3D Dust Mapping service (Green et al., 2019; Argonaut Sky Maps, 2025). For S4 Vel, because the extinction was unavailable via the 3D Dust Mapping page, it was adopted from the Online Data Catalog (Anders et al., 2022), while its distance was obtained through VOSA, which retrieved the value from *Gaia* DR3. The distances for both systems were cross-checked with the distances provided by Bailer-Jones et al. (2021) and found to be highly consistent. The final adopted parameters are listed in Table 5.4 below.

Table 5.4: Summary of parameters required for the SED analysis.

Parameter	System S1 CMi	System S4 Vel
Distance from *Gaia* DR3 (pc)	700^{+10}_{-10}	370^{+20}_{-20}
Distance from Bailer-Jones et al. (2021) (pc)	720^{+20}_{-20}	365^{+35}_{-20}
Extinction in V (mag)	$0.11^{+0.08}_{-0.08}$	$0.221^{+0.005}_{-0.221}$

The next step involved using the Virtual Observatory (VO) photometry tool to gather all available photometric data. To fit the resulting SEDs, the Kurucz ODFNEW/NOVER model grid with an alpha enhancement of 0.0 (Castelli & Kurucz, 2003) was selected for both systems. These models provide a much more realistic representation of the stellar atmosphere than simple blackbody approximations. This specific grid is highly reliable for standard main-sequence stars and provides extensive coverage across the expected effective temperatures and surface gravities of the analysed components. Furthermore, a solar alpha-element abundance parameter (alpha: 0.0) was adopted, representing the standard and most appropriate assumption for typical stellar populations situated within the Galactic disk. While the SED fitting tool automatically ranks results by minimising the χ^2 value, this purely statistical approach can sometimes yield unphysical stellar parameters. Consequently, the final SED models presented in this work were selected not solely on the absolute minimum χ^2, but by verifying that the fitted parameters are physically consistent with the known characteristics of the system.

The produced SED graphs (Figures 5.22 and 5.23) provide estimates for the effective temperatures, surface gravities, and metallicities of the systems. However, it must be noted that SED fitting is primarily sensitive to the effective temperature ($T_{\rm eff}$). Because the photometric determination of surface gravity and metallicity is largely degenerate and highly uncertain, the primary objective of this fitting process was to robustly determine

the effective temperatures. Tables 5.5 and 5.6 summarise the obtained data and show a comparison with the available parameters from *Gaia* DR3 (Gaia Collaboration, 2023) for S1 CMi and *Gaia* DR2 (Gaia Collaboration, 2018) for S4 Vel.

Table 5.5: SED-derived parameters compared with *Gaia* DR3 parameters for the system S1 CMi.

S1 CMi	$T_{\rm eff}$ (K)	log g	Metallicity
SED	8500^{+125}_{-125}	$4.50^{+0.25}_{-0.25}$	$-2.00^{+0.25}_{-0.25}$
Gaia	9850^{+40}_{-30}	$4.09^{+0.06}_{-0.02}$	$-0.100^{+0.001}_{-0.001}$

Table 5.6: SED-derived parameters compared with *Gaia* DR2 parameters for the system S4 Vel. The values for log g and metallicity were not available.

S4 Vel	$T_{\rm eff}$ (K)	log g	Metallicity
SED	7000^{+125}_{-125}	$3.50^{+0.25}_{-0.25}$	$0.00^{+0.10}_{-0.25}$
Gaia	6760^{+190}_{-280}	-	-

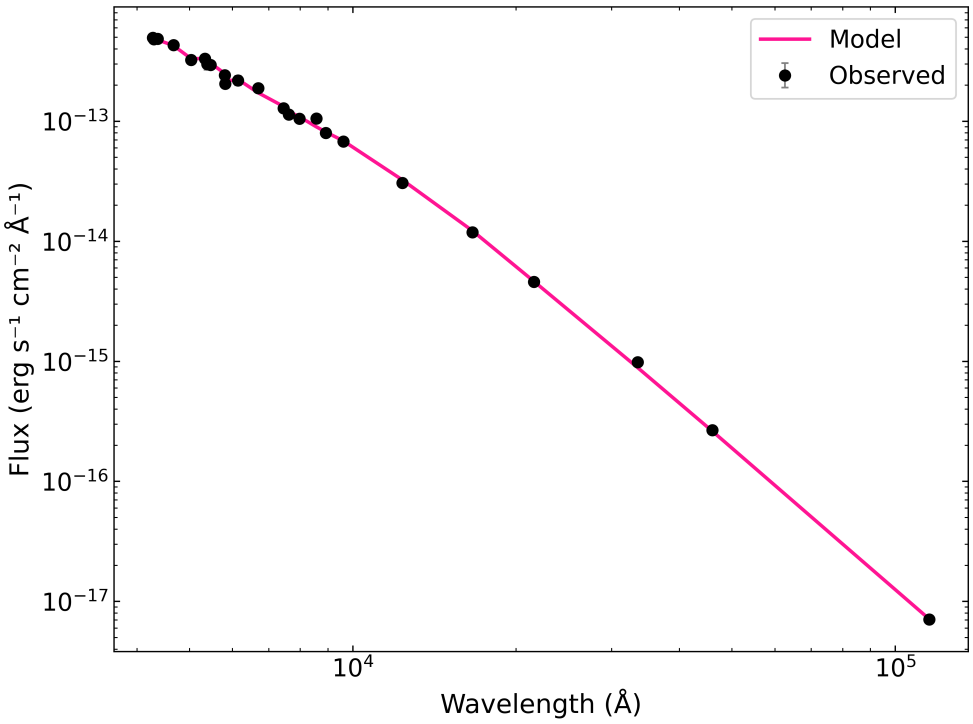

Figure 5.22: Observed SED of S1 CMi (black circles) overlaid with the best-fit theoretical model (pink line).

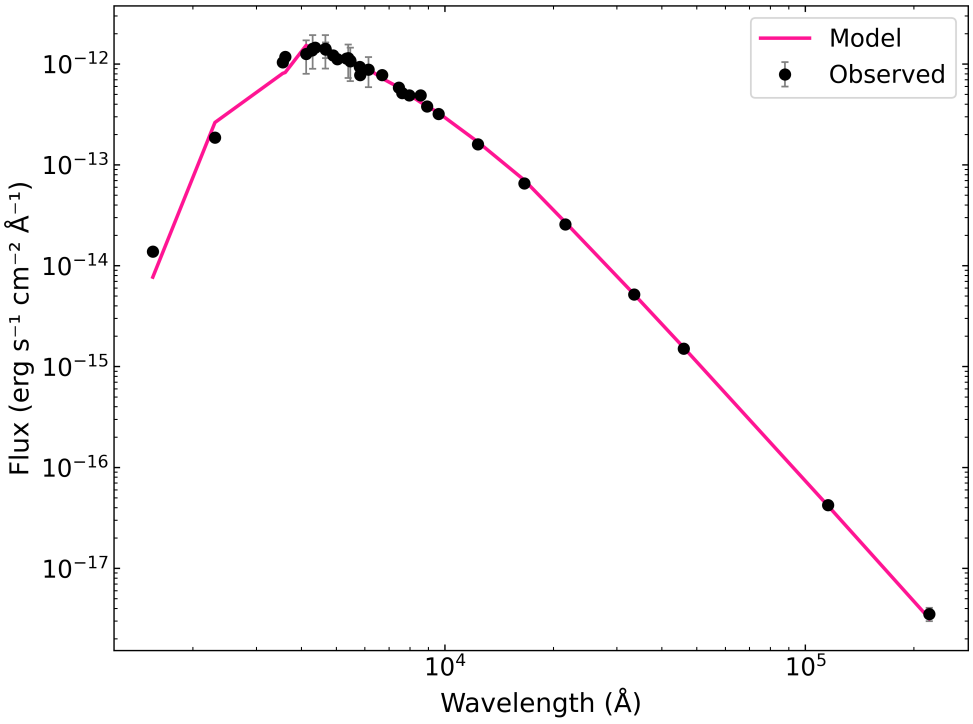

Figure 5.23: Observed SED of S4 Vel (black circles) overlaid with the best-fit theoretical model (pink line).

5.6 Light Curve and Radial Velocity Modelling

5.6.1 Models for S1 CMi

In the measured spectra, only the primary components of both stars were visible. The clear identification of Fe II lines in the spectra for both primaries indicates that they share a similar effective temperature, placing them in the early-to-mid A spectral range (A0–A5) (Gray, 2021). While temperature calibration tables for subgiants (luminosity class IV) are less standardised than those for main-sequence stars, A0–A5 objects typically exhibit temperatures between 8300 K and 9500 K (Gray, 2021). It was assumed that the subgiant components in this system fall within a similar temperature range.

This deduction is consistent with the system's overall spectral classification of A2 IV. However, existing catalogues present a discrepancy: while *Gaia* DR3 suggests a combined system temperature of approximately 9800 K, an independent SED analysis yields a cooler temperature of 8500 K. Based on these combined factors, the effective temperatures of the primary stars were fixed at 9100 K for pair A and 9000 K for pair B.

Because both pairs are single-lined spectroscopic binaries, a direct, independent derivation of the absolute masses is impossible. To break this degeneracy, the mass of the primary component was fixed to 2.1 $M_\odot$ for pair A and 2.0 $M_\odot$ for pair B, derived from

the A2 IV spectral classification and effective temperatures. By adopting these primary masses and the photometrically derived inclinations, the radial velocity amplitudes of the primary stars yielded the mass ratios (q) and the absolute parameters of the secondary components.

In close binary systems, stars are gravitationally distorted rather than perfectly spherical. Consequently, PHOEBE utilises the Equivalent Radius ($R_{\rm equiv}$), defined as the radius of a perfect, undeformed sphere with the same total volume as the modelled star. The photometric light curve dictates the fractional sizes of the stars relative to the semi-major axis ($r = R/a$). To determine the absolute physical radii, a scale must be established using the radial velocity data. By adopting a fixed primary mass (M_1) and fitting the radial velocity curve to obtain the velocity semi-amplitude of the primary (K_1), the projected semi-major axis of the primary component is calculated using the relation (Hilditch, 2001):

$$a_1 \sin i = \frac{K_1 P \sqrt{1 - e^2}}{2\pi}\,, \tag{5.1}$$

where P is the orbital period, e is the eccentricity, i is the orbital inclination, and a_1 is the absolute semi-major axis of the primary star's orbit. Using the binary mass function (see Equation 3.5), the secondary mass (M_2) is determined. With both M_1 and M_2 known, Kepler's Third Law is applied to calculate the total semi-major axis ($a = a_1 + a_2$). Finally, the fractional radii derived from the light curve are scaled by this absolute semi-major axis to produce the absolute equivalent radii in solar units.

Pair A and pair B are observed as a single blended point of light; thus, when modelling one binary, the light contribution from the other pair, along with any potential unresolved background sources, must be accounted for as third light (l_3). Theoretically, assuming the system is isolated, these fractional third light values should be perfectly complementary, meaning the sum of l_3 from both pairs should equal 1.0 (100 per cent).

However, strictly enforcing this sum during the fitting process prevented the models from accurately reproducing the observed eclipse depths without pushing the stellar geometries beyond physical limits (e.g., Roche lobe overflow). To prioritise a physically accurate representation of the stellar shapes and eclipse depths, the third light parameters were treated independently for each binary. Rather than forcing a fixed total sum, each model was allowed to determine its own optimal l_3 value to best match the light curve. Therefore, rather than deriving absolute percentage luminosities, the ratio of the fitted third light parameters ($l_{3,\rm B}/l_{3,\rm A}$) is reported to represent the relative scaling of the two systems. This ratio yields a value of $2.34^{+0.73}_{-0.59}$, confirming that pair A is approximately 2.3 times brighter than pair B and providing a more reliable characterisation of the blended light contribution.

The final system parameters and their associated uncertainties were determined through a Markov Chain Monte Carlo (MCMC) optimisation using the emcee solver

within the PHOEBE framework. To ensure computational stability and resolve potential degeneracies, the optimisation was conducted in two sequential stages:

- Photometric Analysis: The initial stage focused on the light curve to constrain the geometric and radiative properties, including the equivalent radii (R_1, R_2), inclination (i), and the secondary effective temperature ($T_{\rm eff,2}$). As mentioned above, the primary temperature ($T_{\rm eff,1}$) was held constant.

- Spectroscopic Analysis: Following the adoption of the best-fit geometric solution, a separate MCMC analysis was performed on the radial velocity data to determine the dynamical parameters, specifically the mass ratio (q) and the systemic velocity (v_γ). To illustrate the nature of the MCMC solutions, the resulting corner plot for the dynamical parameters of pair B of of S1 CMi's pair B is presented in the Appendices (Figure A.1).

This sequential approach resulted in a physically consistent global model. The final derived parameters for pair A and pair B are presented in Tables 5.7 and 5.8, respectively. Note that the uncertainties listed for $T_{\rm eff,2}$ in these tables, derived from the MCMC, are likely underestimated. While typical temperature uncertainties are ∼100–200 K, the MCMC only calculates formal statistical errors based on the mathematical fit to the data. The corresponding best-fit models for the *TESS* light curves and radial velocity curves are illustrated in Figures 5.24, 5.27, and Figures 5.25, 5.28. Additionally, surface mesh representations of the modelled components for both pairs are shown in Figures 5.26 and 5.29.

Table 5.7: Final derived parameters for S1 CMi, pair A.

Parameter	Symbol	Value	Unit
Inclination	i	$89.0^{+0.6}_{-0.5}$	$^\circ$
Primary Eff. Temperature	$T_{\rm eff,1}$	9100 (fixed)	K
Secondary Eff. Temperature	$T_{\rm eff,2}{}^*$	5630^{+30}_{-30}	K
Primary Equiv. Radius	R_1	$1.96^{+0.03}_{-0.05}$	$R_\odot$
Secondary Equiv. Radius	R_2	$1.11^{+0.05}_{-0.03}$	$R_\odot$
Mass Ratio	q	$0.442^{+0.002}_{-0.003}$	—
Primary Mass	M_1	2.1 (fixed)	$M_\odot$
Secondary Mass	M_2	$0.928^{+0.005}_{-0.006}$	$M_\odot$
Systemic Velocity	v_γ	$33.0^{+0.4}_{-0.7}$	km s^{-1}

* Note: MCMC uncertainties are strictly formal and likely underestimated; see text in Subsection 5.6.1 for details.

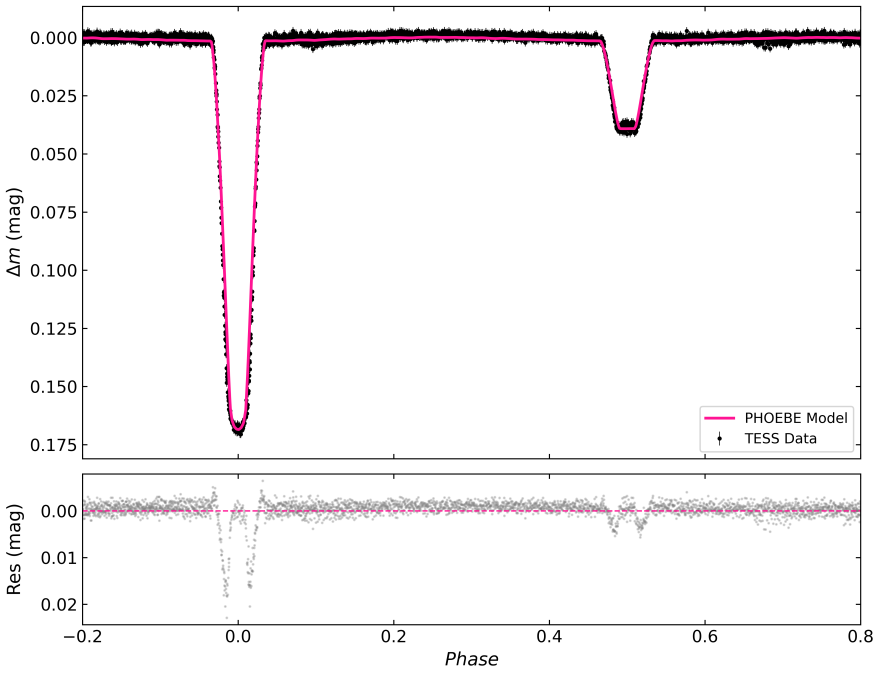

Figure 5.24: Light curve solution for S1 CMi, pair A. Phase-folded *TESS* observations from Sector 33 (black dots) are plotted alongside the derived physical model (solid pink line). Residuals between the observational data and the model are shown in the lower panel. The observations were phase-folded using the orbital period $P = 3.526315$ days and a reference epoch of $T_0 = 2458507.84176$ HJD, both derived from the MCMC analysis.

As seen in the lower panel of Figure 5.24, the model fits well to the out-of-eclipse phases. However, systematic residuals reaching an amplitude of approximately 0.02 mag remain during both the primary and secondary eclipses. These could reflect minor uncertainties in limb darkening or gravity brightening coefficients, or be effects from the light curve disentangling process. Regardless, their small amplitude relative to the overall eclipse depth suggests they do not significantly impact the reliability of the derived physical parameters.

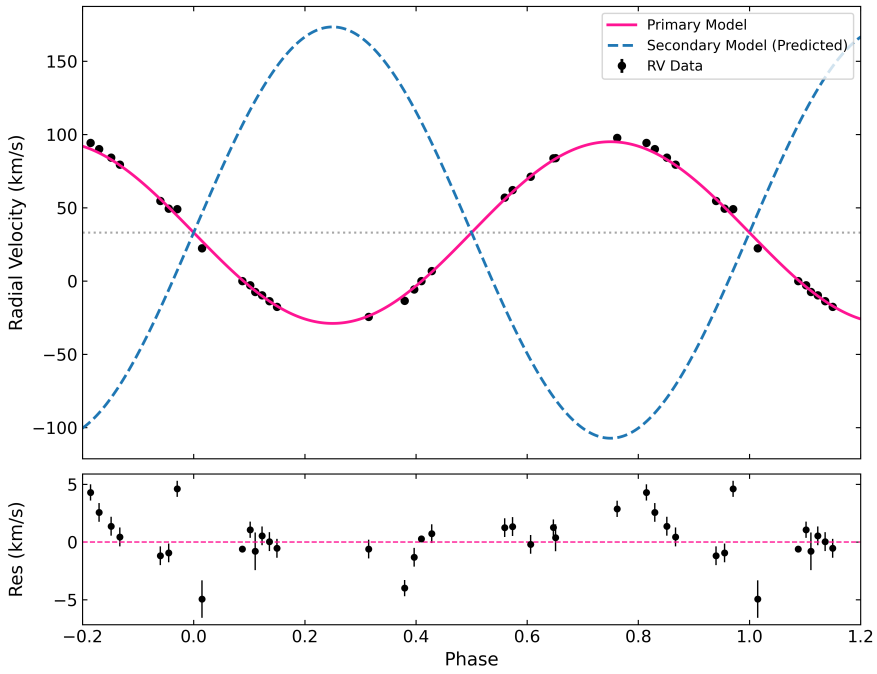

Figure 5.25: Radial velocity solution for S1 CMi, pair A. Primary observations (black circles) are plotted alongside the derived primary model (solid pink line) and the dynamically predicted secondary model (dashed blue line). The horizontal line marks the system's centre-of-mass velocity. Residuals between the primary data and the model are shown in the lower panel. The data and models are plotted over 1.4 orbital cycles (phases -0.2 to 1.2) for visual continuity. The observations were phase-folded using the orbital period $P = 3.526315$ days and a reference epoch of $T_0 = 2458507.84176$ HJD, both derived from the MCMC analysis.

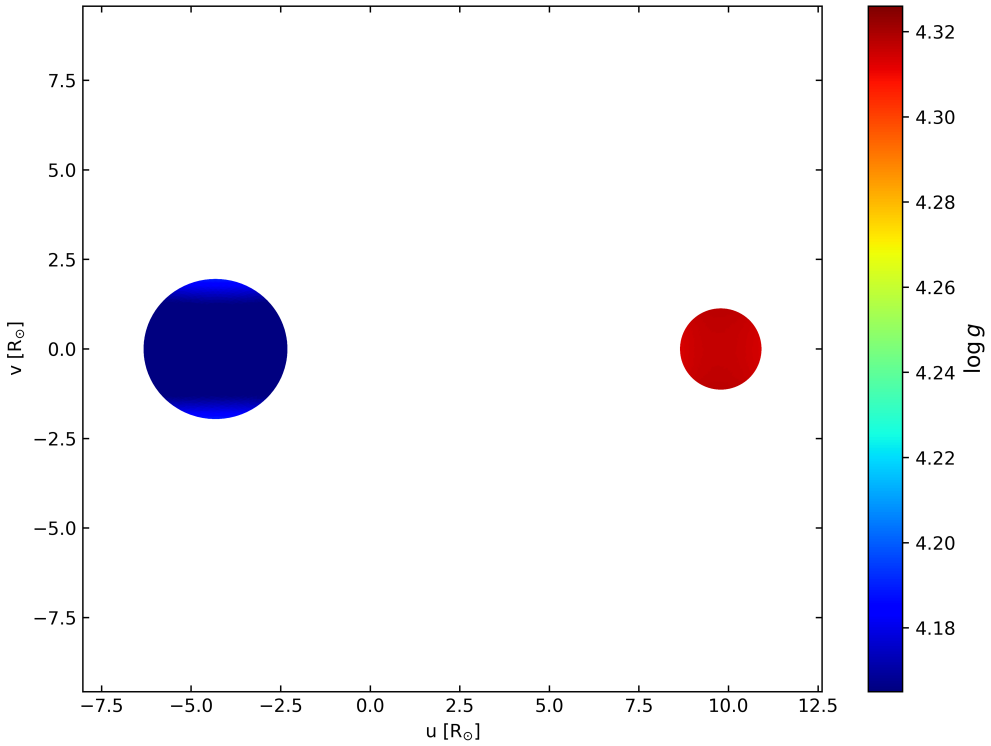

Figure 5.26: Mesh representation of pair A of the system S1 CMi at orbital phase 0.25, mapped using local surface gravity ($\log g$). The $\log g$ scale was chosen over effective temperature ($T_{\rm eff}$) because the $\sim$3500 K difference between the components would dominate the colour scale and obscure localised variations. The u and v axes represent the spatial coordinates of the system projected onto the plane of the sky, expressed in units of solar radii ($\mathrm{R}_\odot$).

Table 5.8: Final derived parameters for S1 CMi, pair B.

Parameter	Symbol	Value	Unit
Inclination	i	$89.3^{+0.5}_{-0.8}$	$^\circ$
Primary Eff. Temperature	$T_{\rm eff,1}$	9000 (fixed)	K
Secondary Eff. Temperature	$T_{\rm eff,2}$ *	5430^{+50}_{-50}	K
Primary Equiv. Radius	R_1	$1.68^{+0.06}_{-0.08}$	$R_\odot$
Secondary Equiv. Radius	R_2	$0.93^{+0.09}_{-0.09}$	$R_\odot$
Mass Ratio	q	$0.506^{+0.007}_{-0.007}$	—
Eccentricity	e	$0.21^{+0.02}_{-0.02}$	—
Argument of Periastron	ω	130^{+6}_{-4}	$^\circ$
Primary Mass	M_1	2.0 (fixed)	$M_\odot$
Secondary Mass	M_2	$1.01^{+0.01}_{-0.01}$	$M_\odot$
Systemic Velocity	v_γ	$19.5^{+0.5}_{-0.5}$	km s^{-1}

* Note: MCMC uncertainties are strictly formal and likely underestimated; see text in Subsection 5.6.1 for details.

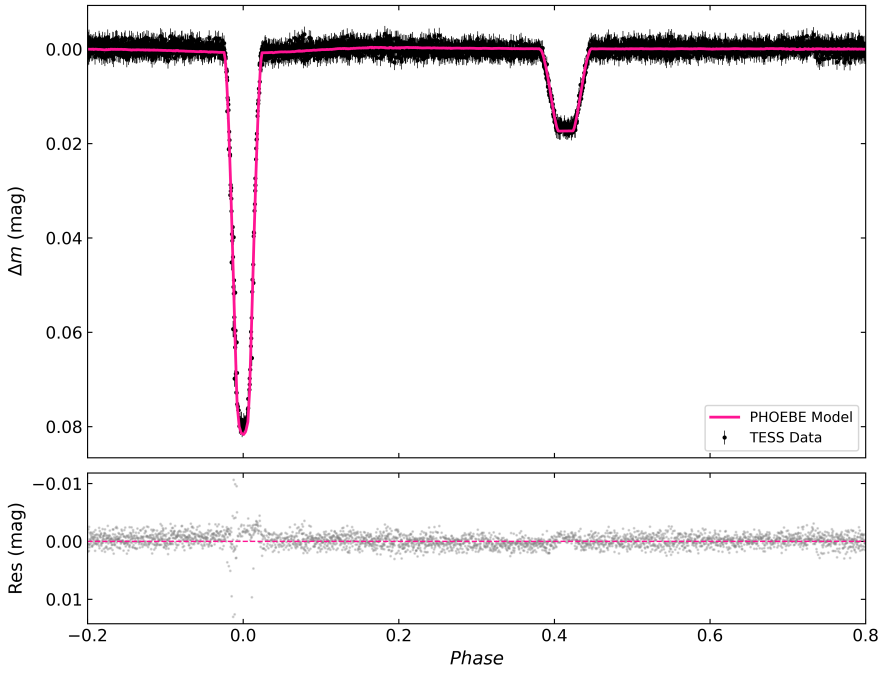

Figure 5.27: Light curve solution for S1 CMi, pair B. Phase-folded *TESS* observations from Sector 33 (black dots) are plotted alongside the derived physical model (solid pink line). Residuals between the observational data and the model are shown in the lower panel. The observations were phase-folded using the orbital period $P = 3.733424$ days and a reference epoch of $T_0 = 2463748.80442$ HJD, both derived from the MCMC analysis.

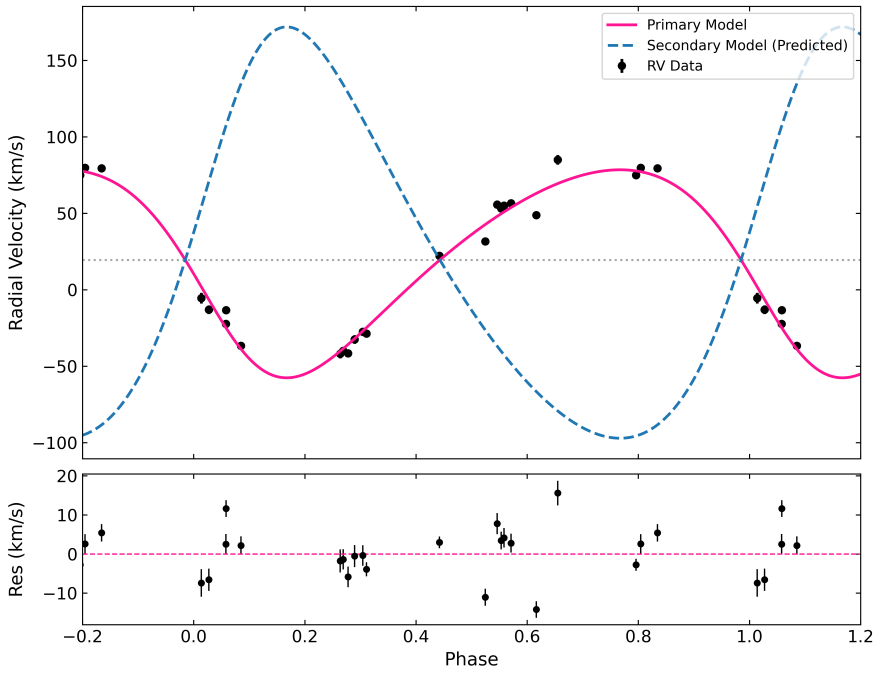

Figure 5.28: Radial velocity solution for S1 CMi, pair B. Primary observations (black circles) are plotted alongside the derived primary model (solid pink line) and the dynamically predicted secondary model (dashed blue line). The horizontal line marks the system's centre-of-mass velocity. Residuals between the primary data and the model are shown in the lower panel. The data and models are plotted over 1.4 orbital cycles (phases -0.2 to 1.2) for visual continuity. The observations were phase-folded using the orbital period $P = 3.733424$ days and a reference epoch of $T_0 = 2463748.80442$ HJD, both derived from the MCMC analysis.

An analysis of the radial velocity solutions for S1 CMi highlights the link between the spectroscopic data and the photometric $O-C$ analysis. The models derived distinct systemic velocities (v_γ) for the two binaries: 33.0 km s^{-1} for pair A and 19.5 km s^{-1} for pair B. While the positive values of both velocities indicate that the quadruple system is moving away from Earth at a calculated mean velocity of approximately 26.3 km s^{-1}, it must be noted that this absolute value remains highly uncertain due to the short observational baseline of the spectroscopic data relative to the very long, at least 80-year outer orbit.

However, the distinct velocities of the individual pairs mirror the trends observed in the $O-C$ diagrams. The currently rising $O-C$ trend for pair A indicates it is physically moving away from the observer, which is reflected in its higher relative velocity. Conversely, the falling $O-C$ trend for pair B indicates it is moving towards the observer, corresponding to its lower relative velocity. The resulting $\sim$13.5 km s^{-1} difference between them represents the speed of their mutual orbital motion. This radial

velocity analysis provides compelling supporting evidence that the two binaries are gravitationally bound in a mutual outer orbit.

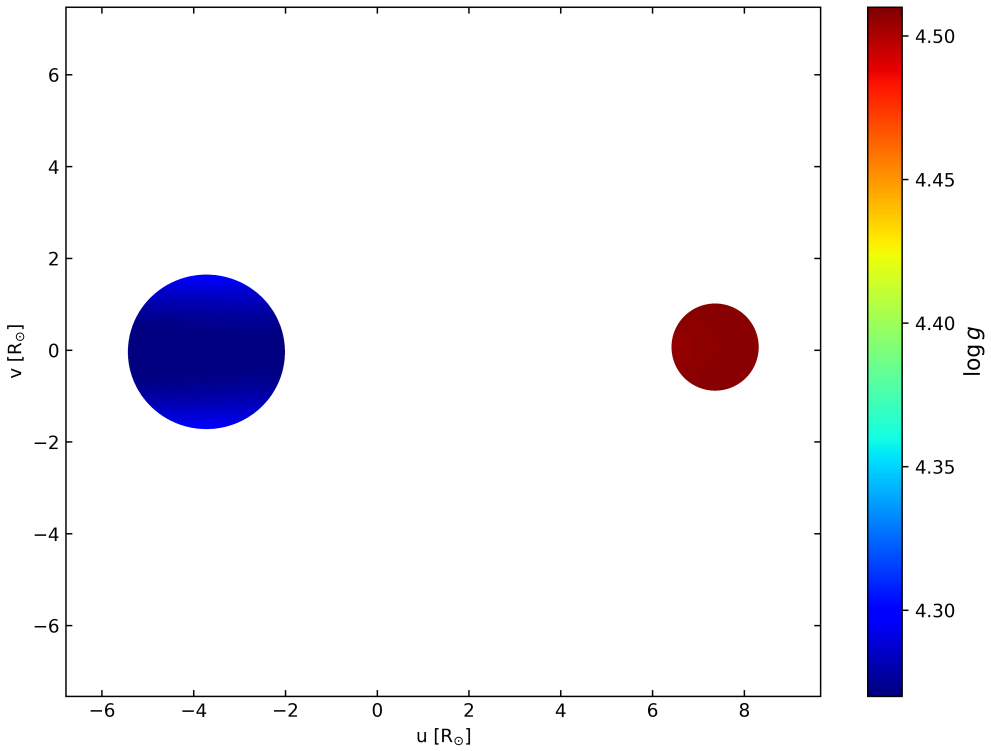

Figure 5.29: Mesh representation of pair B of the system S1 CMi at orbital phase 0.25, mapped using local surface gravity ($\log g$). The $\log g$ scale was chosen over effective temperature ($T_{\rm eff}$) because the ∼3500 K difference between the components would dominate the colour scale and obscure localised variations. The u and v axes represent the spatial coordinates of the system projected onto the plane of the sky, expressed in units of solar radii ($R_\odot$).

5.6.2 Models for S4 Vel

Despite the availability of numerous spectroscopic observations, it was not possible to extract reliable radial velocity data for this system. While all four components are likely present in the spectra, rapid rotation and blending cause the split lines to merge into broad, unresolved profiles. Furthermore, the fact that no single component dominates the spectrum suggests that the system is composed of stars with very similar effective temperatures.

The S4 Vel system is classified as a spectral type F2 V. According to Gray (2021), the typical effective temperature for stars of this spectral type is approximately 6900 K, corresponding to a mass of roughly 1.6 $M_\odot$. A spectral energy distribution (SED) analysis derived a temperature of 7000 K, while *Gaia* DR2 determined it to be 6760 K. Other catalogues provide similar estimates: Anders et al. (2022) states 7050 K, whereas the Paegert et al. (2022) and Kostov et al. (2022b) report 6990 K. Although these

literature values vary slightly, they consistently fall within the range of 6760 K to 7050 K. Based on this consensus, an effective temperature of 6990 K was adopted for the primary star of pair A. The primary component of pair B was deduced to be similar to, or slightly cooler than, the primary of pair A. Therefore, its temperature was set to 6800 K, with an assumed mass of 1.5 $M_\odot$. While absolute masses cannot be precisely constrained without radial velocity data, the PHOEBE software still requires these parameters to scale the physical Keplerian model. Consequently, it was necessary to provide physically realistic baseline values that align with the established spectral types. Because absolute dimensions cannot be calculated without radial velocities, the absolute equivalent radii of the stars could not be determined. For this reason, the geometry of the system is expressed using fractional radii (R_1/a and R_2/a), which represent the relative sizes of the stars scaled to their semi-major axis. Finally, while a baseline mass ratio q could be estimated via the Nelder-Mead algorithm by leveraging the out-of-eclipse ellipsoidal variations, this parameter remains highly degenerate when fitting photometric light curves alone. To prevent unphysical skewing of the estimated uncertainties, q was kept fixed at this derived value and excluded from the MCMC analysis. Following the approach used for S1 CMi, the relative luminosity of the two binaries is evaluated using their third light parameters. The ratio of the fitted third lights ($l_{3,\mathrm{B}}/l_{3,\mathrm{A}}$) is $3.63^{+0.07}_{-0.08}$. Since the third light in the model of pair B ($l_{3,\mathrm{B}}$) corresponds to the luminosity of pair A, this ratio confirms that pair A is approximately 3.6 times brighter than pair B.

The derived parameters for pair A and pair B can be found in Tables 5.9 and 5.10, and the final models in Figures 5.30 and 5.32, respectively. The corresponding surface mesh plots for both pairs are presented in Figures 5.31 and 5.33.

Table 5.9: Final derived parameters for S4 Vel, pair A.

Parameter	Symbol	Value	Unit
Inclination	i	$89.5^{+0.4}_{-0.4}$	$^\circ$
Primary Eff. Temperature	$T_{\mathrm{eff},1}$	6990 (fixed)	K
Secondary Eff. Temperature	$T_{\mathrm{eff},2}$ *	6955^{+20}_{-20}	K
Primary Frac. Radius	R_1/a	$0.180^{+0.002}_{-0.003}$	—
Secondary Frac. Radius	R_2/a	$0.177^{+0.003}_{-0.003}$	—
Mass Ratio	q	0.8854 (fixed)	—
Primary Mass	M_1	1.60 (fixed)	$M_\odot$
Secondary Mass	M_2	1.42 (fixed)	$M_\odot$

* Note: MCMC uncertainties are strictly formal and likely underestimated; see text in Subsection 5.6.1 for details.

The primary mass was anchored to 1.6 $M_\odot$ and the mass ratio was fixed to 0.8854, inherently constraining the secondary mass to 1.42 $M_\odot$. Because this secondary mass

is calculated directly from these assumed values rather than being a free parameter in the MCMC model, it is designated as fixed in Table 5.9. It must also be noted that the tabular mass value for a main-sequence star with an effective temperature of 6955 K is approximately 1.58 $M_{\odot}$ (Gray, 2021). This discrepancy clearly demonstrates that without radial velocity data, the photometrically derived mass ratio (q) is physically unconstrained and unreliable.

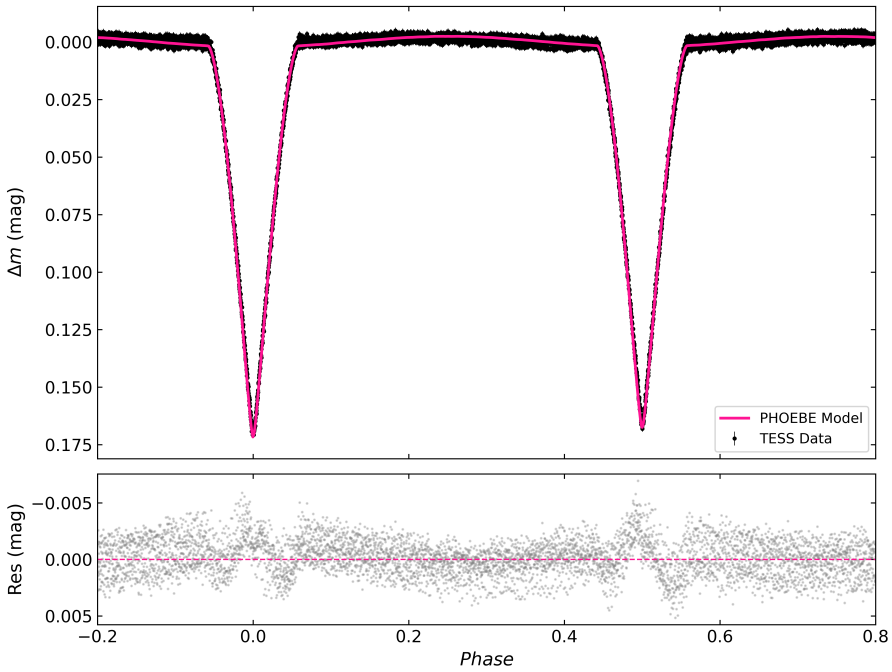

Figure 5.30: Light curve solution for S4 Vel, pair A. Phase-folded *TESS* observations from Sector 90 (first half) (black dots) are plotted alongside the derived physical model (solid pink line). Residuals between the observational data and the model are shown in the lower panel. The observations were phase-folded using the orbital period listed in Table 5.2 and a reference epoch of $T_0 = 2459288.82363$ HJD derived from the MCMC analysis.

The light curve solution for pair A, shown in Figure 5.30, demonstrates good agreement with the data, with residuals limited to ≈ 0.005 mag. Despite this low amplitude, "W-shaped" patterns, comparable to those previously described for pair A of the system S1 CMi, are visible during the eclipse phases. As mentioned above, in the absence of radial velocity data, the mass ratio could not be constrained, which limits the precision of the model outside of eclipses. The residuals likely reflect the degeneracies between the mass ratio, limb darkening, and the geometric parameters of the stars when fitting photometry alone. While similarly structured eclipse residuals have been observed in the *TESS* light curves of another doubly eclipsing binary (BG Ind; Borkovits

et al. (2021)), those specific variations were associated with the cooler components of the system (around 4500 K) and attributed to chromospheric/photospheric activity. In contrast, the components of S4 Vel pair A possess effective temperatures of ∼6900 K, placing them in the radiative envelope regime where traditional magnetic starspots do not typically form. Therefore, these "W-shaped" residuals are most likely the product of the aforementioned degeneracies, or potentially unmodelled surface inhomogeneities. Nonetheless, the small amplitude of these residuals relative to the eclipse depth indicates that the model remains a reliable representation of the pair's characteristics.

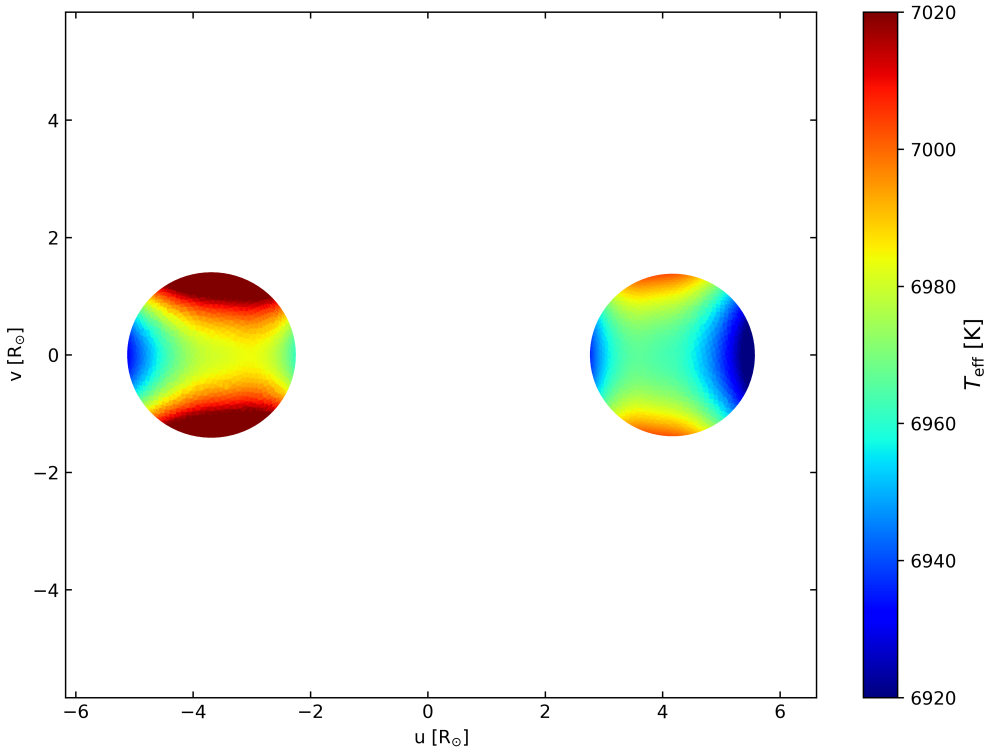

Figure 5.31: Mesh representation of pair A of the system S4 Vel at orbital phase 0.25, mapped using local effective temperature ($T_{\rm eff}$). In the absence of radial velocity data to determine absolute masses and radii, mapping by $T_{\rm eff}$ provides the most physically meaningful visualisation of the surfaces. Because the overall temperature difference between the components is small, the colour scale clearly displays surface details, such as gravity darkening and the reflection effect. The u and v axes represent the spatial coordinates of the system projected onto the plane of the sky, expressed in units of solar radii ($R_\odot$).

Table 5.10: Final derived parameters for S4 Vel, pair B.

Parameter	Symbol	Value	Unit
Inclination	i	$85.8^{+1.00}_{-1.0}$	$^\circ$
Primary Eff. Temperature	$T_{\mathrm{eff},1}$	6800 (fixed)	K
Secondary Eff. Temperature	$T_{\mathrm{eff},2}$ *	6380^{+30}_{-40}	K
Primary Frac. Radius	R_1/a	$0.331^{+0.001}_{-0.002}$	—
Secondary Frac. Radius	R_2/a	$0.253^{+0.002}_{-0.001}$	—
Mass Ratio	q	0.6556 (fixed)	—
Primary Mass	M_1	1.50 (fixed)	$M_\odot$
Secondary Mass	M_2	0.98 (fixed)	$M_\odot$

* Note: MCMC uncertainties are strictly formal and likely underestimated; see text in Subsection 5.6.1 for details.

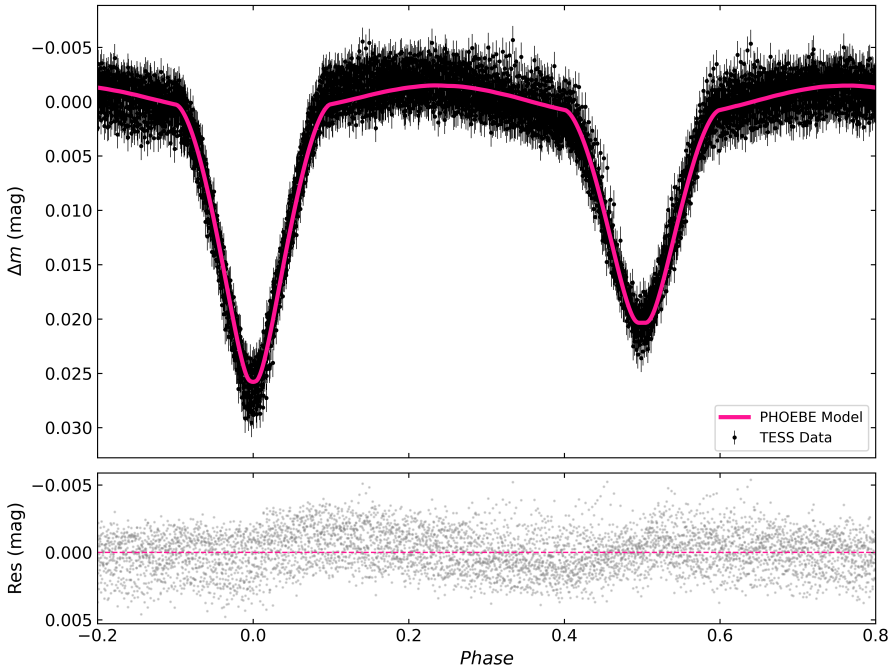

Figure 5.32: Light curve solution for S4 Vel, pair B. Phase-folded *TESS* observations from Sector 90 (first half) (black dots) are plotted alongside the derived physical model (solid pink line). Residuals between the observational data and the model are shown in the lower panel. The observations were phase-folded using the orbital period listed in Table 5.2 and a reference epoch of $T_0 = 2459288.55492$ HJD derived from the MCMC analysis.

The residuals for pair B, shown in the lower panel of Figure 5.32, exhibit a wave-like pattern throughout the out-of-eclipse phases. This arises because the phase curve

itself displays an asymmetry in these regions, which is difficult to fit with a standard model. A closer inspection reveals that this specific portion of the phase curve varies across different *TESS* sectors (see Figure A.2 in the Appendices). This time-dependent variation suggests the asymmetry is driven by intrinsic stellar activity, such as evolving starspots. Furthermore, as with pair A, the absence of radial velocity data means the mass ratio could not be independently constrained, adding a secondary complication to the out-of-eclipse fit. Despite these structured residuals, the overall geometric solution remains reliable.

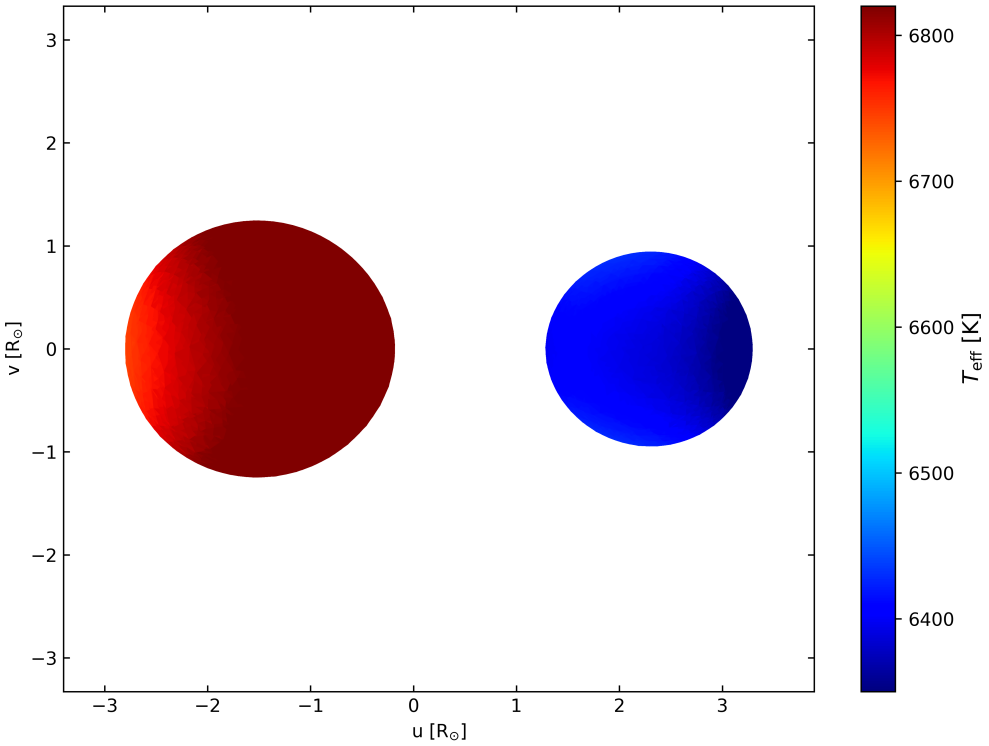

Figure 5.33: Mesh representation of pair B of the system S4 Vel at orbital phase 0.25, mapped using local effective temperature ($T_{\rm eff}$). In the absence of radial velocity data to determine absolute masses and radii, $T_{\rm eff}$ provides the most physically meaningful visualisation of the surfaces. While the ∼400 K temperature difference between the components requires a broader colour scale that obscures fine-scale temperature variations, the ellipsoidal distortion of the stars due to tidal forces remains clearly visible. The u and v axes represent the spatial coordinates of the system projected onto the plane of the sky, expressed in units of solar radii ($R_\odot$).

Conclusion

This study presented a comprehensive analysis of two doubly eclipsing candidates, S1 CMi (TYC 168-784-1) and S4 Vel (V0432 Vel). By combining high-precision space-based *TESS* photometry, ground-based observations, archival data, and high-resolution spectroscopy, this work successfully derived the fundamental geometric and physical parameters of these systems. Crucially, the analysis of their $O-C$ diagrams revealed anti-correlated Light-Time Effects (LiTE) for both targets, confirming their status as gravitationally bound quadruple star systems.

Reliable results were obtained for the system S1 CMi due to the successful extraction of radial velocities for the primary components from PLATOSpec and HERMES spectra. The dynamical constraints provided by these radial velocity curves, combined with the PHOEBE 2 photometric models, allowed for the determination of absolute masses and equivalent radii, revealing that each binary pair consists of a hot primary star and a significantly cooler, less massive companion. Furthermore, while the partial coverage of the LiTE curve constrained the mutual outer orbital period to a minimum of 80 years, the long-term $O-C$ analysis of pair B in this system revealed an additional, systematic separation between its primary and secondary minima, identified as apsidal motion within an eccentric orbit. To accurately isolate the effect, the LiTE was first subtracted, allowing the apsidal motion to be modelled with a preliminary estimated minimum period of approximately 430 years. Additionally, the measured relative velocity difference of $\sim$13.5 km s^{-1} between the two binaries is in accordance with the approaching and receding trends visible in the $O-C$ diagrams, strengthening the evidence for the gravitational bond of the quadruple system.

The analysis of S4 Vel presented some challenges, primarily because the blending of its four components prevented the extraction of usable radial velocity data. Consequently, the physical models for both pairs in S4 Vel relied on photometric constraints and theoretical mass assumptions, guided by the system's overall F2 V spectral classification and independent SED analysis. This analysis revealed that the system is composed of four stars with very similar effective temperatures, with pair B consisting of close, slightly ellipsoidal components. While the absolute masses of S4 Vel remain unconstrained without radial velocity data, the photometric modelling successfully derived the system's fractional radii and orbital inclinations. Furthermore, the visible antiphase LiTE

curvature in the $O-C$ diagrams, which constrains the mutual outer orbit to a minimum period of 90 years, serves as definitive proof that S4 Vel is a gravitationally bound quadruple system.

A consistent feature across the photometric modelling of both systems was the presence of small, structured residuals in the *TESS* light curve solutions. This included "W-shaped" patterns during the primary eclipses of pair A in both systems, and wave-like, out-of-eclipse variations in pair B of S4 Vel. As demonstrated by sector-by-sector comparisons specifically for pair B, these out-of-eclipse asymmetries are clearly time-dependent, indicating intrinsic stellar variability. Across both systems, these variations likely originate from different physical mechanisms depending on the specific component's temperature, such as starspots on the cooler convective secondaries, or alternative surface inhomogeneities on the hotter radiative primaries. Rather than attempting to fit complex variation models to single-band photometry, these asymmetries were left as residuals. This approach is fully consistent with treatments of similar multiple-star systems in the literature, where such variations are attributed to generic photospheric activity and left as residuals or mathematically filtered.

Future research must address several important areas. First and foremost, continued minima timing observations over the coming decades are essential because the current $O-C$ baselines cover only a fraction of the mutual orbits; long-term monitoring is required to fully close the LiTE curves and precisely constrain the outer orbital periods. Furthermore, obtaining radial velocities for the secondary components of S1 CMi, as well as for every star of S4 Vel, remains a critical objective. Future efforts utilising higher signal-to-noise observations will be necessary to resolve the individual components and enable the extraction of radial velocity data. Finally, the significant computational time required to model these systems remains a limiting factor. Securing dedicated computing resources will allow for the higher-iteration optimisation needed to achieve even greater precision in future physical models.

In conclusion, this research confirms that both S1 CMi and S4 Vel are gravitationally bound doubly eclipsing systems, expanding the sample of confirmed 2+2 quadruples. By combining precise space photometry with ground-based and spectroscopic observations, this work derives the fundamental physical and orbital parameters for these targets, offering a detailed characterisation of these complex stellar architectures.

Bibliography

F. Anders, A. Khalatyan, A. B. A. Queiroz, C. Chiappini, J. Ardevol, L. Casamiquela, F. Figueras, O. Jimenez-Arranz, C. Jordi, M. Monguio, M. Romero-Gomez, D. Altamirano, T. Antoja, R. Assaad, T. Cantat-Gaudin, A. Castro-Ginard, H. Enke, L. Girardi, G. Guiglion, S. Khan, X. Luri, A. Miglio, I. Minchev, P. Ramos, B. X. Santiago, & M. Steinmetz. VizieR Online Data Catalog: StarHorse2, Gaia EDR3 photo-astrometric distances (Anders+, 2022), Jan. 2022.

Argonaut Sky Maps. Argonaut sky maps. http://argonaut.skymaps.info/, 2025. Accessed: 2025-11-16.

C. A. L. Bailer-Jones, J. Rybizki, M. Fouesneau, M. Demleitner, & R. Andrae. VizieR Online Data Catalog: Distances to 1.47 billion stars in Gaia EDR3 (Bailer-Jones+, 2021). VizieR On-line Data Catalog: I/352. Originally published in: 2021AJ....161..147B, Feb. 2021.

A. Batten & T. Haar. *Binary and Multiple Systems of Stars*. Pergamon, 2013. International Series of Monographs in Natural Philosophy.

A. Bayo, C. Rodrigo, D. Barrado Y Navascués, E. Solano, R. Gutiérrez, M. Morales-Calderón, & F. Allard. VOSA: virtual observatory SED analyzer. An application to the Collinder 69 open cluster. *Astronomy & Astrophysics*, 492(1):277–287, Dec. 2008. doi: 10.1051/0004-6361:200810395.

G. Beskin, S. Karpov, A. Biryukov, S. Bondar, E. Ivanov, E. Katkova, N. Orekhova, A. Perkov, & V. Sasyuk. Wide-field optical monitoring with mini-megatortora (mmt-9) multichannel high temporal resolution telescope. *Astrophysical Bulletin*, 72:81–92, 02 2017. doi: 10.1134/S1990341317030105.

T. Borkovits, S. Albrecht, S. Rappaport, L. Nelson, A. Vanderburg, B. L. Gary, T. G. Tan, A. B. Justesen, M. H. Kristiansen, T. L. Jacobs, D. LaCourse, H. Ngo, N. Wallack, G. Ruane, D. Mawet, S. B. Howell, & R. Tronsgaard. EPIC 219217635: a doubly eclipsing quadruple system containing an evolved binary. *Monthly Notices of the Royal Astronomical Society*, 478(4):5135–5152, Aug. 2018. doi: 10.1093/mnras/sty1386.

T. Borkovits, S. A. Rappaport, P. F. L. Maxted, I. Terentev, M. Omohundro, R. Gagliano, T. Jacobs, M. H. Kristiansen, D. LaCourse, H. M. Schwengeler, A. Vanderburg, & M. G. Blackford. BG Ind: the nearest doubly eclipsing, compact hierarchical quadruple system. *Monthly Notices of the Royal Astronomical Society*, 503(3):3759–3774, May 2021. doi: 10.1093/mnras/stab621.

M. Brož, K. E. Conroy, & A. Prša. Physics Of Eclipsing Binaries. VIII. Multiple systems. *arXiv e-prints*, June 2025. doi: 10.48550/arXiv.2506.20866.

P. Cagaš. Silicups. http://var.astro.cz/oejv/issues/oejv0180.pdf#page=10, 2016. cit. 2024-03-12.

B. W. Carroll & D. A. Ostlie. *An Introduction to Modern Astrophysics*. Cambridge University Press, 2 edition, 2017.

F. Castelli & R. L. Kurucz. New Grids of ATLAS9 Model Atmospheres. In N. Piskunov, W. W. Weiss, & D. F. Gray, editors, *Modelling of Stellar Atmospheres*, volume 210 of *IAU Symposium*, page A20, Jan. 2003. doi: 10.48550/arXiv.astro-ph/0405087.

K. E. Conroy, A. Kochoska, D. Hey, H. Pablo, K. M. Hambleton, D. Jones, J. Giammarco, M. Abdul-Masih, & A. Prša. Physics of Eclipsing Binaries. V. General Framework for Solving the Inverse Problem. *The Astrophysical Journal Supplement Series*, 250(2): 34, Oct. 2020. doi: 10.3847/1538-4365/abb4e2.

I. Czekala, K. S. Mandel, S. M. Andrews, J. A. Dittmann, S. K. Ghosh, B. T. Montet, & E. R. Newton. Disentangling time-series spectra with gaussian processes: Applications to radial velocity analysis. *The Astrophysical Journal*, 840(1):49, may 2017. doi: 10.3847/1538-4357/aa6aab.

P. P. Eggleton & L. Kiseleva-Eggleton. Orbital Evolution in Binary and Triple Stars, with an Application to SS Lacertae. *The Astrophysical Journal*, 562(2):1012–1030, Dec. 2001. doi: 10.1086/323843.

X. Fang, T. A. Thompson, & C. M. Hirata. Dynamics of quadruple systems composed of two binaries: stars, white dwarfs, and implications for Ia supernovae. *Monthly Notices of the Royal Astronomical Society*, 476(3):4234–4262, May 2018. doi: 10.1093/mnras/sty472.

S. Freund, S. Czesla, J. Robrade, P. C. Schneider, & J. H. M. M. Schmitt. The stellar content of the ROSAT all-sky survey. *Astronomy & Astrophysics*, 664:A105, Aug. 2022. doi: 10.1051/0004-6361/202142573.

Gaia Collaboration. Gaia data release 2 - summary of the contents and survey properties. *Astronomy & Astrophysics*, 616:A1, 2018. doi: 10.1051/0004-6361/201833051.

Gaia Collaboration. Gaia data release 3 - summary of the content and survey properties. *Astronomy & Astrophysics*, 674:A1, 2023. doi: 10.1051/0004-6361/202243940.

P. Gajdoš. New features in software OCFIT. *Open European Journal on Variable Stars*, 241:1–9, Oct. 2023. doi: 10.5817/OEJV2023-0241.

P. Gajdoš & Š. Parimucha. New tool with GUI for fitting O-C diagrams. *Open European Journal on Variable Stars*, 197:71, Apr. 2019.

I. Gezer, G. Marton, J. Roquette, M. Audard, D. Hernandez, M. Madarász, & O. Dionatos. SED Modelling of Young Stellar Objects in the Orion Star Formation Complex. *Astronomy & Astrophysics*, 696, Apr. 2025. doi: 10.1051/0004-6361/202453624.

D. F. Gray. *The Observation and Analysis of Stellar Photospheres*. Cambridge University Press, 4 edition, 2021.

G. M. Green, E. Schlafly, C. Zucker, J. S. Speagle, & D. Finkbeiner. A 3d dust map based on gaia, pan-starrs 1, and 2mass. *The Astrophysical Journal*, 887(1):93, Dec. 2019. ISSN 1538-4357. doi: 10.3847/1538-4357/ab5362.

J. Grindlay, S. Tang, E. Los, & M. Servillat. Opening the 100-Year Window for Time-Domain Astronomy. In E. Griffin, R. Hanisch, & R. Seaman, editors, *New Horizons in Time Domain Astronomy*, volume 285 of *IAU Symposium*, pages 29–34, Apr. 2012. doi: 10.1017/S1743921312000166.

A. S. Hamers. Shrinking orbits in hierarchical quadruple star systems. *Monthly Notices of the Royal Astronomical Society*, 482(2):2262–2276, Jan. 2019. doi: 10.1093/mnras/sty2879.

A. A. Henden, S. Levine, D. Terrell, & D. L. Welch. APASS - The Latest Data Release. In *American Astronomical Society Meeting Abstracts #225*, volume 225 of *American Astronomical Society Meeting Abstracts*, page 336.16, Jan. 2015.

R. W. Hilditch. *An Introduction to Close Binary Stars*. Cambridge University Press, 2001.

T.-O. Husser, S. Wende-von Berg, S. Dreizler, D. Homeier, A. Reiners, T. Barman, & P. H. Hauschildt. A new extensive library of PHOENIX stellar atmospheres and synthetic spectra. *Astronomy & Astrophysics*, 553:A6, May 2013. doi: 10.1051/0004-6361/201219058.

D. Jones, K. E. Conroy, M. Horvat, J. Giammarco, A. Kochoska, H. Pablo, A. J. Brown, P. Sowicka, & A. Prša. Physics of Eclipsing Binaries. IV. The Impact of Interstellar Extinction on the Light Curves of Eclipsing Binaries. *The Astrophysical Journal Supplement Series*, 247(2):63, Apr. 2020. doi: 10.3847/1538-4365/ab7927.

P. Kabáth, M. Skarka, A. Hatzes, E. Guenther, L. Vanzi, R. Brahm, J. Janík, P. Pintr, P. Gajdoš, J. Lipták, J. Žák, H. M. J. Boffin, L. Antonucci, G. Avila, Z. Balkóová, M. E. Ball, M. Flores, A. Fuentes, J. Fuchs, R. Greimel, A. Gajardo, V. D. Ivanov, J. Köhler, M. Leitzinger, M. R. Ludwig, T. Moravčík, J. Nečásek, R. J. U. Neubert, P. Odert, G. Olguín, M. T. Pinto, M. Roth, L. Řezba, V. Schaffenroth, M. Sigwarth, J. Srba, A. Suárez, P. Škoda, J. Šubjak, J. Václavík, M. Veselý, R. Veselý, M. Vítková, J. U. Winkler, M. Zummer, & E. Žďárská. PLATOSpec: a precise spectrograph in support of space missions. *Monthly Notices of the Royal Astronomical Society*, 545(1): staf1972, Jan. 2026. doi: 10.1093/mnras/staf1972.

J. Kallrath & E. F. Milone. *Eclipsing Binary Stars: Modeling and Analysis*. Springer New York, 2009. doi: 10.1007/978-1-4419-0699-1_1.

J. Kolář, M. Zejda, A. Richterková, P. Dvořák, R. F. Auer, Z. Henzl, R. Dřevěný, S. Pačková, & M. Uhlár. Period ratios and observation of noticeable resonance at 3:2 for 2+2 quadruple systems. *Monthly Notices of the Royal Astronomical Society*, 538 (2):1160–1166, Apr. 2025. doi: 10.1093/mnras/staf364.

J. Kolář, S. Pačková, A. Richterková, M. Zejda, R. F. Auer, R. Dřevěný, J. Janík, M. Mašek, T. Merle, P. Ohlídal, T. Pribulla, M. Uhlár, P. Viewegh, & J. Vyskočil. Study of doubly eclipsing quadruples - I. Methodology and results for 10 Northern sky systems. *Monthly Notices of the Royal Astronomical Society*, 547(4):stag417, Apr. 2026. doi: 10.1093/mnras/stag417.

J. Kolář. *Studium vícenásobných hvězdných systémů*. Disertační práce, Masarykova univerzita, Přírodovědecká fakulta, 2025. URL https://is.muni.cz/th/m79qa/.

Z. Kopal. The classification of close binary systems. *Annales d'Astrophysique*, 18:379, 1955.

V. B. Kostov, B. P. Powell, S. A. Rappaport, T. Borkovits, R. Gagliano, T. L. Jacobs, M. H. Kristiansen, D. M. LaCourse, M. Omohundro, J. Orosz, A. R. Schmitt, H. M. Schwengeler, I. A. Terentev, G. Torres, T. Barclay, A. H. Friedman, E. Kruse, G. Olmschenk, A. Vanderburg, & W. Welsh. Ninety-seven Eclipsing Quadruple Star Candidates Discovered in TESS Full-frame Images. *The Astrophysical Journal Supplement Series*, 259(2):66, Apr. 2022a. doi: 10.3847/1538-4365/ac5458.

V. B. Kostov, B. P. Powell, S. A. Rappaport, T. Borkovits, R. Gagliano, T. L. Jacobs, M. H. Kristiansen, D. M. Lacourse, M. Omohundro, J. Orosz, A. R. Schmitt, H. M. Schwengeler, I. A. Terentev, G. Torres, T. Barclay, A. H. Friedman, E. Kruse, G. Olmschenk, A. Vanderburg, & W. Welsh. VizieR Online Data Catalog: Eclipsing quadruple star candidates from TESS (Kostov+, 2022), July 2022b.

Lightkurve Collaboration, J. V. d. M. Cardoso, C. Hedges, M. Gully-Santiago, N. Saunders, A. M. Cody, T. Barclay, O. Hall, S. Sagear, E. Turtelboom, J. Zhang, A. Tzanidakis, K. Mighell, J. Coughlin, K. Bell, Z. Berta-Thompson, P. Williams, J. Dotson, & G. Barentsen. Lightkurve: Kepler and TESS time series analysis in Python. Astrophysics Source Code Library, record ascl:1812.013, 2018.

A.-L. Luo, Y.-H. Zhao, G. Zhao, & et al. VizieR Online Data Catalog: LAMOST DR7 catalogs (Luo+, 2019), Mar. 2022.

R. A. Mardling & S. J. Aarseth. Tidal interactions in star cluster simulations. *Monthly Notices of the Royal Astronomical Society*, 321(3):398–420, Mar. 2001. doi: 10.1046/j.1365-8711.2001.03974.x.

Z. Mikulášek. Phenomenological modelling of eclipsing system light curves. *Astronomy & Astrophysics*, 584:A8, 2015. doi: 10.1051/0004-6361/201425244.

Z. Mikulášek & M. Zejda. *Úvod do studia proměnných hvězd*. Masaryk university, 2013.

D. Motl. Muniwin v2.1.34. https://c-munipack.sourceforge.net/, 2010. cit. 2025-05-28.

J. A. Nelder & R. Mead. A simplex method for function minimization. *The Computer Journal*, 7(4):308–313, 01 1965. ISSN 0010-4620. doi: 10.1093/comjnl/7.4.308.

S. A. Otero & P. A. Dubovsky. New Elements for 80 Eclipsing Binaries IV. *Information Bulletin on Variable Stars*, 5557:1, Aug. 2004.

M. Paegert, K. G. Stassun, K. A. Collins, J. Pepper, G. Torres, J. Jenkins, J. D. Twicken, & D. W. Latham. VizieR Online Data Catalog: TESS Input Catalog version 8.2 (TIC v8.2) (Paegert+, 2021). VizieR On-line Data Catalog: IV/39. Originally published in: 2021arXiv210804778P, Feb. 2022.

S. Pačková. Fotometrická analýza vícenásobně zákrytových systémů, 2024. URL https://is.muni.cz/th/k04bo/.

O. Pejcha. Ondřej Pejcha: Světelné křivky z TESS. https://www.youtube.com/watch?v=47g7ypzHTRI, 2020. cit. 2026-03-29.

O. Pejcha, P. Cagaš, C. Landri, M. M. Fausnaugh, G. De Rosa, J. L. Prieto, Z. Henzl, & M. Pešta. The complex dynamical past and future of double eclipsing binary CzeV343: Misaligned orbits and period resonance. *Astronomy & Astrophysics*, 667:A53, Nov. 2022. doi: 10.1051/0004-6361/202244335.

J. R. Percy. *Understanding Variable Stars*. Cambridge University Press, 2007.

M. A. C. Perryman, L. Lindegren, J. Kovalevsky, E. Hoeg, U. Bastian, P. L. Bernacca, M. Crézé, F. Donati, M. Grenon, M. Grewing, F. van Leeuwen, H. van der Marel, F. Mignard, C. A. Murray, R. S. Le Poole, H. Schrijver, C. Turon, F. Arenou, M. Froeschlé, & C. S. Petersen. The HIPPARCOS Catalogue. *Astronomy & Astrophysics*, 323:L49–L52, July 1997.

G. Pojmanski. The All Sky Automated Survey. Catalog of Variable Stars. I. 0 h - 6 hQuarter of the Southern Hemisphere. *Acta Astronomica*, 52:397–427, Dec. 2002. doi: 10.48550/arXiv.astro-ph/0210283.

D. L. Pollacco, I. Skillen, A. Collier Cameron, D. J. Christian, C. Hellier, J. Irwin, T. A. Lister, R. A. Street, R. G. West, D. R. Anderson, W. I. Clarkson, H. Deeg, B. Enoch, A. Evans, A. Fitzsimmons, C. A. Haswell, S. Hodgkin, K. Horne, S. R. Kane, F. P. Keenan, P. F. L. Maxted, A. J. Norton, J. Osborne, N. R. Parley, R. S. I. Ryans, B. Smalley, P. J. Wheatley, & D. M. Wilson. The WASP Project and the SuperWASP Cameras. *Publications of the Astronomical Society of the Pacific*, 118(848):1407–1418, Oct. 2006. doi: 10.1086/508556.

B. P. Powell, G. Torres, V. B. Kostov, T. Borkovits, S. A. Rappaport, M. Moe, D. W. Latham, T. L. Jacobs, R. Gagliano, M. H. K. Kristiansen, M. Omohundro, H. M. Schwengeler, D. M. LaCourse, I. A. Terentev, & A. R. Schmitt. The Discovery of Two Quadruple Star Systems with the Second and Third Shortest Outer Periods. *The Astrophysical Journal*, 985(2):213, June 2025. doi: 10.3847/1538-4357/adcece.

M. J. D. Powell. An efficient method for finding the minimum of a function of several variables without calculating derivatives. *The Computer Journal*, 7(2):155–162, 01 1964. ISSN 0010-4620. doi: 10.1093/comjnl/7.2.155.

T. Pribulla, T. Borkovits, R. Jayaraman, S. Rappaport, T. Mitnyan, P. Zasche, R. Komžík, A. Pál, R. Uhlař, M. Mašek, Z. Henzl, I. B. Bíró, I. Csányi, R. Stuik, M. H. Kristiansen, H. M. Schwengeler, R. Gagliano, T. L. Jacobs, M. Omohundro, V. Kostov, B. P. Powell, I. A. Terentev, A. Vanderburg, D. LaCourse, J. E. Rodriguez, G. Bakos, Z. Csubry, & J. Hartman. BU Canis Minoris - the most compact known flat doubly eclipsing quadruple system. *Monthly Notices of the Royal Astronomical Society*, 524(3):4220–4238, Sept. 2023. doi: 10.1093/mnras/stad2015.

A. Prša & T. Zwitter. A Computational Guide to Physics of Eclipsing Binaries. I. Demonstrations and Perspectives. *The Astrophysical Journal*, 628(1):426–438, July 2005. doi: 10.1086/430591.

A. Prša, K. E. Conroy, M. Horvat, H. Pablo, A. Kochoska, S. Bloemen, J. Giammarco, K. M. Hambleton, & P. Degroote. Physics Of Eclipsing Binaries. II. Toward the

Increased Model Fidelity. *The Astrophysical Journal Supplement Series*, 227(2):29, Dec. 2016. doi: 10.3847/1538-4365/227/2/29.

G. Raskin, H. van Winckel, H. Hensberge, A. Jorissen, H. Lehmann, C. Waelkens, G. Avila, J.-P. de Cuyper, P. Degroote, R. Dubosson, L. Dumortier, Y. Frémat, U. Laux, B. Michaud, J. Morren, J. Perez Padilla, W. Pessemier, S. Prins, K. Smolders, S. van Eck, & J. Winkler. HERMES: a high-resolution fibre-fed spectrograph for the Mercator telescope. *Astronomy & Astrophysics*, 526:A69, Feb. 2011. doi: 10.1051/0004-6361/201015435.

G. R. Ricker, J. N. Winn, R. Vanderspek, D. W. Latham, G. Á. Bakos, J. L. Bean, Z. K. Berta-Thompson, T. M. Brown, L. Buchhave, N. R. Butler, R. P. Butler, W. J. Chaplin, D. Charbonneau, J. Christensen-Dalsgaard, M. Clampin, D. Deming, J. Doty, N. De Lee, C. Dressing, E. W. Dunham, M. Endl, F. Fressin, J. Ge, T. Henning, M. J. Holman, A. W. Howard, S. Ida, J. M. Jenkins, G. Jernigan, J. A. Johnson, L. Kaltenegger, N. Kawai, H. Kjeldsen, G. Laughlin, A. M. Levine, D. Lin, J. J. Lissauer, P. MacQueen, G. Marcy, P. R. McCullough, T. D. Morton, N. Narita, M. Paegert, E. Palle, F. Pepe, J. Pepper, A. Quirrenbach, S. A. Rinehart, D. Sasselov, B. Sato, S. Seager, A. Sozzetti, K. G. Stassun, P. Sullivan, A. Szentgyorgyi, G. Torres, S. Udry, & J. Villasenor. Transiting Exoplanet Survey Satellite (TESS). *Journal of Astronomical Telescopes, Instruments, and Systems*, 1:014003, Jan. 2015. doi: 10.1117/1.JATIS.1.1.014003.

B. Shappee, J. Prieto, K. Z. Stanek, C. S. Kochanek, T. Holoien, J. Jencson, U. Basu, J. F. Beacom, D. Szczygiel, G. Pojmanski, J. Brimacombe, M. Dubberley, M. Elphick, S. Foale, E. Hawkins, D. Mullins, W. Rosing, R. Ross, & Z. Walker. All Sky Automated Survey for SuperNovae (ASAS-SN or "Assassin"). In *American Astronomical Society Meeting Abstracts #223*, volume 223 of *American Astronomical Society Meeting Abstracts*, page 236.03, Jan. 2014.

C. Sterken & C. Jaschek. *Light Curves of Variable Stars: A Pictorial Atlas*. Cambridge University Press, 1996.

M. A. B. Terry D. Oswalt. *Planets, Stars and Stellar Systems*. Springer Dordrecht, 2013.

D. Tody. The IRAF Data Reduction and Analysis System. In D. L. Crawford, editor, *Instrumentation in astronomy VI*, volume 627 of *Society of Photo-Optical Instrumentation Engineers (SPIE) Conference Series*, page 733, Jan. 1986. doi: 10.1117/12.968154.

A. Tokovinin. Comparative statistics and origin of triple and quadruple stars. *Monthly Notices of the Royal Astronomical Society*, 389(2):925–938, Sept. 2008. doi: 10.1111/j.1365-2966.2008.13613.x.

A. Tokovinin. From Binaries to Multiples. II. Hierarchical Multiplicity of F and G Dwarfs. *The Astronomical Journal*, 147(4):87, Apr. 2014. doi: 10.1088/0004-6256/147/4/87.

A. Tokovinin. Architecture of hierarchical stellar systems and their formation. *Universe*, 7(9):352, 2021.

J. L. Tonry, L. Denneau, A. N. Heinze, B. Stalder, K. W. Smith, S. J. Smartt, C. W. Stubbs, H. J. Weiland, & A. Rest. ATLAS: A High-cadence All-sky Survey System. *Publications of the Astronomical Society of the Pacific*, 130(988):064505, June 2018. doi: 10.1088/1538-3873/aabadf.

G. Torres, C. H. Sandberg Lacy, F. C. Fekel, M. Wolf, & M. W. Muterspaugh. The Quadruple-lined, Doubly Eclipsing System V482 Persei. *The Astrophysical Journal*, 846(2):115, Sept. 2017. doi: 10.3847/1538-4357/aa8633.

C. L. Watson, A. A. Henden, & A. Price. The International Variable Star Index (VSX). *Society for Astronomical Sciences Annual Symposium*, 25:47, May 2006.

H. Willems. Determining the physical parameters of eclipsing binaries from the B-Type binaries characterization programme (BBC) with PHOEBE. *Contributions of the Astronomical Observatory Skalnaté Pleso*, 55(3), 2025. doi: 10.31577/caosp.2025.55.3.444.

R. E. Wilson & E. J. Devinney. Realization of Accurate Close-Binary Light Curves: Application to MR Cygni. *The Astrophysical Journal*, 166:605, June 1971. doi: 10.1086/150986.

C. Winkler, T. J.-L. Courvoisier, G. Di Cocco, N. Gehrels, A. Giménez, S. Grebenev, W. Hermsen, J. M. Mas-Hesse, F. Lebrun, N. Lund, G. G. C. Palumbo, J. Paul, J.-P. Roques, H. Schnopper, V. Schönfelder, R. Sunyaev, B. Teegarden, P. Ubertini, G. Vedrenne, & A. J. Dean. The INTEGRAL mission. *Astronomy & Astrophysics*, 411:L1–L6, Nov. 2003. doi: 10.1051/0004-6361:20031288.

P. Zasche, D. Vokrouhlický, M. Wolf, H. Kučáková, J. Kára, R. Uhlař, M. Mašek, Z. Henzl, & P. Cagaš. Doubly eclipsing systems. *Astronomy & Astrophysics*, 630:A128, Oct. 2019. doi: 10.1051/0004-6361/201936328.

P. Zasche, Z. Henzl, H. Lehmann, J. Pepper, B. P. Powell, V. B. Kostov, T. Barclay, M. Wolf, H. Kučáková, R. Uhlař, M. Mašek, S. Palafouta, K. Gazeas, K. G. Stassun, B. S. Gaudi, J. E. Rodriguez, & D. J. Stevens. CzeV1731: The unique doubly eclipsing quadruple system. *Astronomy & Astrophysics*, 642:A63, Oct. 2020. doi: 10.1051/0004-6361/202038656.

P. Zasche, Z. Henzl, & J. Kára. The first study of four doubly eclipsing systems. *Astronomy & Astrophysics*, 659:A8, Mar. 2022a. doi: 10.1051/0004-6361/202142771.

P. Zasche, Z. Henzl, & M. Mašek. Multiply eclipsing candidates from the tess satellite. *Astronomy & Astrophysics*, 664:A96, 2022b. doi: 10.1051/0004-6361/202243723.

P. Zasche, Z. Henzl, M. Mašek, R. Uhlař, J. Kára, J. Merc, & H. Kučáková. Detection of seven 2+2 doubly eclipsing quadruple systems. *Astronomy & Astrophysics*, 675: A113, July 2023. doi: 10.1051/0004-6361/202346848.

P. Zasche, Z. Henzl, J. Merc, J. Kára, & H. Kučáková. Eight new 2+2 doubly eclipsing quadruple systems detected. *Astronomy & Astrophysics*, 687:A6, July 2024. doi: 10.1051/0004-6361/202450400.

P. Zasche, Z. Henzl, M. Mašek, J. Kára, H. Kučáková, J. Merc, & R. Uhlař. Three new 2+2 quadruple systems with changing inclination. *Monthly Notices of the Royal Astronomical Society*, 539(2):1015–1023, Apr. 2025. ISSN 1365-2966. doi: 10.1093/mnras/staf495.

Appendices

Scripts

Script A.1: Script used to download, detrend, and extract differential photometry from TESS Full Frame Images (Ondřej Pejcha).

```
import pandas as pd
import numpy as np
import math
import lightkurve as lk
import matplotlib.pyplot as plt

search_results = lk.search_tesscut("RA DE")
search_results

tpfs = search_results.download_all(cutout_size=20, quality_bitmask='hardest')

i =
tpfs[i].plot()

target_mask = tpfs[i].create_threshold_mask(threshold=150, reference_pixel='center')
target_mask[9:12, 9:12] = 1
tpfs[i].plot(aperture_mask=target_mask, mask_color='r')
n_target_pixels = target_mask.sum()
n_target_pixels

target_lc = tpfs[i].to_lightcurve(aperture_mask=target_mask)
bg_mask = ~tpfs[i].create_threshold_mask(threshold=0.001, reference_pixel=None)
tpfs[i].plot(aperture_mask=bg_mask, mask_color='w')

n_bg_pixels = bg_mask.sum()
n_bg_pixels

bg_lc_per_pixel = tpfs[i].to_lightcurve(aperture_mask=bg_mask) / n_bg_pixels
bg_estimate_lc = bg_lc_per_pixel * n_target_pixels
corr_lc = target_lc - bg_estimate_lc.flux
corr_lc.plot()

corr_lc.flatten(601).plot()

corr_lc.time = corr_lc.time + tpfs[i].get_keyword('BJDREFI') + tpfs[i].get_keyword('
    BJDREFF')
name = "star{}".format(i) + ".csv"
corr_lc.flatten(601).to_csv(name)

period =
M0 =
```

```
corr_lc.flatten(601).fold(period, t0=M0).scatter()

search_results_cmp = lk.search_tesscut('RA DE')
search_results_cmp

tpfs_cmp =search_results_cmp.download_all(cutout_size=20, quality_bitmask='hardest')

i =
tpfs_cmp[i].plot()

target_mask_cmp = tpfs_cmp[i].create_threshold_mask(threshold=150, reference_pixel='
    center')
target_mask_cmp[9:12, 9:12] = 1

tpfs_cmp[i].plot(aperture_mask=target_mask_cmp, mask_color='r')
n_target_cmp_pixels = target_mask_cmp.sum()
n_target_cmp_pixels

target_cmp_lc = tpfs_cmp[i].to_lightcurve(aperture_mask=target_mask_cmp)
bg_mask_cmp = ~tpfs_cmp[i].create_threshold_mask(threshold=0.001, reference_pixel=None)
n_bg_cmp_pixels = bg_mask_cmp.sum()

bg_cmp_lc_per_pixel = tpfs_cmp[i].to_lightcurve(aperture_mask=bg_mask_cmp) /
    n_bg_cmp_pixels
bg_estimate_cmp_lc = bg_cmp_lc_per_pixel * n_target_cmp_pixels
corr_cmp_lc = target_cmp_lc - bg_estimate_cmp_lc.flux

corr_cmp_lc.time = corr_cmp_lc.time + tpfs_cmp[i].get_keyword('BJDREFI') + tpfs_cmp[i].
    get_keyword('BJDREFF')
name_cmp = "star_cmp_{}".format(i) + ".csv"
corr_cmp_lc.flatten(601).to_csv(name_cmp)

for i in range(len(tpfs)):
    name = "star{}".format(i) + ".csv"
    name_cmp = "star_cmp_{}".format(i) + ".csv"
    variable = pd.read_csv(name, thousands=r" ", sep=",", decimal=".")
    comparison = pd.read_csv(name_cmp, thousands=r" ", sep=",", decimal=".")
    change_data = pd.concat([variable["time"], comparison["time"], variable["flux"],
        comparison["flux"], variable["flux_err"], comparison["flux_err"]], axis=1)
    change_data.columns = ["var_time", "comp_time", "var_flux", "comp_flux", "
        var_flux_err", "comp_flux_err"]
    change = -2.5 * np.log10(change_data["var_flux"] / change_data["comp_flux"])
    error = (((2.5 * change_data["comp_flux_err"]) / change_data["var_flux"])**2 +
        ((2.5 * change_data["var_flux_err"]) / change_data["comp_flux"])**2)**0.5
    ch = change.tolist()
    final_change = []

    for j in range(len(ch)):
        a = ch[j]
        x = "%.17f" % a
        final_change.append(x)
    change = pd.Series(final_change)
    err = error.tolist()
    final_error = []

    for k in range(len(err)):
        b = err[k]
        y = "%.17f" % b
        final_error.append(y)
    error = pd.Series(final_error)
```

```
    time = variable["time"]
    final_data = pd.concat([time, change, error], axis=1)
    final_name = "star{}".format(i) + "_final.txt"
    np.savetxt(final_name, final_data, fmt='%s', delimiter='\t' )
```

Script A.2: Python script for detrending light curves using Chebyshev polynomials (Jakub Kolář).

```
import numpy as np
import matplotlib.pyplot as plt

t, mag, err = np.loadtxt("reziduals.txt", unpack=True)

plt.figure(figsize=(18,12))
plt.tick_params(bottom=True, top=True, left=True, right=True)
plt.xticks(fontsize=26)
plt.yticks(fontsize=26)
plt.tick_params(axis="x", length=15, direction="in", pad=15)
plt.tick_params(axis="y", length=15, direction="in", pad=15)
plt.plot(t, mag, "o", color="blue")
plt.errorbar(t, mag, yerr=err, fmt='o', color="b", ecolor="b")
plt.gca().invert_yaxis()

p = np.polynomial.Chebyshev.fit(t, mag, 3)

y_tr = p(t)

plt.figure(figsize=(18,12))
plt.tick_params(bottom=True, top=True, left=True, right=True)
plt.xticks(fontsize=26)
plt.yticks(fontsize=26)
plt.tick_params(axis="x", length=15, direction="in", pad=15)
plt.tick_params(axis="y", length=15, direction="in", pad=15)
plt.plot(t, mag, "o", color="blue")
plt.plot(t, y_tr, "-", color="orange", linewidth=5)
plt.gca().invert_yaxis()

np.savetxt("trend.txt", y_tr, delimiter='', fmt="%.5f")

t, mag, err = np.loadtxt("data_with_trend.txt", unpack=True)

plt.figure(figsize=(18,12))
plt.tick_params(bottom=True, top=True, left=True, right=True)
plt.xticks(fontsize=26)
plt.yticks(fontsize=26)
plt.tick_params(axis="x", length=15, direction="in", pad=15)
plt.tick_params(axis="y", length=15, direction="in", pad=15)
plt.plot(t, mag, "o", color="blue")
plt.errorbar(t, mag, yerr=err, fmt='o', color="b", ecolor="b")
plt.gca().invert_yaxis()

mag_new = mag - y_tr

plt.figure(figsize=(18,12))
plt.tick_params(bottom=True, top=True, left=True, right=True)
plt.xticks(fontsize=26)
plt.yticks(fontsize=26)
plt.tick_params(axis="x", length=15, direction="in", pad=15)
plt.tick_params(axis="y", length=15, direction="in", pad=15)
plt.plot(t, mag_new, "o", color="blue")
```

```
plt.errorbar(t, mag_new, yerr=err, fmt='o', color="b", ecolor="b")
plt.gca().invert_yaxis()

np.savetxt("detrended.txt", np.c_[t, mag_new, err], delimiter=' ', fmt="%.5f")
```

Log of Photometric Observations

Tables A.1 and A.2 present a complete log of the photometric observations obtained for the candidate systems S1 CMi and S4 Vel.

Table A.1: Log of photometric observations for the system S1 CMi.

Date	**Observer**	**Observatory**	**Filters**
01.02.2025	Zejda	Ždánice	g', r'
04.02.2025	Zejda	Ždánice	g', r'
10.02.2025	Zejda	Ždánice	g', r'
19.02.2025	Kolář	Ždánice	g', r'
06.03.2025	Zejda	Ždánice	g', r'
07.03.2025	Zejda	Ždánice	g', r'
01.12.2025	Zejda	Boyden	g', r'
03.12.2025	Pačková	Boyden	g', r'
13.12.2025	Zejda	Boyden	g', r'
17.12.2025	Pačková	Boyden	g', r'
26.12.2025	Kolář	Ždánice	g', r'
28.12.2025	Zejda	Ždánice	g', r'
07.01.2026	Zejda	Boyden	g', r'
21.01.2026	Kolář	Ždánice	g', r'
23.01.2026	Zejda	Boyden	g', r'
27.01.2026	Zejda	Boyden	g', r'
	Additional Observations		
11.12.2025	Haltuf	Gemini	V, R
17.12.2025	Haltuf	Gemini	V, R
01.01.2026	Haltuf	Gemini	V, R
09.01.2026	Haltuf	Gemini	V, R
10.01.2026	Haltuf	Gemini	V, R

Table A.2: Log of photometric observations for the system S4 Vel.

Date	**Observer**	**Observatory**	**Filters**
09.05.2025	Zejda	Boyden	r'
12.05.2025	Zejda	Boyden	r'
05.06.2025	Zejda	Boyden	g'
16.06.2025	Zejda	Boyden	g', r'
26.11.2025	Zejda	Boyden	g', r'
02.12.2025	Zejda	Boyden	g', r'
18.12.2025	Pačková	Boyden	g', r'
06.01.2026	Zejda	Boyden	g', r'
24.01.2026	Zejda	Boyden	g', r'
11.02.2026	Zejda	Boyden	g', r'
14.02.2026	Zejda	Boyden	g', r'
24.02.2026	Zejda	Boyden	g', r'
	Additional Observations		
05.06.2025	Zejda	Boyden	i'
16.06.2025	Zejda	Boyden	i'

Log of Spectroscopic Observations

Tables A.3 and A.4 present a complete log of the spectroscopic observations obtained for the candidate systems S1 CMi and S4 Vel.

Table A.3: Log of spectroscopic observations for the system S1 CMi.

HJD (start) (days)	**Exposure** (s)	**Instrument**	**Observatory**	**Observer**	**Phase A**	**Phase B**
2 460 730.530 30	1800	PLATOSpec	La Silla	Janík	0.319	0.532
2 460 972.788 37	2400	PLATOSpec	La Silla	Janík	0.020	0.417
2 460 972.853 81	2400	PLATOSpec	La Silla	Janík	0.039	0.435
2 460 997.810 67	2400	PLATOSpec	La Silla	Janík	0.116	0.119
2 460 999.716 92	2400	PLATOSpec	La Silla	Janík	0.657	0.630
2 461 034.656 92	2400	PLATOSpec	La Silla	Janík	0.565	0.988
2 461 034.706 89	2400	PLATOSpec	La Silla	Janík	0.579	0.001
2 461 034.821 67	2400	PLATOSpec	La Silla	Janík	0.612	0.032
2 461 035.609 24	2400	PLATOSpec	La Silla	Janík	0.835	0.243
2 461 035.685 73	2400	PLATOSpec	La Silla	Janík	0.857	0.263
2 461 035.740 93	2400	PLATOSpec	La Silla	Janík	0.873	0.278
2 461 036.643 53	2400	PLATOSpec	La Silla	Janík	0.129	0.520
2 461 036.690 06	2400	PLATOSpec	La Silla	Janík	0.142	0.532
2 461 036.737 75	2400	PLATOSpec	La Silla	Janík	0.155	0.545
2 461 037.608 31	2400	PLATOSpec	La Silla	Janík	0.402	0.778
2 461 037.720 33	2400	PLATOSpec	La Silla	Janík	0.434	0.808
2 461 106.524 47	2400	PLATOSpec	La Silla	Janík	0.946	0.237
2 461 106.577 71	2400	PLATOSpec	La Silla	Janík	0.961	0.251
Additional Observations						
2 460 661.581 11	1800	HERMES	La Palma	Merle	0.766	0.065
2 460 700.555 65	1200	HERMES	La Palma	Shchechilin	0.819	0.503
2 460 701.568 57	1400	HERMES	La Palma	Shchechilin	0.106	0.775
2 460 702.548 29	923	HERMES	La Palma	Shchechilin	0.384	0.037
2 460 703.491 84	1192	HERMES	La Palma	Shchechilin	0.652	0.290
2 460 704.632 20	1200	HERMES	La Palma	Shchechilin	0.975	0.595
Unusable Observations						
2 460 997.729 28	2400	PLATOSpec	La Silla	Janík	0.093	0.097
2 461 030.847 96	2400	PLATOSpec	La Silla	Janík	0.485	0.968
2 461 037.654 48	2400	PLATOSpec	La Silla	Janík	0.415	0.791

Table A.4: Log of spectroscopic observations for the system S4 Vel.

HJD (start) (days)	**Exposure** (s)	**Instrument**	**Observatory**	**Observer**	Phase A	Phase B
2 460 725.776 18	1800	PLATOSpec	La Silla	Janík	0.473	0.290
2 460 725.797 09	1800	PLATOSpec	La Silla	Janík	0.487	0.328
2 460 725.817 98	1800	PLATOSpec	La Silla	Janík	0.502	0.367
2 460 725.838 88	1800	PLATOSpec	La Silla	Janík	0.516	0.405
2 460 725.862 93	1800	PLATOSpec	La Silla	Janík	0.532	0.449
2 460 730.800 66	1800	PLATOSpec	La Silla	Janík	0.894	0.510
2 460 730.821 56	1800	PLATOSpec	La Silla	Janík	0.909	0.548
2 460 730.843 18	1800	PLATOSpec	La Silla	Janík	0.923	0.588
2 460 730.865 04	1800	PLATOSpec	La Silla	Janík	0.938	0.628
2 460 772.622 10	1800	PLATOSpec	La Silla	Janík	0.372	0.250
2 460 772.750 88	1800	PLATOSpec	La Silla	Janík	0.460	0.487
2 460 772.771 78	1800	PLATOSpec	La Silla	Janík	0.474	0.525
2 460 772.792 67	1800	PLATOSpec	La Silla	Janík	0.488	0.563
2 461 102.733 49	1800	PLATOSpec	La Silla	Janík	0.156	0.991
2 461 102.754 38	1800	PLATOSpec	La Silla	Janík	0.171	0.029
2 461 102.775 88	1800	PLATOSpec	La Silla	Janík	0.185	0.069
2 461 102.796 78	1800	PLATOSpec	La Silla	Janík	0.199	0.107
2 461 102.821 13	1800	PLATOSpec	La Silla	Janík	0.216	0.152
2 461 102.842 03	1800	PLATOSpec	La Silla	Janík	0.230	0.190
2 461 102.863 12	1800	PLATOSpec	La Silla	Janík	0.245	0.229
2 461 102.884 02	1800	PLATOSpec	La Silla	Janík	0.259	0.267
2 461 103.778 47	1800	PLATOSpec	La Silla	Janík	0.868	0.908
2 461 106.501 72	1800	PLATOSpec	La Silla	Janík	0.722	0.905
2 461 106.555 30	1800	PLATOSpec	La Silla	Janík	0.759	0.004
2 461 106.609 76	1800	PLATOSpec	La Silla	Janík	0.796	0.104
2 461 106.630 65	1800	PLATOSpec	La Silla	Janík	0.810	0.142
2 461 106.653 34	1800	PLATOSpec	La Silla	Janík	0.825	0.184
2 461 106.674 24	1800	PLATOSpec	La Silla	Janík	0.840	0.222
2 461 106.814 58	1800	PLATOSpec	La Silla	Janík	0.935	0.480
2 461 106.835 48	1800	PLATOSpec	La Silla	Janík	0.949	0.518
2 461 106.856 38	1800	PLATOSpec	La Silla	Janík	0.964	0.556

List of Minima Timings

The derived minima timings used to create the $O-C$ diagrams are presented in Tables A.5 and A.6.

Table A.5: Minima timings for pairs A and B of the system S1 CMi.

Pair A				**Pair B**			
HJD - 2450000	***O−C*** (days)	**Error**	**Type**	**HJD - 2450000**	***O−C*** (days)	**Error**	**Type**
3542.92880	0.0759	0.0037	P	3787.64109	−0.0950	0.0040	P
3544.68930	0.0739	0.0037	S	7778.97155	−0.0096	0.0040	P
8479.63929	0.0000	0.0040	P	11027.19181	−0.0431	0.0008	P
9572.78355	−0.0013	0.0040	P	11051.14174	−0.0426	0.0072	S
7398.83570	0.0026	0.0040	S	10711.38644	−0.0500	0.0031	S
8007.11831	0.0000	0.0040	P	10717.29589	−0.0482	0.0015	P
11050.33542	0.0409	0.0014	P	10885.30970	−0.0475	0.0003	P
10708.27525	0.0295	0.0060	P	10886.86940	−0.0474	0.0003	S
10888.11530	0.0295	0.0010	P	11023.45415	−0.0472	0.0009	P
10889.86900	0.0294	0.0010	S	10711.38945	−0.0487	0.0024	S
11048.55080	0.0288	0.0060	S	10726.32422	−0.0484	0.0049	S
11064.42909	0.0295	0.0060	P	10885.31110	−0.0461	0.0003	P
10320.36586	0.0105	0.0080	P	10886.87240	−0.0461	0.0003	S
10708.28464	0.0389	0.0060	P	11023.45531	−0.0460	0.0004	P
10888.12170	0.0359	0.0020	P	8492.10403	0.0005	0.0013	P
10889.87920	0.0321	0.0020	S	8495.83801	0.0008	0.0002	P
11011.54042	0.0350	0.0060	P	8497.38750	0.0027	0.0010	S
8491.98320	0.0045	0.0014	S	8499.57171	0.0009	0.0006	P
8493.74403	−0.0004	0.0023	P	8501.11820	−0.0002	0.0002	S
8495.50835	0.0034	0.0019	S	8504.85132	−0.0008	0.0018	S
8497.27084	0.0002	0.0018	P	8507.03874	0.0007	0.0004	P
8499.03270	0.0015	0.0009	S	8508.58776	0.0021	0.0014	S
8500.79678	−0.0002	0.0012	P	8510.77220	0.0005	0.0003	P
8502.56073	0.0032	0.0038	S	8512.32111	0.0018	0.0012	S
8506.08790	0.0041	0.0028	S	8514.50550	0.0002	0.0017	P
8509.61211	0.0021	0.0004	S	9203.04038	0.0004	0.0015	S
8511.37570	−0.0001	0.0010	P	9205.22690	0.0010	0.0004	P
8513.13861	0.0023	0.0016	S	9206.77366	0.0001	0.0034	S
8514.90189	−0.0002	0.0005	P	9208.96028	0.0007	0.0004	P
9202.52573	−0.0001	0.0003	P	9210.50614	−0.0011	0.0023	S
9204.28968	0.0033	0.0015	S	9212.69344	0.0003	0.0004	P
9206.05167	−0.0005	0.0002	P	9217.97429	−0.0002	0.0021	S

Continued on next page...

Table A.5: Minima timings for pairs A and B of the system S1 CMi (Continued).

Pair A				Pair B			
HJD - 2450000	***O−C*** (days)	**Error**	**Type**	**HJD - 2450000**	***O−C*** (days)	**Error**	**Type**
9207.81400	0.0013	0.0013	S	9220.16003	−0.0004	0.0013	P
9209.57822	−0.0002	0.0005	P	9221.70838	0.0003	0.0031	S
9211.34159	0.0026	0.0008	S	11027.19250	−0.0424	0.0012	P
9213.10435	−0.0003	0.0003	P				
9218.39505	0.0035	0.0010	S				
9220.15667	−0.0006	0.0003	P				
9221.92155	0.0038	0.0007	S				
9225.44870	0.0046	0.0013	S				
9227.20969	−0.0001	0.0003	P				
11050.33593	0.0414	0.0008	P				

Table A.6: Minima timings for pairs A and B of the system S4 Vel.

Pair A				Pair B			
HJD - 2450000	***O−C*** (days)	**Error**	**Type**	**HJD - 2450000**	***O−C*** (days)	**Error**	**Type**
2669.79630	−0.1787	0.0040	P	10808.21135	0.0094	0.0023	S
3131.66156	−0.1783	0.0040	S	11103.32190	0.0138	0.0031	P
8560.40400	−0.0053	0.0050	P	11047.46088	0.0132	0.0011	S
8561.13800	−0.0051	0.0050	S	11086.42379	0.0101	0.0044	P
9287.35600	0.0046	0.0060	P	11099.50331	0.0101	0.0011	P
9288.09000	0.0047	0.0060	S	11103.31738	0.0093	0.0059	P
9657.43300	0.0019	0.0060	P	11047.46088	0.0132	0.0011	S
9658.16700	0.0021	0.0060	S	11086.42379	0.0101	0.0044	P
10012.83000	0.0050	0.0060	P	11099.50331	0.0101	0.0011	P
10013.56400	0.0051	0.0060	S	11103.31738	0.0093	0.0059	P
7692.47700	−0.0074	0.0030	P	8544.09636	0.0097	0.0013	P
7693.21000	−0.0083	0.0030	S	8544.37081	0.0116	0.0008	S
8200.60300	−0.0066	0.0040	P	8544.64241	0.0107	0.0003	P
8201.33700	−0.0065	0.0040	S	8544.91789	0.0137	0.0018	S
10832.29000	0.0029	0.0008	P	8545.18846	0.0118	0.0016	P
10843.30367	0.0023	0.0006	S	8545.46002	0.0109	0.0003	S
10970.33640	0.0038	0.0001	P	8546.00361	0.0095	0.0017	S
10971.06910	0.0022	0.0001	S	8546.27788	0.0113	0.0014	P
11047.43451	0.0019	0.0004	S	8546.55364	0.0145	0.0002	S
11083.41604	0.0035	0.0004	P	8546.82179	0.0102	0.0002	P

Continued on next page...

Table A.6: Minima timings for pairs A and B of the system S4 Vel (Continued).

Pair A				Pair B			
HJD - 2450000	***O−C*** (days)	**Error**	**Type**	**HJD - 2450000**	***O−C*** (days)	**Error**	**Type**
11086.35306	0.0034	0.0003	P	8547.09643	0.0124	0.0033	S
11099.57166	0.0049	0.0005	P	8547.36676	0.0102	0.0028	P
11108.38185	0.0036	0.0006	P	8547.63910	0.0101	0.0019	S
10832.28952	0.0024	0.0010	P	8548.18439	0.0104	0.0001	S
10843.30462	0.0033	0.0010	S	8548.45702	0.0105	0.0003	P
5934.57612	−0.0300	0.0030	P	8548.73217	0.0132	0.0001	S
6083.63598	−0.0296	0.0030	S	8549.00139	0.0099	0.0001	P
7356.90607	−0.0097	0.0030	S	8549.82122	0.0123	0.0010	S
10843.30344	0.0021	0.0003	S	8550.36384	0.0099	0.0003	S
10957.11890	0.0034	0.0001	P	8550.63689	0.0105	0.0001	P
10957.85220	0.0024	0.0001	S	8550.90871	0.0098	0.0008	S
11047.43463	0.0021	0.0004	S	8551.18032	0.0089	0.0007	P
11083.41649	0.0039	0.0003	P	8551.45417	0.0103	0.0003	S
11086.35329	0.0036	0.0002	P	8551.72763	0.0112	0.0001	P
11099.57012	0.0033	0.0002	P	8552.00036	0.0115	0.0033	S
11108.38235	0.0041	0.0003	P	8552.27086	0.0095	0.0027	P
5616.61815	−0.0421	0.0033	S	8552.54373	0.0099	0.0002	S
5617.35349	−0.0415	0.0014	P	8552.81662	0.0103	0.0004	P
5619.55735	−0.0401	0.0004	S	8553.36159	0.0103	0.0006	P
5631.30301	−0.0430	0.0007	S	8553.63524	0.0114	0.0009	S
5633.50586	−0.0434	0.0012	P	8553.90843	0.0121	0.0004	P
5636.44460	−0.0418	0.0003	P	8554.18083	0.0120	0.0002	S
5656.26932	−0.0423	0.0006	S	8554.72510	0.0113	0.0015	S
5661.41037	−0.0417	0.0004	P	8554.99689	0.0106	0.0011	P
5681.23789	−0.0395	0.0010	S	8555.27163	0.0129	0.0007	S
5954.39716	−0.0342	0.0035	S	8557.17707	0.0109	0.0001	P
5956.60080	−0.0339	0.0010	P	8557.72153	0.0104	0.0002	P
5962.47583	−0.0331	0.0006	P	8557.99459	0.0109	0.0004	S
5970.55247	−0.0332	0.0004	S	8558.26875	0.0126	0.0037	P
5973.48941	−0.0334	0.0014	S	8559.35771	0.0116	0.0004	P
5978.63537	−0.0278	0.0031	P	8560.17282	0.0093	0.0004	S
5979.36402	−0.0330	0.0012	S	8560.71871	0.0102	0.0006	S
5981.56940	−0.0310	0.0005	P	8560.99189	0.0109	0.0022	P
5984.50515	−0.0324	0.0009	P	8561.53725	0.0112	0.0003	P
5990.37766	−0.0341	0.0008	P	8562.08191	0.0109	0.0005	P
5993.31566	−0.0333	0.0009	P	8562.35580	0.0123	0.0019	S
5998.45595	−0.0325	0.0008	S	8562.62632	0.0104	0.0014	P

Continued on next page...

Table A.6: Minima timings for pairs A and B of the system S4 Vel (Continued).

Pair A				Pair B			
HJD - 2450000	***O−C*** (days)	**Error**	**Type**	**HJD - 2450000**	***O−C*** (days)	**Error**	**Type**
6004.33397	−0.0288	0.0035	S	8562.89872	0.0103	0.0002	S
6006.53276	−0.0333	0.0008	P	8563.17173	0.0108	0.0005	P
6007.26891	−0.0310	0.0013	S	8563.71706	0.0111	0.0017	P
6015.34494	−0.0325	0.0006	P	8564.26096	0.0100	0.0011	P
6018.28194	−0.0327	0.0007	P	8564.53508	0.0117	0.0007	S
6020.48604	−0.0310	0.0005	S	8565.07955	0.0112	0.0028	S
6029.29637	−0.0321	0.0007	S	8565.35287	0.0120	0.0006	P
6040.31037	−0.0328	0.0004	P	8566.71407	0.0108	0.0008	S
6054.26296	−0.0312	0.0004	S	8567.80746	0.0142	0.0016	S
6059.40259	−0.0320	0.0012	P	8568.07622	0.0105	0.0006	P
6068.21581	−0.0302	0.0013	P	8568.34911	0.0109	0.0007	S
6076.29088	−0.0318	0.0006	S	8570.80071	0.0100	0.0005	P
6079.22839	−0.0314	0.0008	S	8571.34551	0.0099	0.0004	P
6299.51950	−0.0258	0.0020	S	8571.61832	0.0102	0.0005	S
6316.40833	−0.0260	0.0030	P	8571.89176	0.0111	0.0018	P
6329.62372	−0.0277	0.0022	P	8572.43565	0.0101	0.0004	P
6330.35600	−0.0293	0.0037	S	8572.71004	0.0120	0.0015	S
6338.44321	−0.0197	0.0031	P	8572.98259	0.0120	0.0013	P
6346.51188	−0.0277	0.0027	S	8573.25353	0.0105	0.0003	S
6355.32300	−0.0280	0.0028	S	8573.79778	0.0097	0.0003	S
6357.52819	−0.0261	0.0023	P	8574.07181	0.0113	0.0001	P
6363.40062	−0.0279	0.0020	P	8574.34510	0.0121	0.0018	S
6369.27355	−0.0293	0.0032	P	8574.61626	0.0107	0.0003	P
6371.47996	−0.0253	0.0024	S	8574.88928	0.0113	0.0014	S
6388.36894	−0.0253	0.0004	P	8575.43350	0.0105	0.0003	S
6396.44735	−0.0236	0.0023	S	8575.70689	0.0114	0.0004	P
6413.33154	−0.0284	0.0028	P	8575.97960	0.0116	0.0018	S
6419.21286	−0.0214	0.0018	P	8576.25118	0.0107	0.0008	P
6424.35154	−0.0222	0.0017	S	8576.79643	0.0110	0.0011	P
6427.28613	−0.0248	0.0011	S	8577.06905	0.0111	0.0010	S
6430.22652	−0.0215	0.0022	S	8577.34044	0.0100	0.0004	P
6438.30283	−0.0228	0.0030	P	8577.61237	0.0095	0.0006	S
6441.23820	−0.0246	0.0024	P	8577.88719	0.0118	0.0009	P
6449.31560	−0.0239	0.0034	S	8578.43107	0.0107	0.0018	P
6714.39748	−0.0193	0.0005	P	8578.97578	0.0104	0.0013	P
6725.41107	−0.0196	0.0020	S	8579.24920	0.0114	0.0023	S
6739.35848	−0.0240	0.0020	P	8579.79341	0.0106	0.0002	S

Continued on next page...

Table A.6: Minima timings for pairs A and B of the system S4 Vel (Continued).

Pair A				Pair B			
HJD - 2450000	***O−C*** (days)	**Error**	**Type**	**HJD - 2450000**	***O−C*** (days)	**Error**	**Type**
6753.30990	−0.0236	0.0020	S	8580.06603	0.0107	0.0009	P
8544.25405	−0.0010	0.0006	P	8580.33920	0.0114	0.0044	S
8544.98719	−0.0017	0.0005	S	8580.61032	0.0100	0.0009	P
8545.72212	−0.0015	0.0008	P	8581.15427	0.0090	0.0014	P
8546.45663	−0.0008	0.0003	S	8581.42825	0.0105	0.0037	S
8547.19065	−0.0015	0.0011	P	8584.42464	0.0095	0.0004	P
8547.92513	−0.0009	0.0004	S	8584.97007	0.0100	0.0005	P
8548.65979	−0.0009	0.0008	P	8585.51522	0.0101	0.0020	P
8549.39237	−0.0022	0.0002	S	8585.78721	0.0096	0.0012	S
8550.12742	−0.0019	0.0004	P	8586.33148	0.0089	0.0029	S
8550.86226	−0.0009	0.0004	S	8586.60501	0.0100	0.0014	P
8551.59654	−0.0013	0.0002	P	8587.14929	0.0093	0.0030	P
8552.32988	−0.0018	0.0005	S	8587.42257	0.0101	0.0005	S
8553.06553	−0.0009	0.0031	P	8587.96718	0.0097	0.0009	S
8553.79903	−0.0012	0.0004	S	8588.51152	0.0090	0.0023	S
8554.53307	−0.0019	0.0012	P	8588.78356	0.0086	0.0005	P
8555.26808	−0.0008	0.0012	S	8589.32941	0.0095	0.0027	P
8557.47022	−0.0019	0.0014	P	8589.60177	0.0093	0.0018	S
8558.20513	−0.0009	0.0005	S	8590.14614	0.0087	0.0013	S
8559.67260	−0.0020	0.0005	S	8590.41866	0.0088	0.0006	P
8560.40797	−0.0013	0.0004	P	8590.69104	0.0086	0.0012	S
8561.14256	−0.0006	0.0006	S	8590.96390	0.0090	0.0008	P
8561.87634	−0.0015	0.0005	P	8591.50848	0.0086	0.0014	P
8562.61077	−0.0009	0.0016	S	8591.78175	0.0094	0.0012	S
8563.34482	−0.0016	0.0003	P	8592.05275	0.0079	0.0024	P
8564.07928	−0.0010	0.0002	S	8592.32676	0.0094	0.0026	S
8564.81376	−0.0012	0.0001	P	8592.59761	0.0078	0.0013	P
8565.54791	−0.0009	0.0037	S	8592.87057	0.0083	0.0035	S
8566.28171	−0.0018	0.0006	P	8593.14403	0.0092	0.0017	P
8567.01631	−0.0011	0.0009	S	8593.41555	0.0083	0.0015	S
8567.75105	−0.0011	0.0003	P	8593.68863	0.0089	0.0024	P
8571.42224	−0.0009	0.0002	S	8593.96030	0.0080	0.0009	S
8572.15687	−0.0010	0.0005	P	8595.32411	0.0094	0.0019	P
8572.89097	−0.0007	0.0004	S	9281.17714	0.0064	0.0010	S
8573.62483	−0.0016	0.0001	P	9281.44922	0.0060	0.0009	P
8574.35938	−0.0009	0.0001	S	9281.72028	0.0045	0.0003	S
8575.09377	−0.0012	0.0001	P	9281.99361	0.0054	0.0004	P

Continued on next page...

Table A.6: Minima timings for pairs A and B of the system S4 Vel (Continued).

Pair A				Pair B			
HJD - 2450000	***O−C*** (days)	**Error**	**Type**	**HJD - 2450000**	***O−C*** (days)	**Error**	**Type**
8575.82785	−0.0010	0.0011	S	9282.26523	0.0045	0.0006	S
8576.56212	−0.0014	0.0006	P	9282.53833	0.0051	0.0004	P
8577.29692	−0.0005	0.0009	S	9282.81156	0.0058	0.0007	S
8578.03043	−0.0017	0.0008	P	9283.08317	0.0050	0.0003	P
8578.76500	−0.0010	0.0003	S	9283.35632	0.0056	0.0006	S
8579.49929	−0.0014	0.0001	P	9283.62873	0.0055	0.0013	P
8580.23388	−0.0007	0.0001	S	9283.90102	0.0053	0.0002	S
8580.96769	−0.0016	0.0001	P	9284.17368	0.0055	0.0006	P
8584.63990	−0.0003	0.0005	S	9284.44608	0.0054	0.0007	S
8585.37372	−0.0012	0.0004	P	9284.71841	0.0053	0.0004	P
8586.10771	−0.0011	0.0008	S	9284.99100	0.0054	0.0004	S
8586.84236	−0.0012	0.0004	P	9285.26429	0.0062	0.0004	P
8587.57666	−0.0007	0.0001	S	9285.53555	0.0049	0.0006	S
8589.04530	−0.0007	0.0007	S	9285.80907	0.0060	0.0005	P
8589.77997	−0.0007	0.0003	P	9286.07934	0.0037	0.0008	S
8590.51349	−0.0010	0.0008	S	9286.35361	0.0055	0.0005	P
8591.24791	−0.0013	0.0006	P	9286.62555	0.0050	0.0011	S
8591.98273	−0.0004	0.0003	S	9286.89823	0.0052	0.0003	P
8592.71671	−0.0011	0.0010	P	9287.17048	0.0049	0.0003	S
8593.45053	−0.0011	0.0006	S	9287.44558	0.0075	0.0004	P
8594.18572	−0.0007	0.0011	P	9287.71596	0.0054	0.0006	S
8594.91962	−0.0006	0.0009	S	9287.98711	0.0041	0.0005	P
9281.47875	0.0016	0.0001	P	9288.26094	0.0054	0.0005	S
9282.21257	0.0016	0.0001	S	9288.53377	0.0058	0.0004	P
9282.94734	0.0016	0.0001	P	9288.80690	0.0064	0.0006	S
9283.68170	0.0021	0.0001	S	9289.07804	0.0051	0.0004	P
9284.41568	0.0014	0.0001	P	9289.35124	0.0058	0.0004	S
9285.15003	0.0019	0.0001	S	9289.62355	0.0056	0.0009	P
9285.88462	0.0018	0.0002	P	9289.89585	0.0054	0.0003	S
9286.61882	0.0021	0.0001	S	9290.16859	0.0057	0.0004	P
9287.35306	0.0016	0.0001	P	9290.44016	0.0047	0.0008	S
9288.08735	0.0021	0.0001	S	9290.71441	0.0065	0.0009	P
9288.82177	0.0018	0.0001	P	9290.98645	0.0060	0.0018	S
9289.55550	0.0017	0.0001	S	9291.25866	0.0058	0.0008	P
9290.29005	0.0015	0.0001	P	9291.53084	0.0055	0.0006	S
9291.02467	0.0023	0.0001	S	9291.80360	0.0057	0.0005	P
9291.75842	0.0013	0.0001	P	9292.07602	0.0057	0.0005	S

Continued on next page...

Table A.6: Minima timings for pairs A and B of the system S4 Vel (Continued).

Pair A				Pair B			
HJD - 2450000	***O−C*** (days)	**Error**	**Type**	**HJD - 2450000**	***O−C*** (days)	**Error**	**Type**
9292.49312	0.0021	0.0001	S	9292.62068	0.0053	0.0008	S
9293.96131	0.0018	0.0002	S	9293.98227	0.0045	0.0002	P
9294.69646	0.0022	0.0001	P	9294.25648	0.0062	0.0004	S
9295.43017	0.0020	0.0001	S	9294.80232	0.0071	0.0005	S
9296.16442	0.0016	0.0001	P	9295.07368	0.0059	0.0011	P
9296.89865	0.0020	0.0002	S	9295.34585	0.0056	0.0007	S
9297.63276	0.0013	0.0001	P	9295.89133	0.0061	0.0004	S
9298.36727	0.0020	0.0002	S	9296.16224	0.0045	0.0008	P
9299.10122	0.0012	0.0001	P	9296.43576	0.0056	0.0005	S
9299.83594	0.0021	0.0001	S	9296.98122	0.0060	0.0006	S
9300.57053	0.0020	0.0002	P	9297.25428	0.0066	0.0010	P
9301.30425	0.0018	0.0001	S	9297.52428	0.0041	0.0006	S
9302.03872	0.0016	0.0001	P	9298.07157	0.0064	0.0007	S
9302.77328	0.0023	0.0001	S	9298.34458	0.0070	0.0005	P
9303.50761	0.0019	0.0001	P	9298.61655	0.0064	0.0003	S
9304.24143	0.0019	0.0001	S	9298.89041	0.0078	0.0007	P
9304.97594	0.0017	0.0001	P	9299.16004	0.0049	0.0005	S
10747.84831	0.0045	0.0002	S	9299.43470	0.0071	0.0012	P
10748.58210	0.0035	0.0001	P	9299.70724	0.0072	0.0007	S
10749.31711	0.0047	0.0000	S	9299.97728	0.0047	0.0015	P
10750.05117	0.0040	0.0001	P	9300.25120	0.0062	0.0002	S
10750.78523	0.0042	0.0001	S	9300.52489	0.0074	0.0016	P
10751.51972	0.0040	0.0001	P	9300.79625	0.0062	0.0004	S
10752.25388	0.0043	0.0000	S	9301.06774	0.0052	0.0019	P
10752.98799	0.0037	0.0001	P	9301.34084	0.0058	0.0011	S
10754.45669	0.0038	0.0001	P	9301.61509	0.0076	0.0013	P
10755.19105	0.0043	0.0000	S	9301.88651	0.0065	0.0005	S
10755.92511	0.0037	0.0001	P	9302.15797	0.0055	0.0021	P
10756.65976	0.0045	0.0001	S	9302.43124	0.0063	0.0004	S
10757.39381	0.0038	0.0001	P	9302.70532	0.0079	0.0011	P
10758.12806	0.0042	0.0001	S	9302.97628	0.0063	0.0007	S
10759.59671	0.0043	0.0001	S	9303.24815	0.0057	0.0016	P
10761.06495	0.0040	0.0001	S	9303.51989	0.0050	0.0011	S
10761.79953	0.0038	0.0001	P	9303.79541	0.0080	0.0011	P
10762.53362	0.0041	0.0000	S	9304.06663	0.0067	0.0006	S
10763.26753	0.0032	0.0001	P	9304.33855	0.0062	0.0016	P
10764.00237	0.0042	0.0001	S	9304.61155	0.0067	0.0009	S

Continued on next page...

Table A.6: Minima timings for pairs A and B of the system S4 Vel (Continued).

Pair A				Pair B			
HJD - 2450000	***O−C*** (days)	**Error**	**Type**	**HJD - 2450000**	***O−C*** (days)	**Error**	**Type**
10764.73646	0.0036	0.0000	P	9304.88541	0.0080	0.0014	P
10765.47068	0.0040	0.0001	S	9305.15606	0.0062	0.0002	S
10766.20535	0.0039	0.0000	P	9305.42824	0.0059	0.0012	P
10766.93944	0.0042	0.0001	S	9305.70252	0.0077	0.0012	S
10767.67396	0.0040	0.0001	P	10747.44393	0.0071	0.0002	P
10769.14224	0.0037	0.0000	P	10747.71626	0.0070	0.0003	S
10769.87650	0.0041	0.0001	S	10747.98807	0.0063	0.0003	P
10770.61071	0.0036	0.0001	P	10748.26103	0.0068	0.0003	S
10771.34532	0.0043	0.0001	S	10748.53343	0.0067	0.0003	P
10772.07941	0.0037	0.0001	P	10748.80611	0.0069	0.0002	S
10772.81347	0.0039	0.0001	S	10749.07851	0.0068	0.0003	P
10773.54843	0.0042	0.0001	P	10749.35004	0.0058	0.0003	S
10774.28228	0.0042	0.0001	S	10749.62342	0.0067	0.0002	P
				10749.89634	0.0071	0.0003	S
				10750.16895	0.0073	0.0003	P
				10750.44075	0.0066	0.0003	S
				10750.98634	0.0072	0.0003	S
				10751.25835	0.0067	0.0002	P
				10751.52977	0.0056	0.0000	S
				10751.80356	0.0069	0.0003	P
				10752.07586	0.0068	0.0003	S
				10752.34897	0.0074	0.0005	P
				10752.62054	0.0065	0.0002	S
				10752.89290	0.0063	0.0003	P
				10753.16546	0.0064	0.0003	S
				10753.43781	0.0063	0.0003	P
				10753.98299	0.0065	0.0002	P
				10754.25586	0.0068	0.0003	S
				10754.80037	0.0064	0.0002	S
				10755.07248	0.0060	0.0002	P
				10755.34477	0.0058	0.0002	S
				10755.61824	0.0068	0.0001	P
				10755.89106	0.0071	0.0003	S
				10756.16215	0.0057	0.0003	P
				10756.43500	0.0061	0.0003	S
				10756.70778	0.0064	0.0004	P
				10756.97982	0.0059	0.0003	S

Continued on next page...

Table A.6: Minima timings for pairs A and B of the system S4 Vel (Continued).

Pair A				**Pair B**			
HJD - 2450000	***O−C*** (days)	**Error**	**Type**	**HJD - 2450000**	***O−C*** (days)	**Error**	**Type**
				10757.25365	0.0072	0.0003	P
				10757.52573	0.0068	0.0002	S
				10757.79803	0.0066	0.0003	P
				10758.07148	0.0076	0.0002	S
				10758.34310	0.0067	0.0002	P
				10758.61500	0.0061	0.0003	S
				10758.88679	0.0054	0.0000	P
				10759.16019	0.0064	0.0003	S
				10759.43198	0.0057	0.0002	P
				10759.70594	0.0071	0.0004	S
				10759.97716	0.0059	0.0003	P

Figures

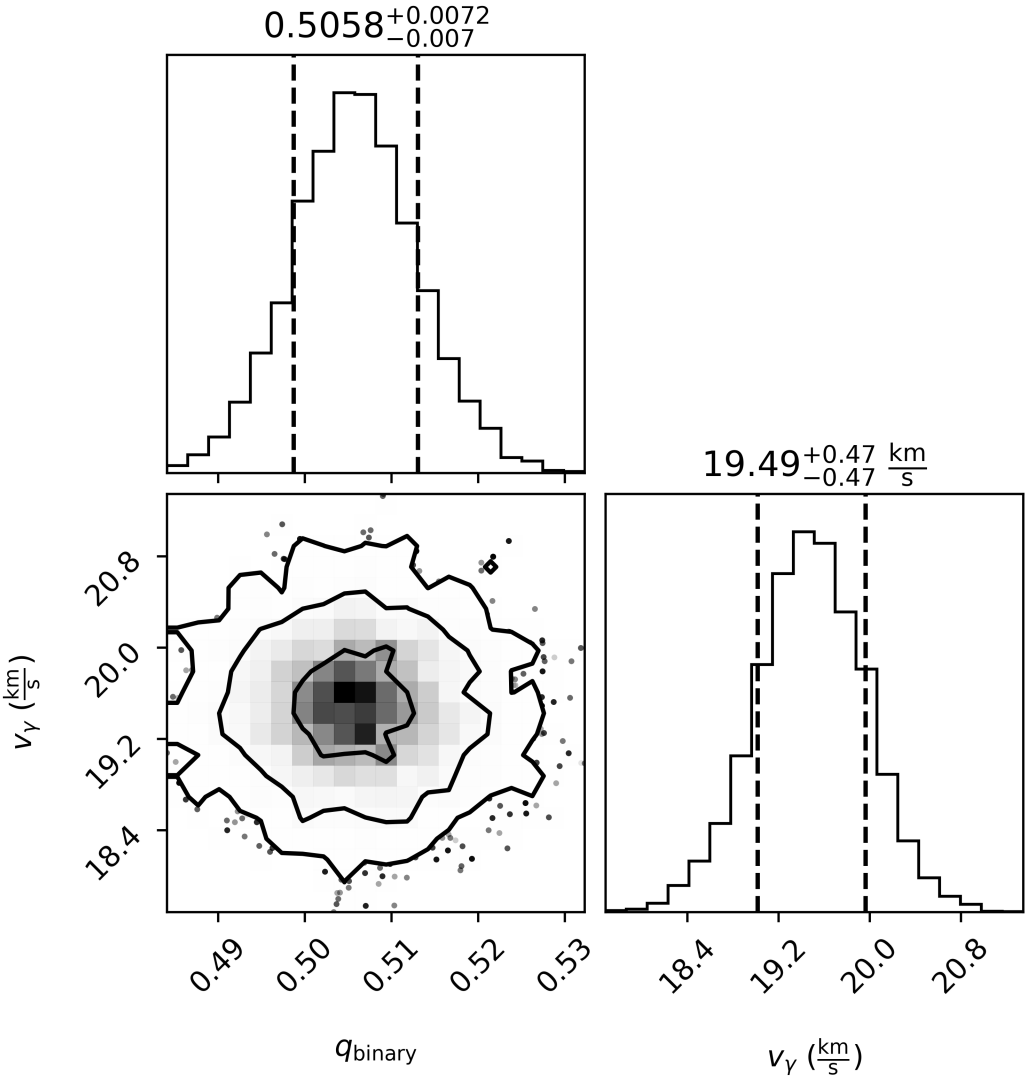

Figure A.1: Corner plot illustrating the posterior distributions of the dynamical parameters for the system S1 CMi, pair B, derived from the MCMC analysis of the radial velocity data. The plot displays the covariance between the mass ratio (q) and systemic velocity (v_γ). The diagonal panels show the corresponding 1D histograms, with vertical dashed lines indicating the median values and their associated uncertainties. The off-diagonal panel shows the 2D joint probability distribution, demonstrating the absence of significant degeneracy between the parameters.

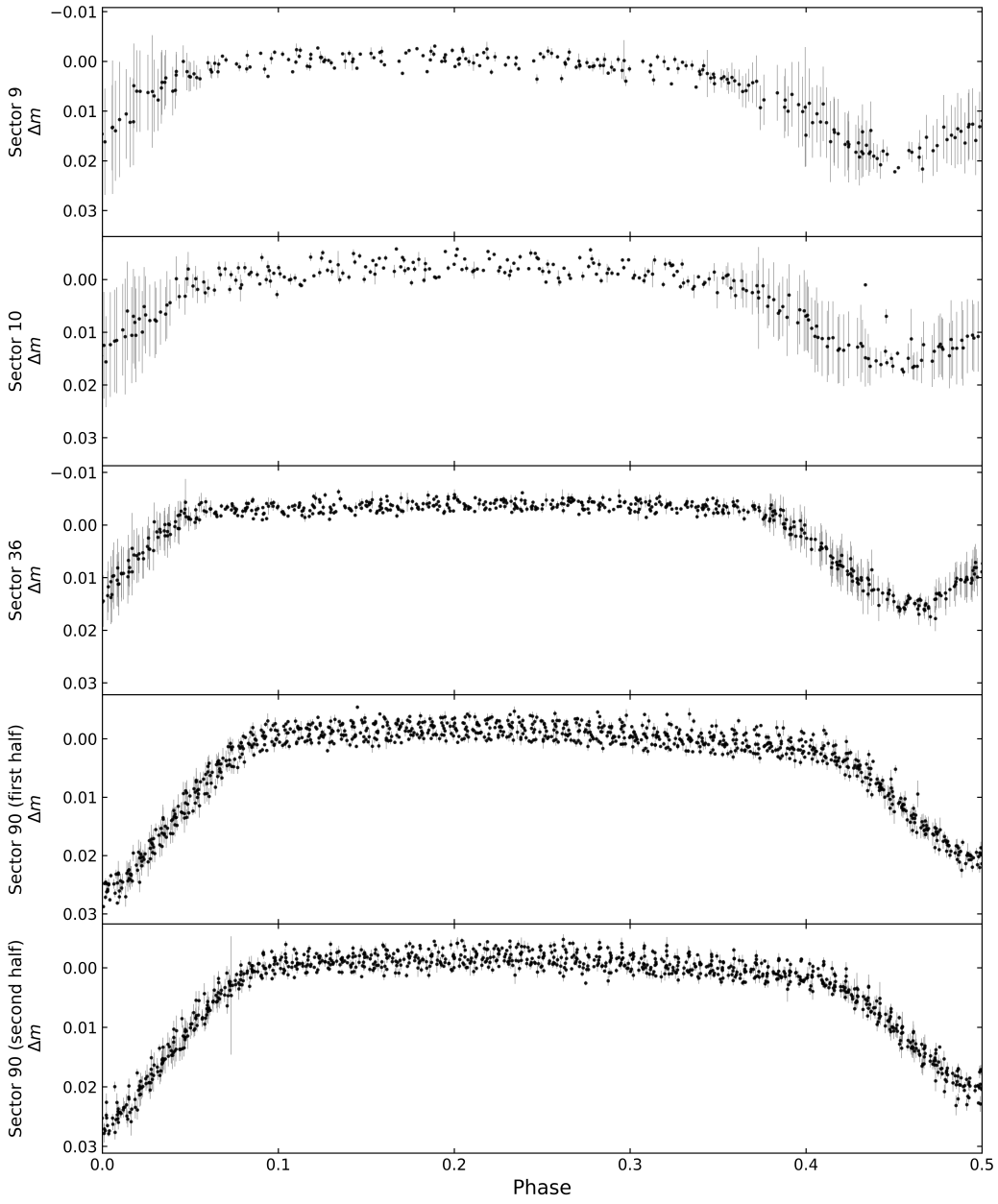

Figure A.2: Phase-folded *TESS* light curves for pair B of the system S4 Vel, binned by averaging every 2 data points for Sectors 9 and 10, and every 3 points for Sectors 36 and 90 (both parts), plotted individually by observational sector. This detailed view illustrates the variations in the out-of-eclipse regions of the phase curves.